

**Interaction Dynamics of High Reynolds Number Magnetized Plasma
Flow on the CTIX Plasma Accelerator**

by

Stephen Howard

B.A. Bennington College, Vermont 1999

A dissertation submitted in partial satisfaction of the
requirements for the degree of
Doctor of Philosophy

in

Plasma Physics

in the

GRADUATE DIVISION
of the
UNIVERSITY OF CALIFORNIA, DAVIS

Committee in charge:
Professor David Hwang, Chair
Professor Neville Luhmann
Professor Elbridge G Puckett

Spring 2006

The dissertation of Stephen Howard is approved:

Chair

Date

Date

Date

University of California, Davis

Spring 2006

**Interaction Dynamics of High Reynolds Number Magnetized Plasma
Flow on the CTIX Plasma Accelerator**

Copyright 2006

by

Stephen Howard

Abstract

Interaction Dynamics of High Reynolds Number Magnetized Plasma Flow on the
CTIX Plasma Accelerator

by

Stephen Howard

Doctor of Philosophy in Plasma Physics

University of California, Davis

Professor David Hwang, Chair

Compact Toroid Injection eXperiment defined

broad, simple description of project

Professor David Hwang
Dissertation Committee Chair

Dedication

Acknowledgments

..

..

Contents

List of Figures	v
List of Tables	vii
1 Introduction	1
1.1 Overview of study	1
1.2 Structure of CTIX device	3
1.3 Concept of a compact toroid plasma	6
1.4 Timescales within the life of a CTIX plasma	7
1.5 Typical CTIX Plasma Parameters	9
2 Compact toroid magnetic field geometry, experiment and theory	11
2.1 Hall term, $\mathbf{j} \times \mathbf{B}$	16
2.2 Magnetic field measurements	16
2.3 Lagrangian interpolation of probe signals	27
2.4 Characterization of CT modes	28
2.5 Comparison between experiment, theory, and simulation	28
3 Reconnection and compression experiment	30
3.1 Experimental set-up	31
3.2 Description of external coils	32
3.3 Diagnostics	33
3.4 Experimental Results for no Target Field	34
3.5 Results and analysis	34
3.6 Model of System	37
4 Determination of plasma resistivity	41
5 Temperature measurements	43
5.1 Particle velocity and energy	43
5.2 Thermalization of electrons	44
5.3 Experimental Overview	47
5.4 EAP Construction	48
5.5 Grid biasing	49
5.6 Relation between $I(V)$ and $f_E(E)$	51
5.7 Analysis Methods	54
5.8 Experimental results	54
5.9 Error analysis of simulated data	56

5.10 Statistical error analysis	57
5.11 Effect of smoothing	59
5.12 Summary of results	59
6 Measurements with high resolution spectrometer	61
6.1 Doppler measurements of plasma velocity	65
6.2 Measurement of Average Doppler Velocity	65
6.3 Photomultiplier tube measurements	69
6.4 Ionization model	72
6.5 Conclusions	76
6.6 Future work	76
7 Determination of plasma Reynolds number, hydrodynamic and magnetic	79
7.1 Definitions	79
7.2 Range of accessible values	80
8 Gas puff imaging technique	81
8.1 Excitation dynamics	82
8.2 Implementations on CTIX drift section	82
8.3 Cameras	82
8.4 Spectral measurements	82
8.5 quad PMT and LMP measurements	82
9 Kink dynamics of central column	83
9.1 GPI results	83
9.2 Magnetic field results	84
9.3 Comparison to theory of kink instability	84
10 Wire target perturbations	85
10.1 Target design	85
10.2 Observation of coherent density waves	85
10.3 Observation of turbulent waves	89
10.4 Comparison of experimental results with plasma turbulence theory	92
A Magnetic helicity of a CT	94
B Magnetic computations for probe calibration	96
C Method of reconstructing a moving pulse	97
C.1 Sequential measurements of a moving pulse	98
C.2 Lagrangian Interpolation Algorithm	99
C.3 Estimation of Flow Field	100
C.4 Validity of Approximation	101
C.4.1 First order velocity error	101
C.4.2 Constraints on the amplitude of undetectable transient pulses	103
D Equations of incompressible resistive MHD	108
E Vector field visualization using a complex color code	110
F Direction of future research	111

List of Figures

1.1	3D view of CTIX showing magnetic probe positions and circuit schematic	4
2.1	Relationship between surface current and magnetic field components	12
2.2	Sketch of magnetic probe port and the effect it would have on a uniform field	18
2.3	Analytic result for magnetic field	21
2.4	Conformal mapping method for 2-D approximation	23
2.5	2-D Relaxation simulation result of magnetic field near a conducting port well	26
2.6	Full-volume expansion factor and effective depth	26
2.7	Reduced-volume expansion factor and effective depth	27
2.8	Measured magnetic fields at $z = 91\text{cm}$	28
2.9	Accelerated Taylor equilibrium with axial compression (absolute value of B_θ)	28
2.10	Modified accelerated Taylor-like equilibrium model	29
3.1	Compression effect of axial field on light emission from CT	35
3.2	Effect of reconnection with axial field on light emission from CT	35
3.3	Effect of external field on CT velocity	36
5.1	Exploded view of EAP showing grids and collector plate	49
5.2	Schematic of EAP biasing circuit	50
5.3	Time dependence EAP collector current, parameterized by control bias voltage	50
5.4	Analysis method using moving-window smoothing	53
5.5	Raw data from pre-injection EAP measurements with resulting $I(V)$ curves	55
6.1	Survey spectrum of Helium plasma near He II line	63
6.2	Survey spectrum of Helium plasma near He II line	64
6.3	Average Doppler velocity as a function of time	68
9.1	Gas puff kink instability caused by accelerator current	83
9.2	Gas puff kink instability caused by accelerator current	84
9.3	Free-form filament curves	84
10.1	Plane wave locations	86
10.2	K-space distribution of Plane waves	86
10.3	Ratio of expected exposure smear length to wavelength	87
10.4	Wavelength vs plasma flow speed	88
10.5	Coherent waves in plasma, USE BETTER EXAMPLES	89
10.6	Coherent waves in plasma, USE BETTER EXAMPLES	89
10.7	Coherent waves in plasma, USE BETTER EXAMPLES	90

10.8 Coherent waves in plasma, USE BETTER EXAMPLES	90
10.9 Coherent waves in plasma, USE BETTER EXAMPLES	91
10.10 Transition to turbulent flow	91
10.11 Fourier transforms of transition to turbulent flow	93
B.1 Plot of computational error for relaxation method	96
C.1 Transient Pulse	104
C.2 Maximum possible amplitude of error	106

List of Tables

5.1	EAP 9.5 kV Data Summary	55
5.2	EAP 12 kV Data Summary	55
5.3	EAP 15 kV Data Summary	55

Chapter 1

Introduction

1.1 Overview of study

My work has dealt with a sequence of basic plasma physics questions with the aim to better understand the nature of high speed flow of a magnetized plasma. One important aspect of this work is the physics of turbulent flow states. The device that makes this investigation feasible is the CTIX plasma accelerator. However, our great success at designing and operating this accelerator has been founded on only a very rudimentary model of the plasma physics involved. Like early hominids, not understanding combustion chemistry hasn't stopped us from rubbing two sticks together and making fire.

And so, as I have endeavored to do something new and useful with CTIX, I have been repeatedly confronted with fundamental questions of regarding the plasma physics that makes it all work in the first place. I have tried to answer these questions as they have become experimentally accessible, and I have attempted to synthesize our results into improved models of what is actually going on inside the plasma. The individual results I have produced are interesting in themselves, in that they advance our understanding of the inner workings of CTIX-like plasma accelerators; but as a collection they have a more general usefulness by providing accurate knowledge of initial con-

ditions and plasma parameters for use when analyzing the experimental data that address universal phenomena such as magnetohydrodynamic (MHD) turbulence.

I have organized my results in an sequence from Chapter 2 to Chapter 7 that logically build on one another toward establishing the key prerequisites for an MHD turbulence experiment. Chapter 2 examines the structure and dynamics of the compact toroid's magnetic field. This information is critical for properly analyzing the Reconnection/Compression experiments described in Chapter 3, and the outcome is a measurement of the so called anomalous resistivity (or magnetic diffusivity) of the plasma as described in Chapter 4. Together this work provides the initial conditions for the drift section measurement of kink dynamics and the wire target turbulence experiments discussed in Chapter 9 and 10.

Chapter 5 describes measurement of the electron temperature of the plasma and looks at the dynamics of energy conversion during the process of interaction with a transverse magnetic field. The knowledge about the electron temperature helps to construct an accurate model of the ionization of helium under our range of conditions. Helium enters the equation because of its ability to emit light brightly when bombarded with plasma electrons. This optical emission provides several diagnostic opportunities. The first is explored in Chapter 6; using a high resolution spectrometer we were able to measure the Doppler shift of spectral line of He II ions, in doing so we measured the velocity of the plasma in previously inaccessible locations in the vessel. Several of these preliminary results are combined in Chapter 7 where I calculate values of the Reynolds numbers that occur in the CTIX plasma flow. The dimensionless Reynolds numbers play a vital role in determining the properties of a fluid flow, and the issues regarding turbulence that we can address with CTIX are focused on how experimental observable change with changing Reynolds number.

From Chapter 8 on we direct our attention to the experiments in the drift section of CTIX where conditions are suitable for exploring MHD turbulence. Chapter 8 discusses our primary tool for investigating turbulence, a technique called Gas Puff Imaging (GPI) in which a cloud of neutral helium can be used to image plasma density fluctuations. Chapter 9 presents analysis of images

taken with fast cameras and gas puffs that show the MHD kink instability at work on the central column of plasma that carries the accelerator current after the compact toroid has entered the drift section. Chapter 10 introduces a wire target that was used in a set of experiments to act as a magnetic perturbation to the plasma flow, and presents the analysis of images that show coherent and incoherent density waves that are created in the presence of the wire target perturbation. Lastly we will compare these results with relevant ideas in turbulence theory.

Proposed future work and a variety of technical details are included as appendices.

1.2 Structure of CTIX device

The Compact Toroid Injection eXperiment, (CTIX), is a coaxial railgun that forms and accelerates magnetized plasma rings called compact toroids (CT's). CTIX consists of a pair of cylindrical coaxial electrodes with the region between them kept at high vacuum. The outer conductor vessel is 2.5 m in length and 15.24 cm in diameter. The electrodes are connected to high voltage 50 μF capacitors and metglass passive timing delay inductors that together form the rail gun circuit. The electrically conductive CT plasma forms a sliding short between the inner and outer electrodes, and completes the path for current to flow down the center conductor, across the plasma, and back along the outer conductor. The railgun effect that accelerates the CT can be accounted for by the Lorentz $\mathbf{j} \times \mathbf{B}$ force density, where \mathbf{j} is the current density driven by the external circuit, and \mathbf{B} is the magnetic field created by the current flowing in circuit, (primarily down the center conductor). There are separate capacitor banks for the formation and accelerator sections that can be charged to different voltages. The final velocity of the CT can range from $V_{CT} = 5\text{cm}/\mu\text{s}$ up to $V_{CT} = 25\text{cm}/\mu\text{s}$. V_{CT} can be adjusted within this range by changing the applied accelerator voltage. The mass of the injected hydrogen CT is typically in the range of a few micrograms.

The center electrode has a larger diameter in the formation region, has a step down in diameter, and then a tapered section, and finally it has a long, slightly thinner straight section where

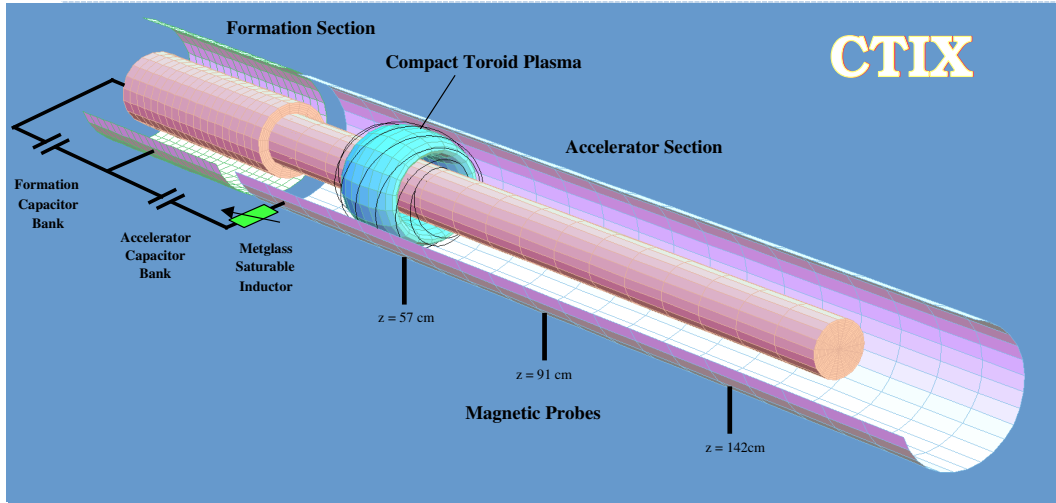


Figure 1.1: 3D view of CTIX showing magnetic probe positions and circuit schematic

most of the CT acceleration occurs. The outer electrode has a corresponding tapered section at the junction between the formation and acceleration regions. Originally the center electrode was electroplated with gold to minimize surface effects from the raw stainless being exposed to the plasma. However, after years of operation, the sustaining direct impact of massive high current discharges at gigawatt power levels has resulting in most of the gold plate in the middle of formation section becoming completely removed via ablative processes and deposited elsewhere in the vessel. Some regions near the step down edge on the center conductor ($z = 20$ cm) have accumulated the gold deposits as a highly textured surface that looks like cracked stucco or peeling paint. We don't know exactly what effect this surface has on the formation process, but all evidence suggests that either it does not matter at all, or it actually improves the formation of high density compact toroids.

The possibility that this surface texture could be beneficial is interesting, and not inconceivable. Electric fields will be significantly stronger at the tips of the gold flakes than elsewhere in the bulk volume. Positive contributions to the formation process might be accounted for by some kind of hollow-cathode effect, in which the small flat spaces between the flaking gold layer and the

vessel wall act to create very efficient fast ionization of the plasma over a large surface area. Additionally, such an unusual formation boundary condition might partially account for the fact that the neutral gas break-down event is held off for such a long time (several ms) while the seed magnetic field decays until it is at just the right magnitude and field geometry, and then break-down spontaneously occurs. It is also possible that such a rough surface on the boundary of the newly forming plasma could modify the fluid velocity field, such as by exciting high k turbulence for example, which ultimately results in the mysteriously efficient fast dynamo effect that is responsible for the creation of the large internal magnetic field of every single compact toroid we generate on CTIX. The observations of extended hold-off of break-down, and unusually high flux amplification factor (~ 200), that occur during the plasma formation are two of the most basic features on the CTIX device. They are definitely in need of further explanation, and the effects of a non-trivial boundary condition should be an important element to consider in future work on the subject.

CTIX was situated so that it can inject its CT's into the Davis Diverted Torus (DDT), which is a small toroidal device that was built in order to investigate basic tokamak physics. Composed of a stainless steel toroidal vacuum vessel, major radius of 44 cm, minor radius 14 cm, which is surrounded by 7 toroidal field coils, as well as a variety of poloidal field coils, an Ohmic core, and a set of pre-ionization coils. DDT originally operated in a pulsed mode where a tokamak-like plasma was heated and confined.

However, as the focus of experiments shifted toward CTIX we ceased the full-power pulsed mode and only operated DDT with smaller currents in a continuous mode. In this mode a tokamak-like plasma is not possible or desired. Instead, we injected the CT into the vacuum field of DDT so that we can observe the interaction of the CT and the continuous toroidal field. The presence of tokamak plasma would make the diagnostic situation more difficult in certain ways, mostly because once reconnection has occurred there is no easy way to distinguish between the tokamak plasma and the CT. Without the tokamak plasma getting in the way of our diagnostics, we can look at zeroth order stopping effects, as well as post-reconnection dispersion and thermalization since the

only plasma in the device is that which originated in the CT.

The toroidal field coils of DDT have a radius of 40 cm and produce about 3 Gauss per Amp at the center of the minor axis of the vacuum vessel. They are water cooled and can produce a maximum field of 600 Gauss in continuous mode. [ref NF high beta paper]

1.3 Concept of a compact toroid plasma

A compact toroid is a magnetized plasma ring formed within a conducting vessel of coaxial geometry. The term “compact” is used because traditionally these plasmas tend to be formed between coaxial electrodes having only a modest outer radius of about 10 cm. It has a strong interior magnetic field that has a special geometry with closed flux surfaces that results in plasma particles being trapped on the field lines for much longer than the escape time due to the particle’s thermal velocity.

Also, this magnetic field is self-generated by the currents flowing within the plasma ring. In this way the compact toroid is self-confined in a stable geometry that persists until the internal currents resistively die down or particles escape as certain non-trivial phenomena eventually dominate. This special magnetic field geometry has comparable poloidal and toroidal components at each point within the plasma. Field lines wrap around toroidal surfaces called flux surfaces, in this way field lines can be grouped by what flux surface they lie on, and the entire magnetic field constitutes a set of nested tori of flux surfaces.

The fields are maintained by associated toroidal and poloidal plasma currents. Its magnetic geometry is much like a spheromak, the distinction between them is primarily that a compact torus is being accelerated by a large railgun current, whereas a spheromak is formed at rest with respect to the laboratory. Also, spheromaks are formed in large, roughly spherical vessels, while the coaxial vessel allows the compact toroids to have almost any aspect ratio, and can range from doughnut shapes to long, cigar shapes.

A more detailed account of the theory of the magnetic equilibrium of compact toroids and spheromaks will be presented in Chapter 2. The CT has a long lifetime of over 1 ms and is able to hold itself together under some rather large forces. The compact toroids formed on CTIX are classified as low beta plasmas, where beta is the ratio of the hydrodynamic thermal pressure to the magnetic pressure. This is important because it means that magnetic effects will dominate pure hydrodynamic effects, and so certain approximations become convenient to use.

There is a large toroidal magnetic field behind the CT, initially generated by the railgun current flowing in the center conductor. This field becomes spatially uniform and steadily dies down as the column of magnetized plasma behind the CT expands, thereby driving the acceleration of the compact toroid.

As it leaves the accelerator, CT plasma is relatively dense $n = 10^{14}$ particles per cm^3 and of modest temperature $T_e = T_i = 50eV \sim 580,000^\circ K$.

Measured surface magnetic fields at the edge of the CT are large $B \sim 1kGauss$ to $5kGauss$ and internal magnetic fields are expected to be a factor of 3 to 10 times larger.

The CT plasma is self confined, in a minimum energy equilibrium configuration. Low thermal Beta, high kinematic beta.

Impurities in the plasma emit plenty of light $10^{17} photons/cm^3 sec$ and is optically thin in the visible range.

Fluid Reynolds number = $V_{CT}L/v = 100$ to 10^4 Magnetic Reynolds number = $V_{CT}L/D_M$
 $= 10$ to 10^4

1.4 Timescales within the life of a CTIX plasma

The innovative aspect of the CTIX design is that it is capable of sustained operation with a maximum firing rate of 0.2 Hz, (1 shot every 5 seconds). We will often refer to the firing rate of CTIX as its rep rate or repetition rate. When we were taking data the rep rate was typically 0.05

Hz (1 shot every 20 seconds) so that the vacuum vessel could be fully pumped back down to base pressure between shots.

The standard firing rate is sufficiently fast to be able to take 1000 shots a day. If the pumping rate was significantly increased (or injected gas volume was decreased), in principle the repetition rate could be increased to 1 kHz if the capacitors could be maintained at high voltage.

CTIX's rapid fire ability is due to the fact that it is passively switched. The only active thing we do in firing CTIX is to trigger the gas valve to let a puff of gas into the formation section, which is already energized to a steady high voltage of typically 10 kV. Then at some randomly occurring time later, the gas ionizes due to the formation potential, thereby completing the formation circuit.

After a fixed delay of about $4 \mu s$ that allows the magnetized plasma to expand into the acceleration region and relax into a CT geometry, the accelerator circuit fires, which accelerates the CT to its injection velocity.

The whole system is passively dependent on the event of the gas break-down which means that CTIX can fire any number of times in quick succession at what ever rate you can successfully send in distinct pulses of gas. The only limitation is that presently the capacitors loose their charge after only one firing cycle.

The basic operations of CT formation and acceleration have been demonstrated to operate very robustly, with a nearly failure-free production of compact toroids over the course of more than 60,000 firings of CTIX. Although CTIX almost never fails to produce and accelerate viable CT's, there is a noticeable amount of random variation of CT properties from one shot to another. With all experimentally controllable settings of the device held fixed, important observables such as plasma density, CT magnetic field shape and strength, and CT final velocity, will jump around randomly within some finite range. These fluctuations are attributed to uncontrollable variations in the initial conditions during the CT formation process.

For example, the formation gas valve sometimes lets in a little more hydrogen then average, sometimes less, resulting in a correspondingly greater or lesser CT plasma density. Another

uncontrollable event is the ionization of the neutral hydrogen (called the breakdown), which will occur at a randomly occurring time, that can vary as much as several milliseconds.

The time of breakdown should depend on the density of the formation cloud of neutral hydrogen, the strength and geometry of the formation magnetic field that acts to bend the trajectories free charged particles, and it most critically depends on the some spontaneous creation of enough free electrons (possibly via cosmic rays) to trigger the needed runaway cascade of electron impact ionization. Overall, there are many more questions than answers regarding the details of the formation process.

Along CTIX there are a number of magnetic field probes. Each is capable of resolving poloidal and toroidal components of the magnetic field at the outer edges of the CT. These different components are recorded on separate digitizer channels. We have three magnetic probes situated along the length of the accelerator at 57 cm, 91 cm, and 142 cm from the gas valve. The B_z probe signals are used on a daily basis for to see the existence of the CT and to get a quick estimate of its velocity.

1.5 Typical CTIX Plasma Parameters

tabulate?

Densities of $n_e = n_i = 10^{14}$ to 10^{15} cm^{-3} , hence a plasma frequency of $\omega_p \sim 20 \text{ GHz}$ Peak magnetic field inside CT: $B_\theta = B_z = 1$ to 10 kGauss Electron Temperature Varies from 10 eV to 80 eV Debye Length $\lambda_D = 7 \times 10^{-5}$ to $7 \times 10^{-4} \text{ cm}$ Electron Gyroradius inside CT = $7 \times 10^{-4} \text{ cm}$ to 0.02 cm The DDT toroidal field coils have a radius of 40 cm and produce about 3 Gauss per Amp at the center of the minor axis of the vacuum vessel. They are water-cooled and have achieved a maximum field of 600 Gauss in continuous mode.

[should I include a section listing diagnostics?]

A number of current monitors were in use for diagnosing what is going on within the CTIX

accelerator circuit. These measured currents flowing between different parts of the machine as a function of time. They were also useful to track down sources of ambient noise and minimize the effect of such sources.

Chapter 2

Compact toroid magnetic field geometry, experiment and theory

Let us now examine the basic constraints imposed on a self-confined magnetized plasma ring that exists within in a cylindrically symmetric conducting vessel. The coaxial geometry of CTIX will require that we apply the following boundary conditions at both the inner and outer walls. It is natural to work in a cylindrical coordinate system (r, θ, z) .

The time varying part of the magnetic field \mathbf{B} of the compact toroid must satisfy the boundary conditions

$$\mathbf{n} \cdot \mathbf{B} = 0 \quad \mathbf{n} \times \mathbf{B} = \mu_0 \mathbf{K} \quad (2.1)$$

where \mathbf{K} is the surface current density. To satisfy the first condition, B_r must vanish at the wall. From the second condition we see that B_z is nonzero if there is a surface current K_θ in the azimuthal direction, and B_θ is nonzero if there is a current K_z in the axial or z direction.

Thus measurements of B_z and B_θ at the wall as a function of axial position and time (z, t) will let us know the state of the magnetic field and the current density at the boundary of the plasma.

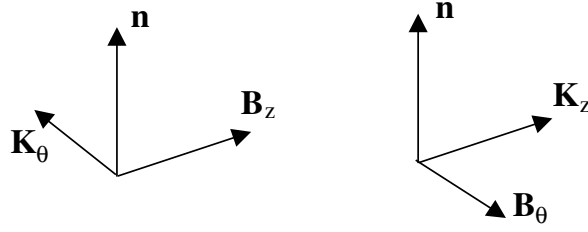


Figure 2.1: Relationship between surface current and magnetic field components

Much work has been done on the theory of force free equilibrium of plasmas in cylindrical, toroidal, and coaxial geometries. The relaxation of a magnetized plasma to a state of minimum magnetic energy, while global helicity is preserved, results in the Woltjer-Taylor force free equilibrium ($\mathbf{j} \times \mathbf{B} = \nabla P = 0$) given by

$$\nabla \times \mathbf{B} = \lambda \mathbf{B} \quad (2.2)$$

where $\lambda = \mu_0 j / B$.

Within a conducting vessel of coaxial geometry, and with the added assumption of zero axial surface current, $K_z = 0$, an axisymmetric solution exists that is separable and is expressible in terms of Bessel functions according to

$$B_r = B_0 \frac{k_z}{\lambda} \cos [k_z(z - z_0)] [J_1(k_r r) + f Y_1(k_r r)] \quad (2.3)$$

$$B_z = -B_0 \frac{k_r}{\lambda} \sin [k_z(z - z_0)] [J_0(k_r r) + f Y_0(k_r r)] \quad (2.4)$$

$$B_\theta = -B_0 \sin [k_z(z - z_0)] [J_1(k_r r) + f Y_1(k_r r)] \quad (2.5)$$

where $k_r^2 + k_z^2 \equiv \lambda^2$ relates the radial and axial wavenumbers to the magnetic eigenvalue λ .

To match the first boundary condition, values of k_r and f must be found such that $B_r(r, z) = 0$ at the inner and outer walls, $r = r_1$ and $r = r_2$ respectively. The radial term is

zero when

$$f = -J_1(k_r r_1)/Y_1(k_r r_1) = -J_1(k_r r_2)/Y_1(k_r r_2)$$

and so k_r must satisfy

$$J_1(k_r r_1)Y_1(k_r r_2) - J_1(k_r r_2)Y_1(k_r r_1) = 0$$

For the CTIX vessel, $r_1 = 3.34 \text{ cm}$ and $r_2 = 7.62 \text{ cm}$ in the acceleration section and so $k_r = 75.18 \text{ m}^{-1}$.

In order for $B_z = 0$ at $z = z_0$ and $z = z_0 + \Delta z$, $k_z = m\pi/\Delta z$. The axial extent of the compact toroid within CTIX tends to be about $\Delta z = 1$ meter and should be dominated by $m = 1$ mode, which implies that $k_z = 3 \text{ m}^{-1}$.

Using these values the Taylor state eigenvalue should be $\lambda = 75.24 \text{ m}^{-1}$. From this result we would also conclude that the ratio of the current density to magnetic field is

$$j/B = \lambda/\mu_0 = 5.98 \times 10^7 \text{ H}$$

where $H = 1 \text{ Henry} = C^2/kg \text{ m}^2$.

This means that for a modest CT surface field of 0.1 Tesla we would have a current density of about $6 \times 10^6 \text{ Amps/m}^2$ or 60 kA/cm^2 . This is roughly in agreement with measured currents.

One paper on this general topic is a 1993 paper discussing the Marauder plasma accelerator and their experiments [ref]. Their paper tackles the issue of MHD equilibrium for compact toroids, and presents a combination of analytical results, simulation and experimental results. Overall it is a very useful review of many relevant topics, and is the only published account I have been able to find that gives an analytic solution of $\nabla \times \mathbf{B} = \lambda \mathbf{B}$ in a coaxial geometry.

Despite their thoroughness, they made a few problematic mistakes in their presentation of the theory of force-free equilibria that are worth notice. The least of the errors was a simple typo, they gave the magnetic helicity as $\mathbf{A} \times \mathbf{B}$, when it should be $\mathbf{A} \cdot \mathbf{B}$ ¹.

¹See Appendix A for a discussion of Helicity of a force-free state

In the same section they made a more confounding mistake by writing down a believable-looking yet incorrect solution for the magnetic field of a force-free state $\nabla \times \mathbf{B} = \lambda \mathbf{B}$ in a coaxial geometry. Lastly, they listed a key reference that seemingly does not exist, even after much effort investigating a very wide margin of possibility for typographic or factual error.

As it relates to my present discussion, relying on the correctness of their published formulas caused some difficulty when I first attempted to make quantitative comparisons between theory and our experiment. The effect is that their formula gives a much larger B_z than B_θ inside the CT, whereas experiment showed that the two components are roughly equal (within a factor of 2). Their formula for B_z had a coefficient (k_r^2/k_z^2) , but when the curl is taken and field components are compared, I found that B_z should just depend on (k_r/k_z) , not squared. The corrected formulas listed above (2.3 - 2.5) actually satisfy $\nabla \times \mathbf{B} = \lambda \mathbf{B}$, while their counterparts in the 1993 paper did not. When this is corrected, the ratio of B_θ/B_z approaches unity within the CT, basically in agreement with experiments.

A further point of refinement can be made, which will be examined more closely in the next section, if the bending of the field lines near the probe port hole is taken into account. This bending results in an effective depth of the probe measurements that is approximately 0.5 cm into the interior of the plasma. The Taylor state model predicts that at this depth, the magnitude of B_θ should be very close to 1/2 of the value of B_z . More generally, it also predicts that within the CT the ratio B_θ/B_z should be only a function of radial position.

When compared to our experiments, this first prediction that our probes should measure $B_\theta = \frac{1}{2}B_z$ is right on the mark when looking at the time of the peak value of B_z at the center axial position of the CT. On the majority of shots we observe a noticeable dip in the B_θ signal that is coincident with the CT center, whose amplitude is very close to 1/2 the peak value of B_z . My interpretation is that this central dip in B_θ is due to Taylor state fields.

However, on almost every shot, the behavior of B_θ inside the CT disagrees qualitatively with the second prediction of the Taylor state model; that the ratio B_θ/B_z is not a function of z.

Our measurements show a significant ramping up of B_θ , going from zero at the leading edge of the CT to about 1/2 to 3/4 of the value of $B_z(t_{peak})$, by the time the back edge of the CT has passed the probe. Then when the probe crosses over into the pushing field, B_θ increases to be at or above the value of the peak of B_z .

This linear ramp-up of B_θ inside the CT is not accounted for by the Taylor state, and some kind of modification to the simple force-free state is required.

One physical complication that may account for the departure away from the simple Bessel function solution is the nature of the current paths near the wall. In the actual device, acceleration of the CT is accomplished by large rail-gun currents that flow axially down the inner conductor, then flow radially through the plasma, and return via the outer conductor.

Because magnetic field is frozen into the plasma during formation, large poloidal currents and toroidal magnetic fields persist in the CT as it propagates. In the outer regions of the CT poloidal currents that intersect the wall are able to penetrate into the conducting wall one skin depth and then flow axially through the walls some distance before merging back into the plasma.

Thus in the vicinity of the CT there is axial surface current $K_z \neq 0$ and so $B_\theta \neq 0$ at the walls in this region, in disagreement with one assumption that leads to the closed form solution (2.3 - 2.5). Also, where poloidal current enters or exits the wall $j_r \neq 0$ yet the boundary conditions require that $B_r = 0$ at the wall, in contrast to the force-free model that predicts a constant proportionality between all components of current density and magnetic field, $\mathbf{j} \times \mathbf{B} = 0 \longrightarrow \mathbf{j} = \frac{\lambda}{\mu_0} \mathbf{B} \longrightarrow j_r = \frac{\lambda}{\mu_0} B_r$ and so this is in contradiction with observation at least in the vicinity of the walls.

The observation that $j_r \neq 0$ at the walls is well supported by measurements of B_θ . We can evaluate Ampere's equation $\nabla \times \mathbf{B} = \mu_0 \mathbf{j}$ in cylindrical coordinates with assumed axisymmetry.

The resulting components of \mathbf{j} are:

$$j_r = -\frac{1}{\mu_0} \frac{\partial B_\theta}{\partial z} \quad (2.6)$$

$$j_\theta = \frac{1}{\mu_0} \left(\frac{\partial B_r}{\partial z} - \frac{\partial B_z}{\partial r} \right) \quad (2.7)$$

$$j_z = \frac{1}{\mu_0 r} \frac{\partial r B_\theta}{\partial r} \quad (2.8)$$

So we can find j_r at the outer wall by measuring the z dependence of B_θ with surface probes. We observe large radial currents j_r of $\sim kA/m^2$ entering and exiting the outer wall.

The interesting questions involve exactly how the CT magnetic geometry varies away from a true force-free Taylor equilibrium when the CT is strongly accelerated.

The surface magnetic field of CTIX plasma has been measured. The details of our methods will be discussed in the remaining sections of this chapter.

2.1 Hall term, $\mathbf{j} \times \mathbf{B}$

2.2 Magnetic field measurements

The measurements of the axial and toroidal magnetic field components are done with special magnetic probes, each component is measured with its own $1\text{ cm} \times 1\text{ cm}$ square loop coil of several turns. The two loops are wound at right angles to each other through small holes at the tip of a long plastic rod (see figure 2.2).

As the net magnetic flux through the loop changes when the magnetized plasma flows around it, a corresponding current is induced in the wire that is proportional to the time derivative of the instantaneous magnetic field at the loop. This current is put through a passive RF integrator that effectively takes the time integral of the signal, and the output signal is digitized.

This recorded signal has some further numerical corrections applied to it in order to compensate for an inherent droop effect of the integrator circuit. The final product is a well calibrated measure of the magnetic field strength as a function of time at the position of the loop.

Some complications arise when we attempt to compare the experimentally measured magnetic field with the predictions of analytic or computational models. The non-experimental models presently do not take into account some important details of the actual vessel geometry in the vicinity of the magnetic field probe ports.

Each magnetic probe port consists of a 0.874 inch hole in the stainless steel outer conductor, with a stainless tube (0.874 inch inner diameter) welded to the hole and extending radially outward (about 1 inch) to a flange that makes an o-ring vacuum seal with a 1/2 inch diameter ceramic tube. The ceramic tube is 6 inches long with one closed end that is inserted into the vessel so that the tip of the ceramic tube is approximately flush with the inner surface of the outer conductor. The other end of the ceramic tube is open to the air, and a plastic rod with the magnetic probe coils at its end is then inserted fully into ceramic tube so that the coils are as close to the plasma as possible.

The ceramic tube acts in three ways: 1) as high voltage insulator to protect the probe coils from the ~ 10 kV potential of the outer conductor, 2) as a vacuum seal and vessel wall that separates the atmospheric pressure from the 10^{-6} Torr vacuum inside CTIX, 3) and as dielectric boundary that lets magnetic field at the edge of the plasma to enter the probe coil and be detected.

Thus the probe coils are actually inside a finite-sized conducting cylindrical well, approximately 0.874 inches in diameter and 0.765 inches deep. The boundary conditions are significantly different than if the port was not there. As the magnetized plasma flows by a port, it dips into the annular gap between the outside of the ceramic tube and the inside of the stainless steel. Even if plasma flow effects are ignored, the edge magnetic field will expand to fill the conducting well of the port and there will be a gradient in the field as components change to match the boundary conditions. So the result of the measurement depends strongly on the precise depth of the probe position inside the port well.

One key characterization that is needed to properly interpret the magnetic measurements is to calculate an effective depth of the experimental magnetic measurements. The idea is that because of the well geometry of the port, the probes are effectively measuring the fields at some point in the

interior of the plasma, some small but not exactly zero distance away from the outer wall.

This would help reconcile the fact that the analytic Bessel function solution to the Woltjer-Taylor force free equation has zero B_θ at the walls, while our probe measurements show it to be non-zero. If we accept that the probe is not actually measuring exactly “at the wall” but rather at the effective depth into the interior, then the question of consistency is relaxed. The comparison between model and experiment would then become a quantitative comparison of the ratio of field components at the effective depth.

A reasonable approximation can be made by considering the magnetostatic problem with an ideal conductor in the shape of the magnetic probe port. This ignores any plasma dynamics that might effect the measurement, but in the case of a low beta plasma, like our CT, the magnetic field is boss. And although we consider a magnetostatic problem, this isn’t such a bad approximation given that the relevant MHD transit timescales are many orders of magnitude slower than the speed-of-light transit timescale for the probe port system. Still, we hope to greatly improve upon these preliminary estimates in the future, and in part, I am documenting the details of my work here in

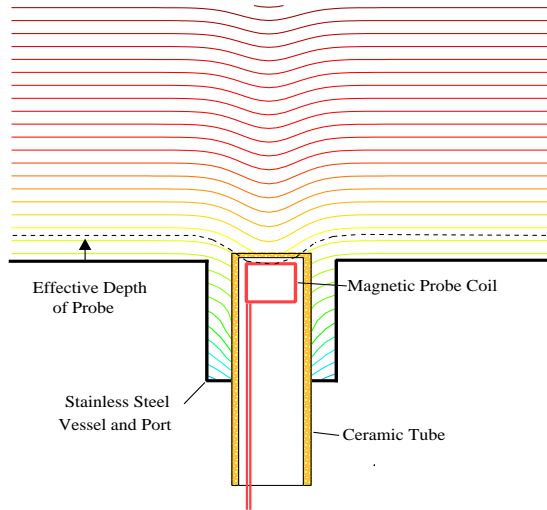


Figure 2.2: Sketch of magnetic probe port and the effect it would have on a uniform field

order to provide a starting point for future work, including some 3-D MHD simulations proposed for the near future.

We want to find the geometric effect on field lines near the port, given that the field is uniform at infinity. There would be some field line that intersects the tip of the probe coil. If we follow this field line away from the port sufficiently far, it will level off uniformly. The effective depth of the probe would then be defined as the distance from the wall of this field line when it is far from the port. Additional calibration factors due to field expansion must also be taken into account. The effect is that the measured field is very strongly dependent on the exact radial position of the probes. The interior fields of the CT are several times larger than what we would expect without these additional calibration factors. During the previous calibration of our probes these field expansion effects should have been implicitly taken into account via the method that was used. After several theoretical considerations have been made will compare predicted and measured calibration factors.

To tackle these issues we can consider a variety of approaches. The simplest is to regard the probe well as simply a hole in the vessel wall which we can reasonably approximate as flat. The magnetostatic field near a circular hole in a thin flat conducting plate has a tractable analytic solution expressible as an integral that can be numerically evaluated. [ref jackson] The magnetic field \mathbf{H} has the form $\mathbf{H} = -\nabla \phi_M$ where the magnetostatic potential ϕ_M is given by

$$\phi_M = \begin{cases} -H_0y + \Phi^1(\vec{x}) & \text{if } z > 0 \\ -\Phi^1(\vec{x}) & \text{if } z < 0 \end{cases}$$

This form guarantees that $\mathbf{H} = -\nabla \phi_M$ will approach a constant vector of magnitude H_0 in the y-direction, as you move away from the hole in the upper half space, while the field goes to zero in the lower half plane. Thus, $\Phi^1(\vec{x})$ describes the localized variation away from complete uniformity.

The solution of $\nabla^2 \Phi^1 = 0$ given the boundary conditions of a hole of radius a can be found by Bessel series expansion in cylindrical coordinates (ρ, ϕ, z)

$$\Phi^1(\vec{x}) = \frac{2H_0a^2}{pi} \int_0^\infty dk j_1(ka) e^{-k|z|} J_1(k\rho) \sin \phi \quad (2.9)$$

where $j_1(x) = \frac{\sin x}{x^2} - \frac{\cos x}{x}$ is the spherical Bessel function of order 1, and $J_1(x)$ is just an ordinary Bessel function of the first kind, order 1.

This solution is attractive to work with because it is fully 3-dimensional, so the total flux through a coil oriented arbitrarily in space can be accurately calculated. However, the simplicity of the boundary geometry yields some quantitatively different effects than the actual, more complex, probe well geometry. The root cause of this discrepancy is that in the case of the simple hole, the field is allowed to expand out infinitely into the void beneath the plane, instead of just the finite sized well that we actually have. This means that more total flux enters the hole than would enter the opening of a well. Since more flux enters, the field beneath the plane is stronger for the hole geometry than the well, i.e. the field below the hole is diminished less than it would be inside the well. Then the calibration factor $\frac{H_0}{\langle H \rangle_p}$ due to field diminishment caused by expansion, would be somewhat less in the hole geometry than for a finite well.

Secondly, each field line that enters the hole will go deeper than it will in the case of a finite well. Thus for a given probe position, the resulting effective depth will be noticeably larger for the simple hole than it would be for the finite well.

Since we are primarily seeking an accurate estimate of the effective depth of the probe in order to compare measured field components to those predicted by theory, we need to do a better job at including the effects of the finite well geometry. So, let us consider a few more possible ways to approach the full magnetostatic problem for a finite well.

The most ambitious route would be to perform a similar Bessel series expansion of the potential as above, but with the added complication that two distinct regions would need to be analyzed separately, then a unique solution could be found to the full problem by matching series

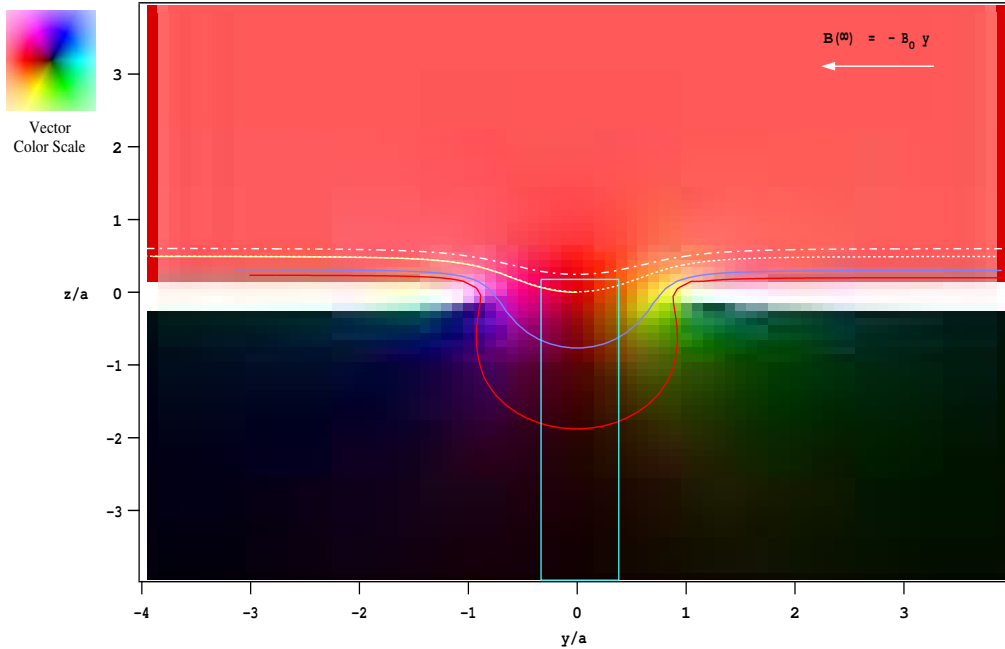


Figure 2.3: Analytic result for magnetic field near a hole in a conducting plane. Here the field vectors are represented by a color-wheel type coloring of the complex plane, which corresponds to the (y, z) directions in physical space. Red indicates a vector pointing directly in the $-y$ direction, while other colors represent vectors at other directions as indicated by the color legend in top left. Vector magnitude is represented by a color's brightness, with black for the zero vector. This color code avoids the “pick-up-stix” effect that can occur with arrow-field representations. A sampling of field lines are also plotted to guide the eye.

coefficients at the interface of the two regions.

The natural choice would be to set one region as the cylindrical volume inside the well, with conducting boundary conditions on the side and base, and the interface matching condition on the top surface. Then the second region would be the upper half space above the plane, with conducting boundary at the $z = 0$ plane, everywhere except for the circular disk where the field needs to match the other region. To implement this, first some analytic simplifications to the general Bessel series would need to be made that take into account the different symmetries of the two regions. Then you would try to see how matching the coefficient at the interface would constrain the form of the solution. However, at this point, progress toward a purely analytic solution begins to fall into that grey unknown between difficult and impossible, and a numerical solution of the system

of coupled integral Fourier-Bessel equations becomes the only tractable option. Then considering that the primary aim of my work was not to spend weeks or months to perfectly solve an advanced 3-D magnetostatic problem by numerical evaluation of Fourier-Bessel equations,I decided to find a simpler, quicker approach.

Since the diameter of the probe coil is relatively small compared with the diameter of the port hole, a 2-D approximation can be made that should be quite accurate for the fields near the central plane of the probe port well. Field expansion effects should be more faithfully recreated by a 2-D solution of the right cross-section geometry than a 3-D solution of the wrong cross-section geometry.

Essentially, the problem in 2-D is equivalent to a field above a conducting plate with an infinitely long trench cut into it, with a rectangular cross-section. If the trench runs in the x-direction, then the solution of the field will be independent of x, it will only vary in the 2-D (y,z) plane. This 2-D solution would correspond to the $x = 0$ plane in the full 3-D problem.

One standard analytic method for dealing with this 2-D problem is the use of conformal mapping. [smythe][F.M. Henderson, Elliptic functions with complex arguments, Univ. Michigan Press 1960, pg 10]. In general it is possible to transform the upper half of the complex plane into the interior of a polygon, by a conformal map according to a straight-forward formula.

For the case at hand, the resulting polygon would be the “upside-down top hat” shape of the vacuum-conductor boundary. It would have four vertices, and interior angles of $\{\frac{3\pi}{2}, \frac{\pi}{2}, \frac{\pi}{2}, \frac{3\pi}{2}\}$. The original untransformed plane is the z-plane, and the transformed plane is the w- plane; the mapping function is $w = w(z)$, which is formulated implicitly through a differential relation:

$$\frac{dw}{dz} = G \frac{(z - c)^{\frac{1}{2}}(z + c)^{\frac{1}{2}}}{(z - 1)^{\frac{1}{2}}(z + 1)^{\frac{1}{2}}} = G \sqrt{\frac{z^2 - c^2}{z^2 - 1}} \quad (2.10)$$

Here, G is a complex constant that accounts for overall scale and orientation of the resulting polygon, and c is a positive real number, where the points $z = \pm c$ get mapped to the vertices at the opening of the well $w = \pm a + bi$, which are labeled points D and A, respectively (see Fig 5). To

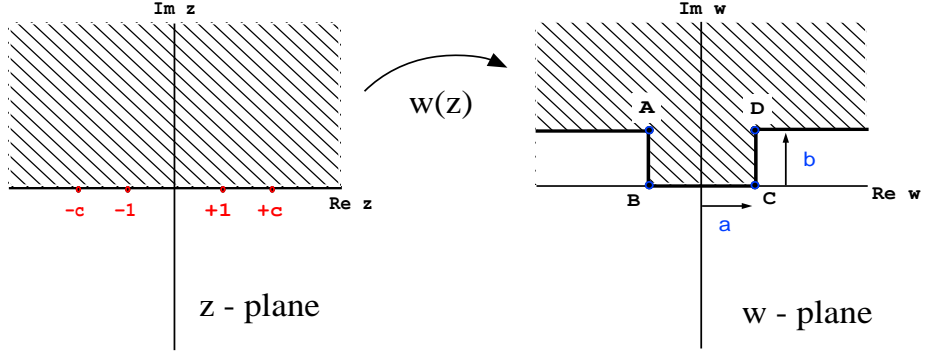


Figure 2.4: Conformal mapping method for 2-D approximation

solve for $w(z)$ we need to take the indefinite path integral, where the integration dummy variable u takes a path from $u = -\infty$ to $u = z$, which is route-independent as long as no branch cuts (along $\text{Im } z = 0$) are crossed. The integral is

$$w(z) = G \int_{-\infty}^z \sqrt{\frac{u^2 - c^2}{u^2 - 1}} du = Gc \int_{-\infty}^z \sqrt{\frac{1 - (\frac{u^2}{c^2})}{1 - u^2}} du \quad (2.11)$$

This integral is not possible to evaluate “analytically” in terms of elementary functions, and does not appear in any standard table of integrals. This is because it corresponds to a combination of elliptic integrals of the second kind, usually notated by $E(k, z)$, here taking a complex argument. Some progress can be made from this point,

$$w(z) = Gc[E(1/c, z) - E(1/c, \infty)] \quad (2.12)$$

and the resulting dimensions of the well radius = a , depth = b , are determined from G and c according to

$$a = Gc[E(1/c) - E(1/c, \infty)], \quad b = Gc[K(\sqrt{1 - (1/c)^2}) - E(\sqrt{1 - (1/c)^2})] \quad (2.13)$$

where $K(k)$ and $E(k)$ are complete elliptic integrals of the first and second kind, respectively. The

proportions of the well, ie the ratio b/a is then independent of G and has the form

$$\frac{b}{a} = \frac{K(\sqrt{1 - (1/c)^2}) - E(\sqrt{1 - (1/c)^2})}{E(1/c) - E(1/c, \infty)} \quad (2.14)$$

It was not too difficult to implement a direct numerical evaluation of the path integral (2.11), and some qualitatively good initial results were obtained.

Once you have the mathematical mechanics set up, it is very easy to find the shape of field lines in the vicinity of the well. You just sequentially evaluate $w_p = w(z_p)$ N times, where $z_p = (x_0 + p \cdot \Delta x) + iy$ for point index taking values of $p \in \{0, 1, 2, \dots, N\}$. This just maps the horizontal line $\text{Im } z = y = \text{constant}$ to the corresponding field line. The resulting array of complex numbers w_p can be plotted to visualize the field line in space.

Furthermore, the effective depth can be found by tracking field lines away from the well and then finding how high above the wall they are after going several hole-radii away from the well. Field expansion ratios can be calculated by comparing the distance between two neighboring field lines, when they are far from the well, vs when they are at the center of the well.

Since the magnitude of the magnetic field is proportional to the density of flux lines, in this way we can get the ratio of the far field to its corresponding value of the distorted near field. To measure the average flux through the probe coil, we just choose one field line that passes through the upper tip of the coil, and a second that passes through the lower tip of the coil. If the distance between these two field lines far from the probe well is δz and the height of the probe coil is Δz_{coil} then the calibration factor due to field expansion is $C_{exp} = \frac{\Delta z_{coil}}{\delta z}$.

The one stumbling block that prevented the full application of this method to solve the problem at hand, is that for reasons not yet understood, the ratio of b/a was not precisely controllable with the algorithms I have implemented. Essentially, only a single value of $b/a \sim 1$ was achievable, regardless of the choice of c and G . An intrinsic part of the problem is that my algorithm was divergent for points close to the real axis in the z -plane. This prevented me from making an accurate determination of what the real b/a ratio was for any particular instance of the mapping. There is

some hope that after some further work with elliptic integrals, the increased insight and experience may lead to a resolution of the bugs in my code. But for the sake of time management, I abandoned this semi-analytic approach and switched to an even simpler fully numeric 2-D iterative relaxation method.

We begin this final (successful) approach with a significant practical simplification. The magnetic field vectors themselves are not really important to find the effective depth and expansion factor, especially if we are only considering a 2-D case. Really we just need to know the shape of the flux surfaces on which the magnetic field lines reside. The simplifications arises from the fact that the magnetostatic potential ϕ_M is what we call the *harmonic dual* of the electrostatic potential ϕ_E .

The concept of harmonic duality is that if two scalar functions satisfy the Laplace equation ($\nabla^2 \phi = 0$, which is the definition of harmonic here) on the same boundary geometry, we say that the functions are dual to each other if one function satisfies Dirichlet boundary conditions ($\phi_1 = \text{constant}$), while the second function satisfies Neumann boundary conditions ($\frac{\partial \phi_2}{\partial n} = \text{constant}$). The result is that equipotential surfaces of ϕ_1 correspond to flux surfaces of ϕ_2 , and vice versa. This is due in part to the fact that equipotential surfaces and the flux surfaces for the same potential function are locally orthogonal to each other. To go from a potential function to its harmonic dual, we just have to interchange the role of equipotentials and flux surfaces, and the resulting potential will still satisfy the Laplace equation, but with the dual boundary condition.

The magnetostatic potential satisfies the Neumann boundary condition at the surface of the conductor, while the electrostatic potential for the same conductor geometry satisfies the Dirichlet boundary condition. Therefore we can find the flux surfaces of the magnetic field by actually computing the equipotential surfaces of the dual electrostatic potential problem. This is an advantage because Dirchelet boundary conditions are intrinsically simpler in that you don't have to evaluate derivatives to apply them, and they lend themselves to numerical solution by iterative relaxation methods.

I have implement a simple Gauss-Seidel method using a 2-step iteration on two interleaved

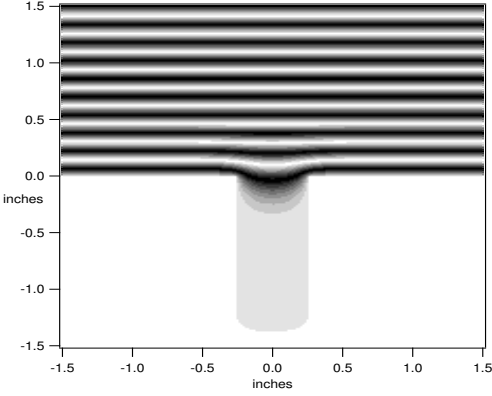


Figure 2.5: 2-D Relaxation simulation result of magnetic field near a conducting port well

square meshes. [ref jackson 1.13 pg 47-50] (see Appendix B for details)

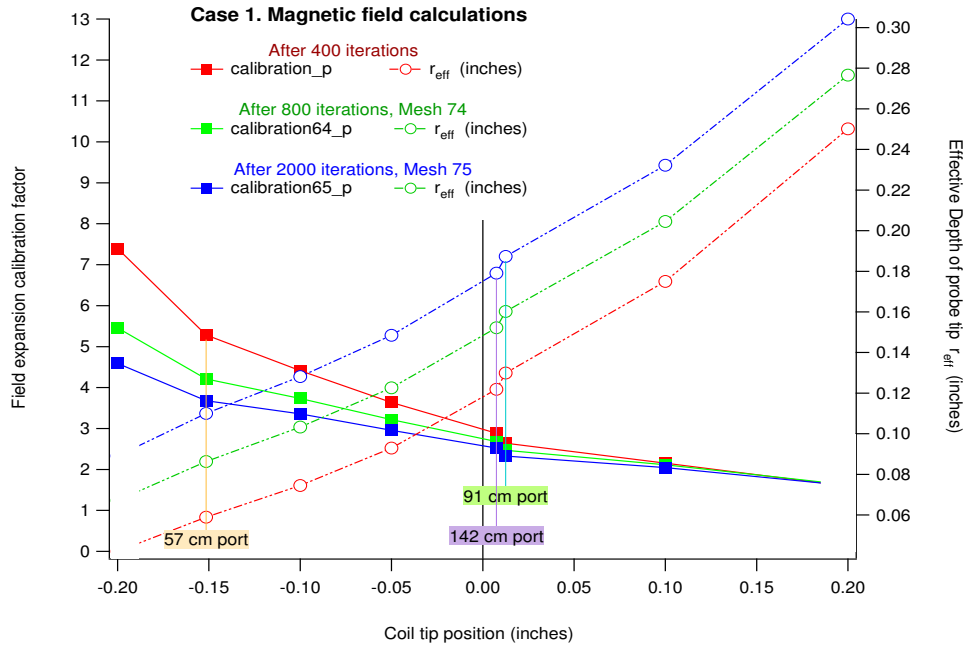


Figure 2.6: Probe position dependent trends in the expansion factor (left) and the effective depth of measurement (right) for magnetic field expansion into full volume of well. Position zero corresponds to the probe coil tip being flush with the inner edge of the port hole.

We also have an independent consideration that leads to similar relative calibration between the primary set of magnetic probes. There is good reason to expect that toward the end of the

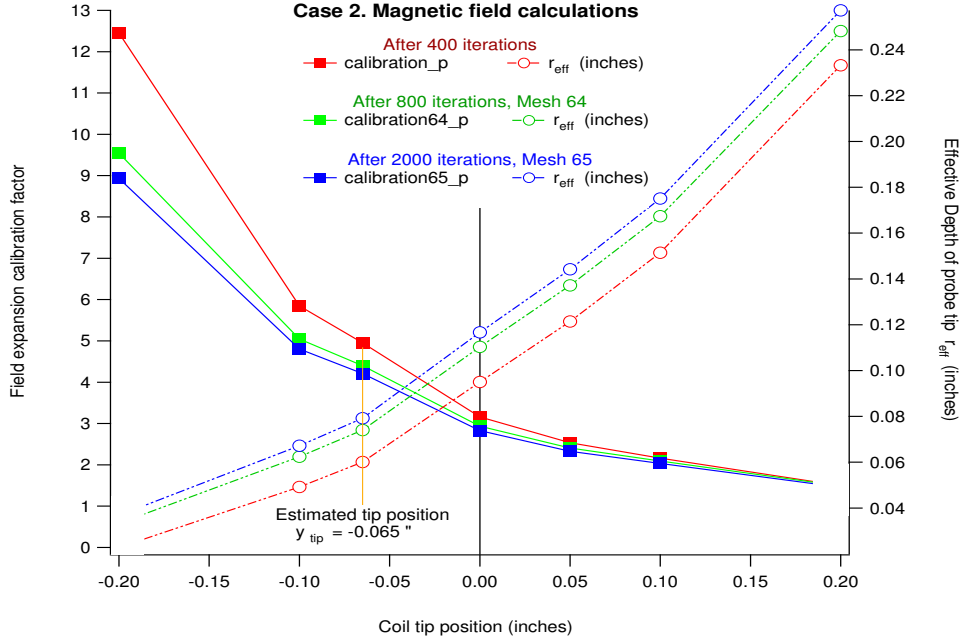


Figure 2.7: Probe position dependent trends in expansion factor (left) and effective depth of measurement (right) for magnetic field expansion into only partial volume of well due to field exclusion by stagnant plasma. Position zero corresponds to the outer surface of the ceramic probe sleeve.

acceleration process the B_θ pushing fields behind the CT should have mostly come to an equilibrium state that is nearly uniform as a function of z . When we look at the actual B_θ data we see a systematic discrepancy between the measurements at the three locations that could either mean a highly reproducible non-uniformity of $B_\theta(z, t)$ that depends on z in an exactly fixed way, or that previous calibration factors for the probes were slightly off by differing amounts. The effect of probe depth in a conducting well of the probe port provides the simplest explanation for this error, and it should be corrected for.

2.3 Lagrangian interpolation of probe signals

Report specific results relevant to magnetic geometry, details of algorithm are left for the appendix. *Analysis finished, but not written yet.*

2.4 Characterization of CT modes

show standard “typical” mode and a variety of non-typical modes show time signals and reconstructed axial dependence at various times

2.5 Comparison between experiment, theory, and simulation

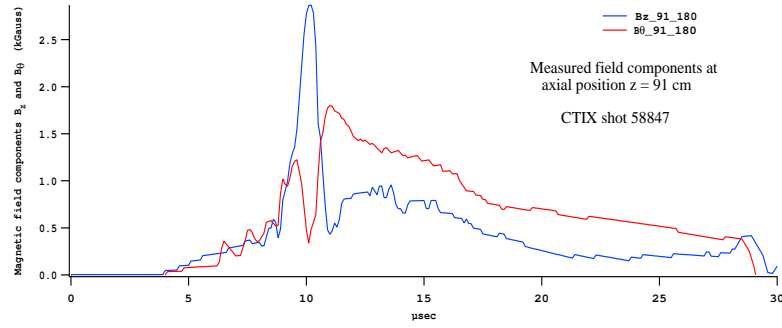


Figure 2.8: Measured magnetic fields at $z = 91$ cm

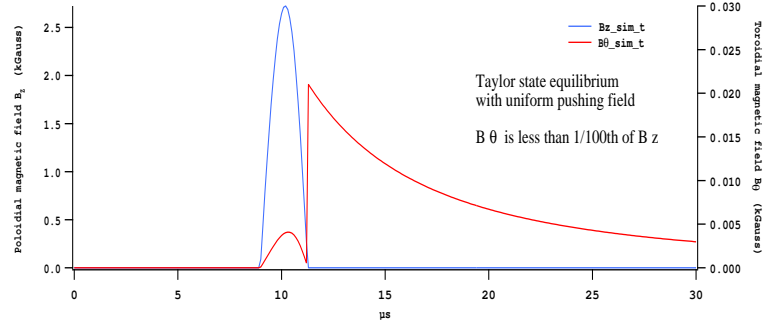


Figure 2.9: Accelerated Taylor equilibrium with axial compression (absolute value of B_θ)

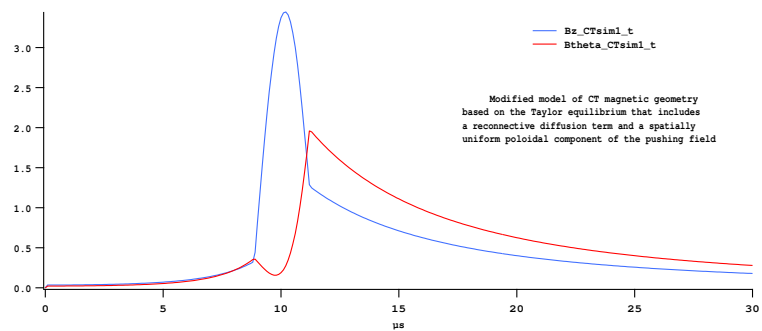


Figure 2.10: Accelerated Taylor-like equilibrium model that is not at an energy minimum, and includes compression and a reconnective diffusion term

Chapter 3

Reconnection and compression experiment

Reconnection within magnetized plasma occurs when two separate regions of magnetic field come in contact in such a way that the magnetic fields of the two regions are oppositely directed in the vicinity of the interface surface (separatrix). A change of the topology of the magnetic field then occurs in which the separate field lines merge at the reconnection zone, and become a single larger field line that now connects the two regions. Reconnection of field lines in a conducting fluid is only possible if the field lines are able to diffuse relative to the fluid. However, due to the high conductivity of laboratory and astrophysical plasmas, classical resistive diffusion rates are far too slow to account for the incredibly rapid rates of field line merging observed in actual reconnection processes such as the tearing mode instability within tokamaks. To explain the anomalously fast diffusion rates that occur within the core of laboratory fusion plasmas, several theoretical models have been proposed. This chapter presents the results of a series of experiments that studied the interaction dynamics that occur when an accelerated compact toroid is injected into a solenoidal target magnetic field, which can be aligned either parallel or anti-parallel to the internal field of

CT at its leading edge. Depending on the alignment direction, MHD predicts that the interaction should result, respectively, in either compression or reconnection of the two fields. This effect has been studied using a fast framing camera that can take a sequence of 12 images of the SCT during the interaction. The images can be taken at rate of one frame every $2 \mu\text{s}$ or at one frame every $0.25\mu\text{s}$. Using these images, the spatial and temporal dependence of light emission intensity of the CT during the interaction is compared to its emission intensity without the external field. The framing camera data is consistent with the data taken on the same set of shots from surface magnetic probes, and laser interferometer measurements of plasma density. *Motivation and relevance to other experimental theoretical results, Questions about driven reconnection, Fast reconnection, resistive MHD. Current sheets Comparison to MRX, Swarthmore. What make this experiment unique.*

3.1 Experimental set-up

In these experiments four external magnetic field coils have been installed on the CTIX accelerator for the purpose of applying magnetic perturbations to CT within the accelerator region. The coils are solenoids concentric with the center axis of the accelerator that produce an axisymmetric B field that is directed along the axis of CTIX near the middle of the coils, but also has a radial component near the ends of the coils. Because the magnetic field produced by the coils is primarily directed axially, we refer to these coils as Axial Field Coils. The direction of the external magnetic field produced by these coils can be aligned either parallel or anti-parallel to the internal field of CT at its leading edge. Depending on the alignment direction, basic resistive MHD predicts that the interaction should result in reconnection of the two fields for the case of anti-parallel alignment, or a compression effect in the case of parallel alignment. These effects have been measured on CTIX using surface magnetic field probes, and a laser interferometer chord at the 142 cm position on the accelerator, and also by using a fast framing camera that images the plasma along an axial line of sight. High reproducibility and high rep-rate allow for a large set of high quality data, and the results

of the three independent diagnostics provide consistent and complementary new information about the reconnection physics within the SCT plasma. Axial field strength can be varied, Observables relevant to reconnection and compression Data sets, number of shots

3.2 Description of external coils

Four external axial field coils are installed on CTIX for the purpose of applying magnetic perturbations to the accelerating SCT. The coils are solenoids concentric with the center axis of the Accelerator, (the z-axis), and located at $z = 65$ cm, $z=100$ cm, $z = 120$ cm, and $z= 148$ cm, as measured from the start of the formation section to the start of each coil. Each coil has 25 turns of 2 cm diameter welding cable. Each coil is L cm long and inner diameter of A, and produce 1.85 Gauss per Amp at coil center.

Insulating acrylic support spools encircle the 16cm OD stainless steel pipe comprising the accelerator section of CTIX. The spools are suspended by an independent support structure that carries the weight of the coils and also maintains a 2 cm gap between the ID of the Acrylic spool and the OD of the SS pipe. This gap is needed because the Accelerator section is charged to high voltage (up to 15 kV) and can heat up to as high as 140 deg F as a result of repeatedly carrying high pulsed current loads (10 kA) during shot runs that can last many hours.

The welding cables have been wound around the spools to form the coils, and connected in series to a variable DC power supply. Each coil can be individually connected or disconnected from the circuit to produce a variety of field geometries. Only 3 of the coils were used for the reconnection/compression experiments, those being the coils at $z= 100$ cm, 120 cm and 148 cm. The coil at $z= 65$ cm was disconnected because early tests indicated that it disrupted the CT formation process when run at high current.

3.3 Diagnostics

The CT location and field structure during the acceleration can be well characterized by surface magnetic field probes that measure the axial component B_z and toroidal component BT of the time dependent magnetic field at three different positions along the accelerator, at z = 57 cm, 91cm, and 142cm.

The closed magnetic structure of the CT results in a localized pulse in the B_z signals that propagates down the accelerator. Under normal operation probe signals show peak B_z fields that remain approximately constant as the CT is accelerated.

Our fast framing camera diagnostic uses an Imacon 790 tube to make 12 visible light images of the plasma during each shot. Each frame is 400 ns in exposure duration, with a time delay of 2 ms between frames. Visible light emission is primarily from impurities in the trailing plasma, and so the framing camera is able to image the plasma sheath in the transition region between the CT field and the purely toroidal field behind the CT that is caused by the rail-gun acceleration current.

The framing camera is well suited for measuring the level of angular variations in plasma density and current density in the CT, as an indicator of the quality of the equilibrium.

For the reconnection experiments the framing camera is very useful because it simultaneously provides a time history of the axial position of the CT, as well as the radial and angular variation in light emission.

Line of sight passes through glass windows and mirrors into an f 4 zoom lens, mounted onto the framing unit. The output phosphor plate is viewed by a 384×576 pixel CCD camera to make a digital image of the shot. Since only visible light can make it out of the vessel, and be imaged by the camera, the diagnostic ability of the framing camera is limited to only observing plasma processes which emit light in the visible.

This means that the CT itself, which is a hydrogen plasma with a high ionization fraction, is not directly observed by the framing camera, (or the spectrometer) since it emits most of its light

in the UV. The framing camera only observes emission by neutral hydrogen atoms, and impurities.

Since neutral atoms are not directly acted on by the accelerating fields they can not be co-moving with the CT given the very fast timescale on which the CT is accelerated and propagates the length of the accelerator.

Impurity ions are directly acted on by the accelerating E and B fields, but because of their larger mass to charge ratio, they are accelerated less than the protons and electron of the CT. This linear centrifuge effect causes the impurities to trail behind the CT, and do not persist within the CT. Thus the framing camera views a halo around the CT, and which can be used to infer CT itself.

The He Ne heterodyne laser interferometer measures the time evolution of line averaged electron density at the three diagnostic port positions on the accelerator.

3.4 Experimental Results for no Target Field

Magnetic field probe data. Probe signals show peak B_z fields that remain approximately constant as the CT is accelerated. Time of flight shows steady acceleration *Reference results of MHD equilibrium paper*

3.5 Results and analysis

Framing camera data. Observe diminished light from in front of center conductor Magnetic field data. Decrease in Peak B_z field as CT enters Axial field. Time of flight shows slight increase in rate of acceleration The toroidal component of B, or B_θ , is important part of the reconnection process. During reconnection, the BT component advances into the external field, ahead of the CT. The signature of the CT itself is a localized B_z component, and high density. The framing camera measures the brightness of the plasma as a function of position and time. We have compared the average of 20 images taken with no axial magnetic field to the average of 20 images taken when the CT is injected into an axial field of - 400 Gauss (in the anti-parallel direction). In the time-sequence

of images below, pixels colored Red show where the plasma was brighter without the axial field, and pixels colored Blue show where the plasma was brighter with the axial magnetic field turned on. For Black pixels there was no difference. We have also compared the average image taken with no axial magnetic field to the average image taken when the CT is injected into an axial field of + 400 Gauss (in the parallel direction). In the time-sequence of images below, pixels colored red show where the plasma was brighter without the axial field, and pixels colored blue show where the plasma was brighter with the axial magnetic field turned on. For black pixels there was no difference in plasma brightness.

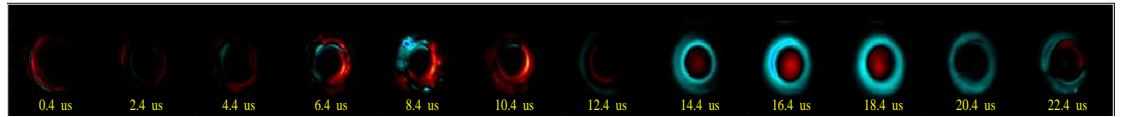


Figure 3.1: Compression effect of axial field on light emission from CT



Figure 3.2: Effect of reconnection with axial field on light emission from CT

When the CT is fired into an anti-parallel magnetic field, we observe a decrease in light emission from the region in front of the center electrode, implying plasma is prevented from filling in this central region. Also we measure the internal field decrease and the CT velocity increase due to interaction with the anti-parallel field. These results are consistent with the effect of resistive MHD magnetic reconnection. Further quantitative analysis on the rate of reconnection are the next step with this project. When the CT is fired into a parallel magnetic field, we observe an increase in light emission from the region between the center electrode and the outer electrode, implying

plasma density and corresponding luminosity greatly increases before the CT is able to leave the accelerator section. We measure the CT velocity slow dramatically and the internal field increase due to interaction with the parallel external field. These results are consistent with the effect of MHD compression Interferometer data Results of Compression Study Magnetic field data. Increase in Peak B_z field as CT enters Axial field. Time of flight shows dramatic decrease in rate of acceleration ($a=0$)Interferometer data. Observe compression effect in increased line averaged electron density measured at $z = 142$ cm position. Density increase by a factor of 1.5 for $B_{AF} = 400$ Gauss Framing camera data: Observed increase of light emission from trailing plasma located in the accelerator section. This implies that trailing plasma is prevented from getting past the compression interaction region.

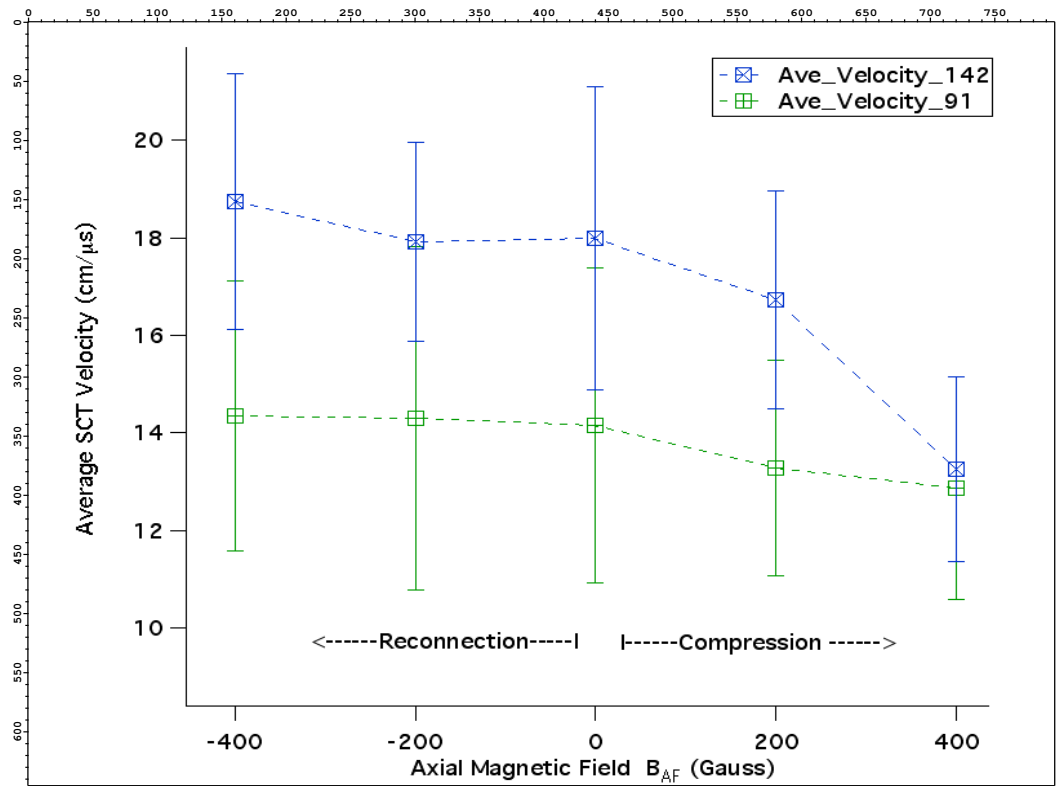


Figure 3.3: Effect of external field on CT velocity

After reconnection, the expected mechanism for plasma fill-in of the region in front of center conductor is Cross-field diffusion. Less plasma is seen in this region for $B_{AF} = -400G$ than for $B_{AF} = 0$. For $B_{AF} = +400G$ most of CT plasma does not leave the end of the center conductor. During the compressional interaction its brightness increases due to the increase in density.

3.6 Model of System

CT field geometry. Axial field geometry. Axial field effects When the Compact Toroid enters an axially directed magnetic field, there is either an attractive force or a repulsive force of interaction between the two fields. This is just like two magnets being brought together along the axis of their poles. Whether the interaction is attractive or repulsive depends on the polarity of the external axial field relative to the internal field of the CT plasma. The magnetic polarity of the CT is fixed, as it is determined by the electrical polarity of the CT formation circuit and formation seed field, while the externally imposed magnetic field can be easily varied in polarity and strength for the sake of experiment. To understand and predict this qualitative effect of either attraction or repulsion, it is simplest to consider the poloidal component of the internal field (the component which is created by toroidal plasma currents), since its geometry is analogous to the field of a simple permanent magnet. In standard operation the CT is accelerated with the North end of its poloidal field at the leading edge, so that the poloidal magnetic field vector (near the center axis) points in the direction of motion, which we call the positive z direction. Then if we were to apply, via a solenoid, an external axial field with its North pole pointing backward toward the oncoming CT, we would expect the two fields to repel each other (North repels North). With the addition of this repulsion force, the CT would accelerate less than normal or it may even decelerate as it enters the target solenoid if the field is strong enough. On the other hand, if we had oriented the external field so that its South pole was facing the CT's North pole as it approached, then we could confidently predict that the CT will be attracted toward the external solenoid (South attracts North). In this configuration the

linear acceleration of the CT will be enhanced above the normal value caused by the rail gun circuit alone. While this simple intuitive model of magnets attracting or repelling one another is correct on a basic level, and does predict the approximate outcome of actual experiments, it leaves out many important and complicating subtleties. The first detail that must be considered is that a compact toroid is a plasma, not a rigid body. It is a conducting fluid with a nearly frozen-in magnetic field, and is capable of compression or expansion. When the CT is accelerated into a repulsive target field we would expect that the CT will be compressed in the z direction since it is being pushed on from both ends, from behind by the pushing field of the accelerator and in front by the repulsive axial field. The CT density and internal field will increase until some sort of pressure balance is reached. Although this compression is relatively straightforward, there are some interesting effects that are possible. Radial variation of the external field can provide a weak spot for the CT to squeeze through. If the external field is high enough reflection of the CT may occur. A very different process occurs when the CT is propelled into an attractive field. In that case, the full complexity of the plasma shows itself during the process of magnetic reconnection. This is a topological change in the structure of the magnetic field in which effective rate of diffusion of magnetic field lines relative to fluid elements typically exceed what would be expected based on the bulk resistivity of the plasma. The two separate magnetic fields merge as the outermost field lines of the compact toroid reconnect with adjacent field lines of the external field; each pair of closed lines becomes a single longer field line that encircles the still distinct inner field lines that have yet to reconnect. This is accompanied by (or mediated by) a layer of strong electric current at the surface of reconnection. The key condition for reconnection is that the magnetic field change sign in at least one component as the surface of interaction is crossed. The second detail is the actual geometry of the internal and external magnetic fields and the boundary conditions that the conducting walls of the vessel apply to the plasma and fields. Reconnection plays a critical role in the dynamo formation process of the CT, it limits the acceleration timescale, and is important when considering injection/refueling into a tokamak type reactor. Produced several new findings about the phenomenon of magnetic reconnection

in the presence of fast plasma flow:Reconnection rate is more than an order of magnitude faster than resistive magnetic diffusion rate, and is comparable to Alven velocity of SCT.Reconnective flux cancellation effect, and SCT kinetic energy gain during reconnection, is proportional to the external axial field strength.Framing camera images have demonstrated the efficient trapping of SCT plasma on the external field lines, and have provided information about the radial dependence of reconnection effects. Measured magnetic compression effects that occur when the SCT is injected into an axial magnetic field. Increase of plasma density by a factor of 1.5 for a target axial field of 400 G , as observed by interferometer data.Increase of peak SCT Bz field strength of 60% as SCT enters axial field of 400 G , as observed by magnetic probe data.Increase of plasma light emission consistent with density increase, as observed by fast framing camera images.

Reconnection Results As the CT enters an axial field that is aligned anti-parallel to the internal field of the CT we observe three main effects with the magnetic probes. First, we observe a significant decrease in the peak value of the Bz field as it propagates into the axial field. This is consistent with magnetic flux cancellation that should occur within the reconnection zone. The amount of reconnective flux cancellation that is observed in our experiment is directly proportional to the strength of the applied external field, with the initial CT field strength being held constant. Secondly, we observe an increase in the acceleration of the CT that is also proportional to the applied external field, with all other accelerator parameters held constant. This means that as reconnection occurs the magnetic energy of the CT is converted into kinetic energy of the plasma's forward motion.Lastly, the toroidal component BT is affected in an unusual way by the reconnection process. During reconnection, the BT component of the CT advances into the external field, ahead of the region where Bz is localized, which is normally considered to be the front edge of the CT. This effect can be understood if the 3D nature of the reconnection is taken into account. Since it is the poloidal components of the CT and external field that are undergoing reconnection, the toroidal component of the CT field (and the associated poloidal current density) is unconstrained in the reconnection

zone and can freely expand into the region ahead of the CT. bringing some diffuse plasma with it. Framing camera data. Observe diminishment of light from in front of center conductor This effect has been studied using a fast framing camera that can take a sequence of 12 images of the CT during the interaction. The images can be taken at rate of one frame every 2 ms or at one frame every 0.25 ms. Using these images, the spatial and temporal dependence of light emission intensity of the CT during the interaction is compared to its emission intensity without the external field. Two very distinct effects are observed in this comparison which shed light on the physics of both compression and reconnection effects. Conclusions based on the framing camera data are consistent with the data taken on the same set of shots from surface magnetic probes that measure the axial variation and time evolution of the magnetic field throughout the system. Compression Magnetic field data. Increase in Peak Bz field as CT enters Axial field. Time of flight shows dramatic decrease in rate of acceleration ($a=0$) Interferometer data. Observe compression effect in increased line averaged electron density measured at $z = 142$ cm position. Density increase by a factor of 1.5 for BAF = 400 Gauss Framing camera data: Observed increase of light emission from trailing plasma located in the accelerator section. This implies that trailing plasma is prevented from getting past the compression interaction region. Each coil can be individually connected or disconnected from the circuit to produce a variety of field geometries. comparison of reconstructed axial dependence of B field signals

Chapter 4

Determination of plasma resistivity

The ability to reconstruct the axial dependence of the magnetic field in the vicinity of the probes due to plasma motion can now be put to use as tool to explore some fundamental physics.

How does the magnetic field evolve in space and time? How does that evolution constrain the effective electrical resistivity of the plasma? How does that measured value of resistivity compare with standard theoretical predictions. If the magnetic field and plasma velocity field are known functions of space and time then the effective resistivity of the plasma, in principle, can be deduced according to

$$\partial_t \mathbf{B} - \nabla \times (\mathbf{v} \times \mathbf{B}) = \eta \nabla^2 \mathbf{B} \quad (4.1)$$

Where η is the electrical resistivity of the fluid. Alternative, we could more directly find the resistivity using a Ohm's law.

$$\mathbf{E} + \mathbf{v} \times \mathbf{B} = \eta \mathbf{j} \quad (4.2)$$

It is clear that these are equivalent to each other since the curl of (4.2) equals (4.1). Then to find the resistivity we just need to evaluate the above combinations of the known quantities. But first we must take notice of the vector nature of the above equations.

In truth η is not really just a number, in the presence of a strong magnetic field its true

properties are best described as a tensor that takes into account the difference of plasma conductivity in the direction parallel to the magnetic field, as compared to its value in the direction perpendicular to the field. This can be phrased in terms the convenient laboratory-framed cylindrical coordinates (r, θ, z) , but with some complications. Let η be a tensor-valued function of position

$$\eta = \begin{pmatrix} \eta_r(\vec{x}) & 0 & 0 \\ 0 & \eta_\theta(\vec{x}) & 0 \\ 0 & 0 & \eta_z(\vec{x}) \end{pmatrix} \quad (4.3)$$

where the dependence on position is simply an artifact due to choosing coordinates that are not locally parallel to \mathbf{B} everywhere. The spatial dependence is purely determined by $\eta(\vec{x}) \cdot \mathbf{B}(\vec{x}) = \eta_{\parallel} \mathbf{B}$, where η_{\parallel} is the parallel resistivity of the plasma, which should be a scalar constant that is approximately uniform over the volume of our system.

What is left over in the η tensor is due to the transverse resistivity η_{\perp} of the plasma

Chapter 5

Temperature measurements

5.1 Particle velocity and energy

In this chapter we will discuss measurements of the electron energy distribution function of the plasma. By taking the first moment of this energy distribution we arrive at the average thermal energy of the electron population, which is proportional to the electron temperature of the plasma for a Maxwellian equilibrium, $\langle E_{thermal} \rangle = \frac{1}{2}nKT_e$. Here n is the number of degrees of freedom that the plasma electrons can move in, which is 3 for our system, and $K = 1.38 \times 10^{-23}\text{J}/\text{K}$ is Boltzmann's constant, and so KT has units of energy. Because the electron and ion populations are distinct interpenetrating fluids, it is possible for them to not be in thermal equilibrium with each other and exist with different energy distribution functions, and different temperatures.

When thinking about the kinetic energy of the plasma particles it is important to distinguish between their drift and thermal velocity components. The drift velocity of the plasma is defined to be the average velocity of all the particles with a macroscopic fluid element, relative to the rest frame of the laboratory. In other words, the drift velocity is the fluid flow velocity of the plasma. It may vary with position, since the fluid elements may be flowing along the streamlines of some non-uniform velocity field.

In the CTIX accelerator, the plasma drift velocity is dominantly in the direction of the axial acceleration, although there may be some smaller toroidal or poloidal component of the velocity of individual fluid elements. On the largest scale however, if we average over all the particles in a thick annular slice at a given axial position, any poloidal rotation of the fluid will average to zero over the cross section, while toroidal rotations may exist but are expected to be much smaller than the dominant axial velocity. This is what we often call the CT velocity, and it is what we can measure with time-of-flight analysis of sequential magnetic probe signals, or with Doppler spectroscopy under certain conditions.

On the other hand, the thermal velocity component of any particle is simply the velocity vector that remains when we subtract the drift velocity from the particle's velocity relative to the lab frame. In this way, a particle's velocity vector is the vector sum of its thermal velocity component, and the drift velocity of the fluid.

$$\mathbf{v}_{particle} = \mathbf{v}_{drift} + \mathbf{v}_{thermal}$$

This thermal velocity will vary randomly in direction and magnitude as we go from particle to particle. We can characterize this random variation by the distribution function of the thermal velocity. We will also separately take account of the drift energy, and the thermal energy of each particle,

$$E_{drift} = \frac{1}{2}mv_{drift}^2 , \quad E_{thermal} = \frac{1}{2}mv_{thermal}^2$$

where m is the mass of the particle.

5.2 Thermalization of electrons

A thermalization effect occurs when a compact toroid is injected into the vacuum magnetic field of the Davis Diverted Torus. Experiments were conducted in which the CT was injected transversely (\perp) into magnetic fields of 105, 150, and 180 Gauss, each defining a distinct data set. Due simply to the net motion of the CT the ions have a drift kinetic energy in the range of 100 eV

to 200 eV. The electrons, in contrast, gain little kinetic energy from the net motion of the plasma, owing to their much smaller mass (1/1856 of the mass of a proton); the net drift contributes no more than 0.1 eV to the electrons, which is insignificant compared to the electron thermal energy of 10 eV or greater.

During the process of collision and reconnection with the magnetic field of DDT the initial velocity field cannot stay directed axially. As the center of mass of the CT is brought to rest the original directed kinetic energy is converted into thermal energy as the anisotropy of the particle velocity field is lost to a more isotropic velocity field in which entropy is maximized. While this basic concept provides a general description of thermalization, it leaves many questions unanswered. A more complete and predictive model would need to delineate the mechanisms that enable the conversion of particle energy to field energy and vice versa, as well as coupling between particles, such as the energy transfer from the ions to the electrons. These mechanisms could include kinetic effects, possibly via collisions, wave growth instabilities, and kinetic damping. Fluid effects could also be important, such as a turbulent cascade of fluid energy down to microscopic dissipative scales, shock heating, and magnetic reconnection. The theory behind these issues is far too extensive to tackle within this dissertation. However, the basics can be outlined, and several new experimental findings can be reported, which may help future work toward confirming existing theories, or guiding the invention of better theories.

The fundamental concept needed to describe the process of thermalization is the distribution function of the thermal energy of the particles; we will notate the energy distribution by $f_E(E)$. The energy distribution function $f_E(E)$ expresses the electron population density as a function of energy. If it is normalized to unity (the convention that I usually prefer), then $f_E(E)$ also represents the probability that any single electron will be found to have a thermal energy in the neighborhood of the energy E .

And of course there are other relevant particle distribution functions. For example $f_E(E)$ is related to the speed distribution by $f_E(E) = J f_v(v(E))$ where v is the speed, or magnitude of

the velocity of a particle, and J is the Jacobian of the transformation $v \rightarrow E(v) = \frac{1}{2}mv^2$. Then $J = |dv(E)/dE| = |(2mE)^{-1/2}|$.

For reference purposes I would like to include some relevant formulas here. The velocity distribution function for a Maxwellian equilibrium of temperature T , with n spatial degrees of freedom, normalized to unity is

$$f(\mathbf{v}) = \left(\frac{m}{2\pi KT} \right)^{\frac{n}{2}} e^{-\frac{m|\mathbf{v}|^2}{2KT}} \quad (5.1)$$

where the n components of \mathbf{v} range over the domain from $-\infty$ to ∞ . Although the velocity distribution depends only on the speed $v = |\mathbf{v}|$, it is critical to remember that the distribution function for the speed v of a particle, ie the speed distribution, is not the same as the velocity distribution. The Maxwellian speed distribution function in the case of $n = 3$ is

$$f_v(v) = \frac{4}{\sqrt{\pi}} \left(\frac{m}{2KT} \right)^{\frac{3}{2}} v^2 e^{-\frac{mv^2}{2KT}} \quad (5.2)$$

where the domain of $f_v(v)$ is $0 \leq v < \infty$. From the speed distribution we can write down the energy distribution function for a Maxwellian system ($n = 3$),

$$f_E(E) = 4\pi^{-\frac{1}{2}} (KT)^{-\frac{3}{2}} m^2 \sqrt{E} e^{-\frac{E}{KT}} \quad (5.3)$$

where the energy is, of course, always positive; $0 \leq E < \infty$.

On the CTIX device, we have successfully measured electron energy using a pair of electrostatic energy analyzers. We found that immediately before the collision/reconnection the electron thermal energy was approximately 30 eV to 40 eV and afterward the thermal energy increases to greater than 70 eV. Ion thermal energy is also expected to increase during the collision, however experimental verification of this effect remains incomplete. An attempt was made to repeat the energy measurement on the ion population using a larger 4-grid Ion Analyzer Probe. This was ultimately not successful. The measurement of ion thermal energy is more challenging due to the larger diameter ion Larmor orbits and certain plasma sheath effects.

A Note on Distribution Functions A quick comment should be included here regarding a difference of terminology. The function that physicists call a distribution function (as I have been using it above), is the same thing that mathematicians somewhat more precisely refer to as a probability density function (or pdf). The math nomenclature does a better job of conveying the meaning of the function because the integral of a pdf over a given interval results in the probability that the continuous random variable will take on a value within the limits of integration. In this way the value of the pdf at any given point represents the density of probability of random occurrence near that point. It reminds us that we need to integrate the pdf to get a value that is actually a probability. To add to this confusion, mathematicians have given the name ‘distribution function’ yet another definition, $F(X)$ which is the integral from $-\infty$ to X of the pdf $f(x)$. The mathematician’s distribution function measures the probability of the event that the random variable will take on a value less than X . This will never be what I mean when I refer to the distribution function of some variable. I will always use ‘distribution function’ as the physicists do, equating it with the mathematician’s pdf. And since my audience is primarily composed of physicists, I will follow their convention and mainly speak in terms of distribution functions.

5.3 Experimental Overview

In our experiments we measured the electron energy distribution before and after it interacts with the DDT target magnetic field using electrostatic energy analyzer probes (EAP) in a variety of configurations. For all of these experiments we measured the initial velocity of the CT as it entered the injection region, as well as the final velocity of the reconnected plasma as it propagated along the field lines of DDT.

We wanted to know how the initial and final states scale with injection energy, and so we repeated the same measurements for three different accelerator settings, CTIX accelerator voltage at 9.5 kV, 12 kV, and 15 kV. For this sequence of data sets, we adjusted the strength of the tokamak

field to follow the increased accelerator voltage, ($B_{DDT} = 105, 150, \text{ and } 180 \text{ G}$). We did this with the intention of maintaining the CT stopping condition. As we will see, because of some accelerator inefficiency, the CT injection velocity did not depend on V_{acc} according to a simple, monotonically increasing function, like we naively expected. Instead, the velocity peaked near 12 kV, and then fell off as the applied accelerator voltage was further increased. The result is that we explored a much broader variety of stopping conditions than we originally planned. [tabulate stopping parameters for the three settings, to show that 9.5 kV data set should not have been stopped by the field] The details of the design and operation of gridded electrostatic energy analyzer probes is presented below, which includes an analysis of simulated data to arrive at an estimate of the experimental error, as well as some statistical results regarding the systematic error due to the analysis algorithm.

5.4 EAP Construction

The probe tip is a hollow cylindrical assembly, 2 cm in diameter, made from anodized aluminum with a moderately large 1 cm diameter aperture to let plasma inside. Within the probe tip are the following components: two circular grids, (the ion repeller grid and control grid), and a circular collector plate. They are stacked together in a sandwich configuration with mica spacers to insulate them from each other and from the case of the probe tip. The probe tip is supported by a 28" long stainless steel shaft which slides through an o-ring vacuum seal to allow the probe to be inserted into the vacuum vessel over a range of depths.

The two grids are tungsten mesh of high transparency, and the collector is tantalum. The two grids and the collector each have a thin nickel wire spot-welded to them that runs back through the shaft and connects to the electronics that operate the probe. By way of these wires the grids can be charged to different potentials and a current can be drawn from the collector plate, and recorded by a digitizer. We will ultimately derive the electron energy distribution function from measurements of how the electron current drawn by the collector plate depends on the applied repeller grid voltage.

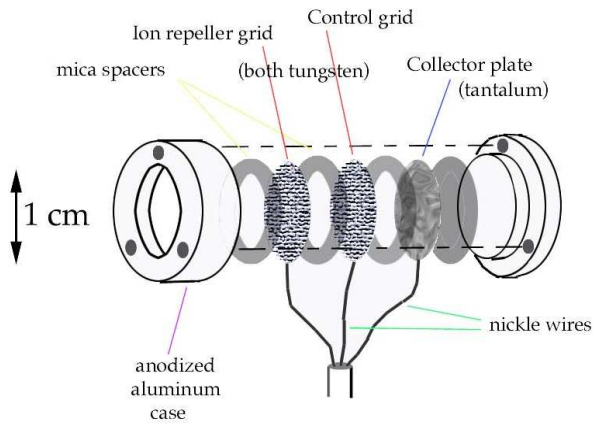


Figure 5.1: Exploded view of EAP showing grids and collector plate

For our experiments the energy analyzer probe tip was positioned at the center of the vacuum vessel with the aperture oriented toward the incoming plasma to have the best opportunity to intercept a good signal. For the injection experiments involving collision/reconnection on DDT target field, the EAP was mounted on the top port 90° from the injection point on DDT, then for the pre-injection measurements, the probe was positioned in the drift section.

5.5 Grid biasing

The functionality of the energy analyzer probe, is achieved primarily by charging the control grid to a negative potential with respect to ground. This potential on a probe is often referred to as the bias voltage or simply the bias. Negatively charged electrons that initially enter the aperture of the probe will feel a repulsive force from this grid. The electric field of the control grid can be thought of as an electrostatic hill standing between the electrons in plasma and the collector plate. This hill will act to separate those electrons which are fast enough to make it over the hill from those which are too slow to get over the hill. All of the electrons that do make it over this hill are

then promptly absorbed into the metal collector plate, causing an AC-coupled negative current to flow across a bias capacitor and then back to the digitizer.

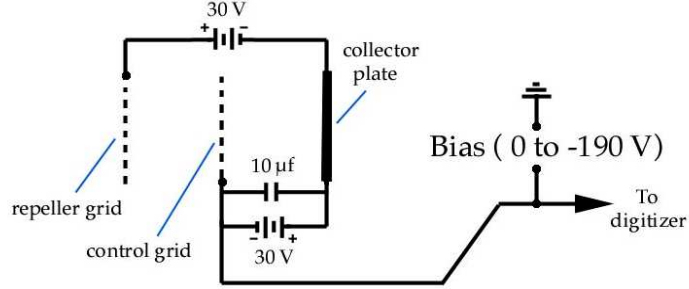


Figure 5.2: Schematic of EAP biasing circuit

The magnitude of this current is directly proportional the total number electrons in the vicinity of the probe which had enough energy to make it over the hill. In Fig. 5.3 we have shown the collector current as a function of time over the course of a typical shot.

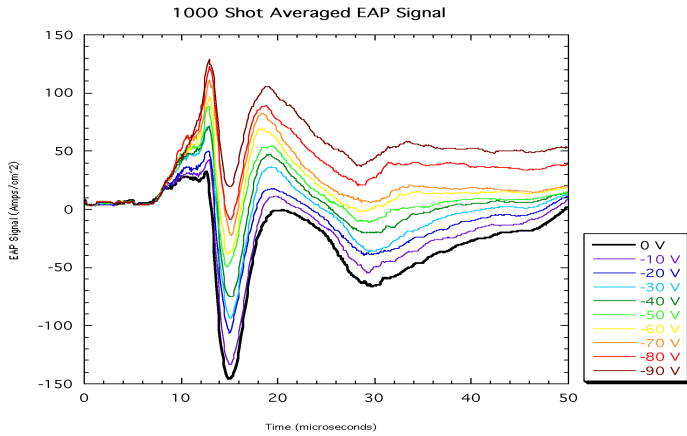


Figure 5.3: Time dependence EAP collector current, parameterized by control bias voltage. As the negative bias is increased a larger electron fraction is repelled. The first strong negative peak in the signal corresponds to the arrival time of the compact toroid.

Now, as we vary the bias voltage applied to the control grid we will repel a variable amount

of electrons, in a manner that is energy dependent. At a larger negative bias, more electrons are repelled by the control grid, letting only the very fastest electrons get to the collector plate, hence a small current is drawn. When we decrease the magnitude of the bias, very few electrons are repelled hence a very large current. At zero bias, all the electrons can get by and so the current has leveled off to a maximum value.

The other grid in the probe, the ion repeller grid, is situated to be the first to encounter incoming plasma and is charged positive in order to prevent ions from entering the interior of the probe. In the simplest possible biasing circuit, the positive bias on the ion repeller grid is accomplished using a high impedance battery, that provides a DC voltage yet blocks the fast signals caused by interaction with the transient plasma.

5.6 Relation between $I(V)$ and $f_E(E)$

Everything that I have already described about the operational mechanism of the EAP, and how it can be used to measure the electron temperature of a plasma can be succinctly summarized in the following integral relationship between $I(V)$ and $f_E(E)$. Because the electron energy distribution $f_E(E)$ measures the probability density of electrons in each infinitesimal slice of energy space, we can express the collector current $I(V)$ as an integral of the electron energy distribution.

$$I(V) = q \cdot \Gamma \int_{qV}^{\infty} f_E(E) dE \quad (5.4)$$

Here, q is the charge of an electron, it works as the conversion factor between V in Volts and E in electron-Volts. This integral counts all of the electrons which have an energy above (qV) , which are collected as electron current by the EAP when the bias voltage is V . Randomness enters our measurements primarily from the electron flux rate $\Gamma = n_e v_e A_{\text{collector}}$ which varies from shot to shot with an approximately Gauss-normal distribution. Here n_e is the electron number density, v_e is the average electron speed (dominated by thermal motion), and $A_{\text{collector}}$ is the area of the collector plate. The physical source of this variation is mostly due to irreproducibility in the total gas output

of the formation gas valve, and also partly due to spatial variations in plasma density and how that density intercepts the probe. Now, it is the current that is experimentally measured, initially as the set of data points making up the I-V scatter plot, one (I, V) point per CTIX shot. We first need to extract an approximate function $I(V)$ from the raw data by some averaging or curve fitting procedure. Once we have the measured $I(V)$, we can solve equation 5.4 for the unknown $f_E(E)$ by differentiating both sides.

$$f_E(E) = \frac{1}{q\Gamma} \frac{dI(V)}{dV} \Big|_{\frac{E}{q}} \quad (5.5)$$

We also see that $V = E/q$ is the bias voltage which is able to repel an electron of energy E .

Lastly, the average thermal energy is computed by taking the first moment of the energy distribution function.

$$\langle E_{thermal} \rangle = \int_0^{\infty} E f_E(E) dE$$

So the experimental task is to find a feasible way to measure the I-V curve with the EAP so that we can differentiate it to get the local electron energy distribution function. In our setup we do not try to measure the energy distribution of the plasma for each individual shot because the desired plasma conditions in the vicinity of EAP are so transient. The plasma wave passes over the probe for only a few microseconds and then is gone. While it is physically possible to sweep the bias over a few hundred volts at a MHz rate, we believe that the cost and inherent difficulties in implementing and operating such a system would overshadow any benefits for measuring the fast plasmas on our experiment.

It is more experimentally feasible to build up the I-V curve point by point, one point for each shot. To make this pointalistic composite of the I-V curve we collected 20 shots per bias voltage setting, with a total of 20 settings from 0 volts to -190 volts in increments of -10 volts. This gave a total of 400 shots per data set in the original post-reconnection measurement of electron temperature.

We were careful not to take all 20 shots for a single bias voltage at once. We broke up the bias settings into even and odd multiples of -10 V. We would first go sequentially through the even

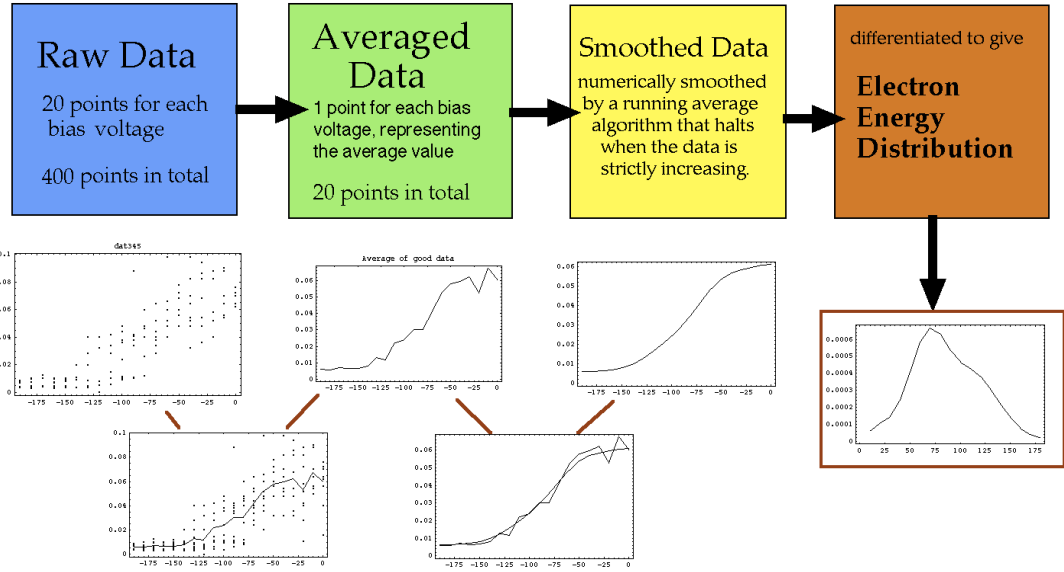


Figure 5.4: Analysis method using moving-window smoothing

set, with 10 shots at each setting, then do a round on the odd set with 10 shots per bias setting.

Then we repeat this to get the second 200 out of 400.

The reason for dividing the scan into several repetitive cycles was to separate out any systematic trends in system performance from the real electron temperature effect. For example, it might be a problem if all the low bias voltage shots were taken at the beginning of the day, and all the high voltage shots at the end of the day. There would no way of knowing that as the device warmed up over the course of the day, variation in the gain of the electronics or in the performance of the accelerator was the real source of the observed trends in the data. Based on the comparison of these divided data sets, we found that there was no measurable systematic variation in the performance of the EAP diagnostic over the course of several weeks of runtime.

5.7 Analysis Methods

Method 1: Two Parameter Nonlinear Fit to a Maxwellian form $I(V)$ Curve. Assumes that plasma is in thermal equilibrium with an effective number of degrees of freedom that must be chosen by the user. Program returns a Temperature and a Normalization Factor. The idea is that if the electrons had a Maxwellian distribution, then the $I(V)$ curve for the EAP should obey some analytically expressible formula. If we evaluate equation 5.4 using the Maxwellian energy distribution given in 5.3, then we find

$$I_{Maxwell}(V) = 1 + \frac{4}{\sqrt{\pi}} m^2 \sqrt{\frac{qV}{KT}} e^{-\frac{qV}{KT}} - \text{Erf} \left(\sqrt{\frac{qV}{KT}} \right) \quad (5.6)$$

Method 2: Non-analytical Free Fitting Method. Using no analytical assumptions about the form of the Energy Distribution Function, this method is able to reconstruct deviations from thermal equilibrium that may exist within the plasma. The Raw Data is averaged, smoothed and then differentiated numerically to yield a discretized plot of the Energy Distribution Function. Both Methods have been implemented and compared.

5.8 Experimental results

graphs ($f(E)$, and velocity histograms, for each DS) with a few comments, and a table

Each of the 10 colored line-plots in the 1000 shot Average is the point-by-point time-dependent average of the 100 shots that were all taken at the same Bias Voltage. On the right are individual EAP signals for two shots that contributed to the 1000-shot average graph. The important features here are first, the strong negative peak that occurs at the time of SCT arrival, and second, the weaker negative pulse that is due to the Trailing Plasma eventually getting to the probe. The top signal was taken with Electron Repeller Bias Voltage set to zero and you can see that both the

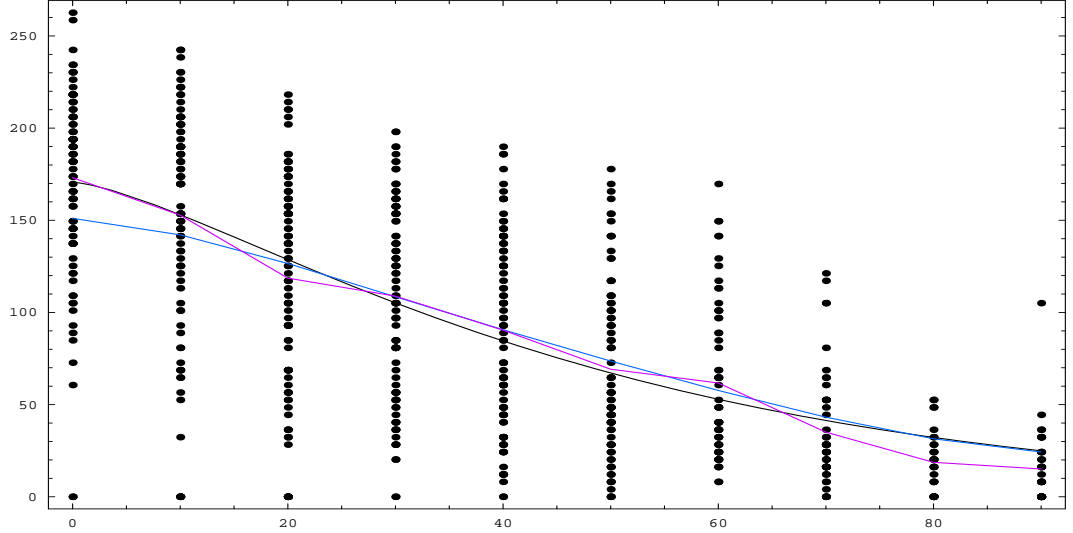


Figure 5.5: Raw data $\{\bullet\}$ with average-value curve $\{\text{violet}\}$, iteratively smoothed curve $\{\text{black}\}$, and Maxwellian fitted I-V curve $\{\text{blue}\}$. The x-axis measures the absolute value of the EAP bias voltage, and the y-axis measures the resulting EAP collector current (arbitrary scale).

Table 5.1: Summary of results from 9.5 kV data set

$V_{acc} = 9.5 \text{ kV}, B_{DDT} = 105 \text{ G}$	<i>Pre-injection</i>	<i>Post-reconnection</i>
Fluid velocity	$13.65 \text{ cm}/\mu\text{s}$	$5.95 \text{ cm}/\mu\text{s}$
Net Ion Kinetic Energy	97.2 eV	18.5 eV
Electron Thermal Energy	unknown	70.1 eV

Table 5.2: Summary of results from 12 kV data set

$V_{acc} = 12 \text{ kV}, B_{DDT} = 150 \text{ G}$	<i>Pre-injection</i>	<i>Post-reconnection</i>
Fluid velocity	$18.4 \text{ cm}/\mu\text{s}$	$14.95 \text{ cm}/\mu\text{s}$
Net Ion Kinetic Energy	176.7 eV	116.6 eV
Electron Thermal Energy	unknown	86.4 eV

Table 5.3: Summary of results from 15 kV data set

$V_{acc} = 15 \text{ kV}, B_{DDT} = 180 \text{ G}$	<i>Pre-injection</i>	<i>Post-reconnection</i>
Fluid velocity	$12.14 \text{ cm}/\mu\text{s}$	$10.26 \text{ cm}/\mu\text{s}$
Net Ion Kinetic Energy	76.9 eV	54.9 eV
Electron Thermal Energy	unknown	80.3 eV

SCT and the Trailing Plasma cause electron current to be collected by the probe. When we increase bias voltage to the -90 V in this lower shot, it is clear that almost all electrons have been repelled.

Pre-injection electron measurements Method 1: Maxwellian Fit Average Thermal Energy = 33.47 eV Errors are unknown

Method 2: Free Fit Average Thermal Energy = 43 eV The Error due to Data Set Size and Quality is $\sigma_{\text{Thermal Energy}}^2 = \pm 2.02788 \text{ eV}$ The Error due to Smoothing is s2Smoothing = $\pm 2 \text{ eV}$

5.9 Error analysis of simulated data

We shall closely examine two cases, one simulation done on with a Maxwellian input distribution and one done with non-Maxwellian input distribution. Here is the Maxwellian energy distribution. [figure ?]It has an average thermal energy of 1.4 (arbitrary units). We integrate this analytically to create the ideal I-V curve, from which we can generate a simulated data set which constitutes the "measured" I-V curve. This is shown below.

This data has 400 points in it, just like a real data set. To make the points scatter, for each bias setting, we generate 20 normal-random numbers from 0 to 2 which have the same standard deviation as the real data set does and we use these numbers as the vertical distance of the data points away from the ideal I-V curve. To do this we just multiplied the 20 normal-random numbers by the height of the ideal I-V curve to get the scatter of points in right relative frame above and below the ideal curve.

If the input and output distributions were wildly different in the simulation, then we would expect that the experimentally measured distribution would also be wildly different from the idealized, physically real distribution. If the input and output distributions were very similar, and this similarity held for a wide range of input curves then we would be guaranteed an equivalent level of similarity between our measured energy distribution and the actual energy distribution of the plasma We then accept the simulated data as being "real" and do our analysis on it.

Below is the energy distribution reconstructed from the data. It has close to the same average thermal energy of 1.44 which differs from the average value of the original by about 3%.

The distribution's shape has spread out quite a bit due to the effects of randomization in creating the simulated data. This is not an error in the average, smooth, differentiate algorithm because when simulations were done with 2000 data points in the set, we reconstructed the proper shape of the distribution quite well.

As the number of data points shrinks, the reconstructed distribution become correspondingly more squashed out. This spreading is due primarily to our data size of 400 points. In addition, different randomizations produced slightly different data sets, and hence slightly different reconstructed energy distributions. This kind of fluctuation was examined informally, and it was observed to be relatively small in the Maxwellian case with 400 points. No simulated sets produced humps where they were none to begin with.

In this way all of the Maxwellian reconstructions were easily identified as being Maxwellian. For comparison, we tried using a non-Maxwellian distribution as the input for the simulation. Here we have the original distribution, its average thermal energy is 3.3. Using the same simulation algorithm as before, we create the “measured” I-V data set as shown below. We then try to reconstruct from this data set and yield the reconstructed energy distribution. While its shape is quite different from the original, its average thermal energy is still very close, 3.46 which is within 4.8% of the original. Many other functional forms were tried as the input for the simulation. Similar results were obtained for all simulations using the same statistics as our actual data sets. In all but a few of these runs, the average value of thermal energy was correctly reconstructed to within 5% of the original.

5.10 Statistical error analysis

The main result from the simulation work was that the average value of thermal energy had a relatively small total error for the size of data sets we are working with. In this section we take this result a step further by deriving exact an relationship between the data set dimensions and

the resulting error in the average thermal energy of the plasma.

We consider a situation where the probe current $I(V)$ has been measured n_V times at the k bias voltage settings, where in general, n_V could take different values at different bias voltages, hence the V index is used to denote this possible dependence. A non-constant n_V could easily occur in a real life experimental data set, where system failures of one sort or another could require that data from certain shots be excluded from the dataset. The result would be a slightly patchy scan of the parameter space, where more good data was gathered for some voltage settings than for others.

[figure I-V raw data, caption: n_V samples of probe current k bias voltage settings]

To get the Energy Distribution the data is averaged, smoothed until it is a well-behaved monotonic function, and finally differentiated to yield the Energy Distribution.

[figure]I-V raw data Average Data Smooth Data Energy Distr.

For now, will ignore the smoothing step, which only acts to decrease the error by bringing the data closer to the real distribution. Without the smoothing step we will be looking at upper bounds for the errors involved with this sampling process. The variable Γ was observed to be normally distributed about the mean density.

Because each $I(V)$ measurement depends on the random variable Γ and a monotonic function of V , the variance of the I data at V obeys

$$\sigma^2(V) = \sigma^2(0) \cdot \int_{qV}^{\infty} f_E(E) dE \quad (5.7)$$

Note that the variance at $V = 0$ should be equivalent to variance that describes how the electron flux rate Γ is randomly distributed, ie $\sigma^2(0) \equiv \sigma_{\Gamma}^2$.

As mentioned earlier, the random variation in $I(V)$ is due almost entirely to fluctuations in Γ , while the stable dependence on voltage is due entirely to the integral of $f_E(E)$, and so the variance will decrease with increasing $|V|$.

This condition is useful as an indicator of whether or not the probe is really working. If $\sigma^2(V)$ doesn't decrease then there is a problem with the probe. Error bars for the values of the

$I(V)$ curve at each voltage can then be estimated from the measured $\sigma^2(V)$ and the number of data points n_V at that energy. For each voltage setting, the variance of the average value of the (n_V) probe current measurements is related to the variance of the measurements themselves, according to

$$\sigma_{ave}^2(V) = \frac{\sigma^2(V)}{n_V} \quad (5.8)$$

Of more importance to this study is an upper bound on the error of the average thermal energy, quantified by the variance first moment of $f_E(E)$. We used moment generating functions to make the transformation from the variances of the individual measurements to the variance of the error in the average thermal energy. The resulting total variance is just the sum of the variances of the average value at each voltage V_1, V_2, \dots, V_k .

$$\sigma_{thermal\ error}^2 = \frac{\sigma^2(V_1)}{n_{V_1}} + \frac{\sigma^2(V_2)}{n_{V_2}} + \dots + \frac{\sigma^2(V_k)}{n_{V_k}} \quad (5.9)$$

The key feature in this expression is that the error will tend to grow linearly with k , ie the number of bias voltage settings in the scan(also the number of terms in this sum). It must be noted that it does not work to try to minimize the error by taking $k = 1$, since your choice of that single voltage setting will dominate the final answer. Enough voltage settings must be included in order to have a minimum amount of energy resolution to consider the final result a reasonable approximation to the distribution function. With that in mind, k should be at least 10, and then n must be chosen to be large enough to bring down the error. ($k = 10$, $n = 200$ are good values to plan an experiment around).

5.11 Effect of smoothing

5.12 Summary of results

The simulation has shown the limitation of accuracy of our experimental method when only 400 data points are taken. The exact shape of the distribution can not be trusted, except that

if it has some lumps in it is very unlikely to be from a Maxwellian plasma. If it has no lumps, the physically real energy distribution still has a chance of being non-Maxwellian. On the other hand we can put more confidence in the average thermal energy of the distribution.

The simulation has shown that our analysis on 400 data points is fairly robust with respect to this average value, and we can expect that with our real data we have correctly reconstructed the average thermal energy of the plasma to within 5%.

When we compare the results of the EAP study to the results of Time of Flight study we find that the final electron thermal energy is comparable to final ion kinetic energy. This implies that electrons and ions have gone through some process of equilibration during the collision.

We notice that of the three data sets gathered in this study, the 15 kV and 12 kV sets have similar, non-Maxwellian energy distributions as well as post-collision loss of net flow velocity. The 9.5 kV set had a much greater loss of flow velocity and in addition appeared to have a more Maxwellian shaped distribution. This supports the model that in the 9.5 situation the interaction of the CT with the DDT field results in the plasma coming to a dead stop at the point of injection and then slowly diffusing out into DDT.

Whereas with the 12 and 15 sets, a definite post collision plasma wave propagates through the vacuum field of DDT carrying significant mass and kinetic energy. The primary variable which must be used to account for this difference are gun velocity and DDT field strength. For 12 and 15 the field strength was 150 Gauss and 180 Gauss, respectively. For the 9.5 set the field was only 105 Gauss, yet the gun velocity was higher than for the 15 data set. This could indicate that in 9.5 case the field was not sufficiently strong to capture the CT before it collided with the back wall of the DDT vacuum vessel. If CT-wall collision occurred then the post collision plasma would likely have completely different thermal properties.

Chapter 6

Measurements with high resolution spectrometer

OMA Spectrometer. Measures visible spectrum 300 nm to 670nm. This allows diagnosis of the light emitted by impurity species within the trailing plasma. Two modes of operation are possible. We can integrate over the entire shot, or gate the spectrometer to measure light from a small time interval within the shot. Time evolution of spectrum during the acceleration process can be built up over a sequence of shots in the gated mode by stepping the delay time of the start of the spectrometer gate pulse relative to the time of CT plasma formation. The spectrometer can view the plasma axially via an internal mirror, or transversely through glass window ports. Focusing optics are required for time-gated operation in order to collect enough light into the fiber optic bundle to make detectable light signal at the diffraction plane. [figure of low res OMA time evolution]

A transmission grating spectrometer appropriate for visible light (3500 Å to 6800 Å) was built by Alex Graf¹ in collaboration with EBIT group and was used to study the plasma created by the CTIX machine. The fast time resolution and high spectral resolution are possible due to special

¹Graduate student in UCD Physics Dept.

LLNL fabricated transmission gratings, which the design is based around.

The transmission grating is circular with a diameter 150 mm, groove spacing of 3944.5 Å . Due to its large diameter this grating allows faster integration times, it has an f/3 which is much greater than the f/10 in a conventional spectrometer. It has a demonstrated spectral resolution, $\lambda/\Delta\lambda$, of up to 14500 for a wavelength of 5790.7 Å while using a 50 μm slit (Fig. 1 and 2). The optics within the spectrometer allow for off axis ($\pm 1 \text{ cm}$) input light. [figure 2 = schematic of spectrometer] [ref RSI paper]

My part in the spectrometer project was primarily the development of practical implementations of fast detector arrangements suitable for viewing the CTIX plasma. We constructed a sequence of custom-made adjustable supports for mounting any available fast CCD camera that we had at our disposal into the interior of the spectrometer so that it could record the spectrum image at the dispersion plane. All together, we took data using a sequence of 5 distinct detectors in as many months of run time.

The first experimental task that we completed was a time integrated impurity survey of the light from a helium CT plasma. The spectral resolution is far superior to that of the former device allowing a proper separation and identification of the many features present. This high-resolution survey spectrum spanned most of the visible wavelengths from 3500 Å to 6800 Å . This spectrum was compiled from about 50 individual spectra, and it mapped out the location and relative intensities of hundreds of impurity lines, as well as the primary helium and hydrogen lines. Next we selected the one of the brighter spectral lines for further study. The best candidate was the line transition at 4686 Å of singly charged Helium (He II)

[Graph of line at 4686]

The largest shift expected for a 200 km/s CT is around 4 Å well within the spectral bandwidth of typically 150 Å , while the smallest shift we can detect is at least $\sim 0.4 \text{ Å}$ (less if the light is sufficiently bright).

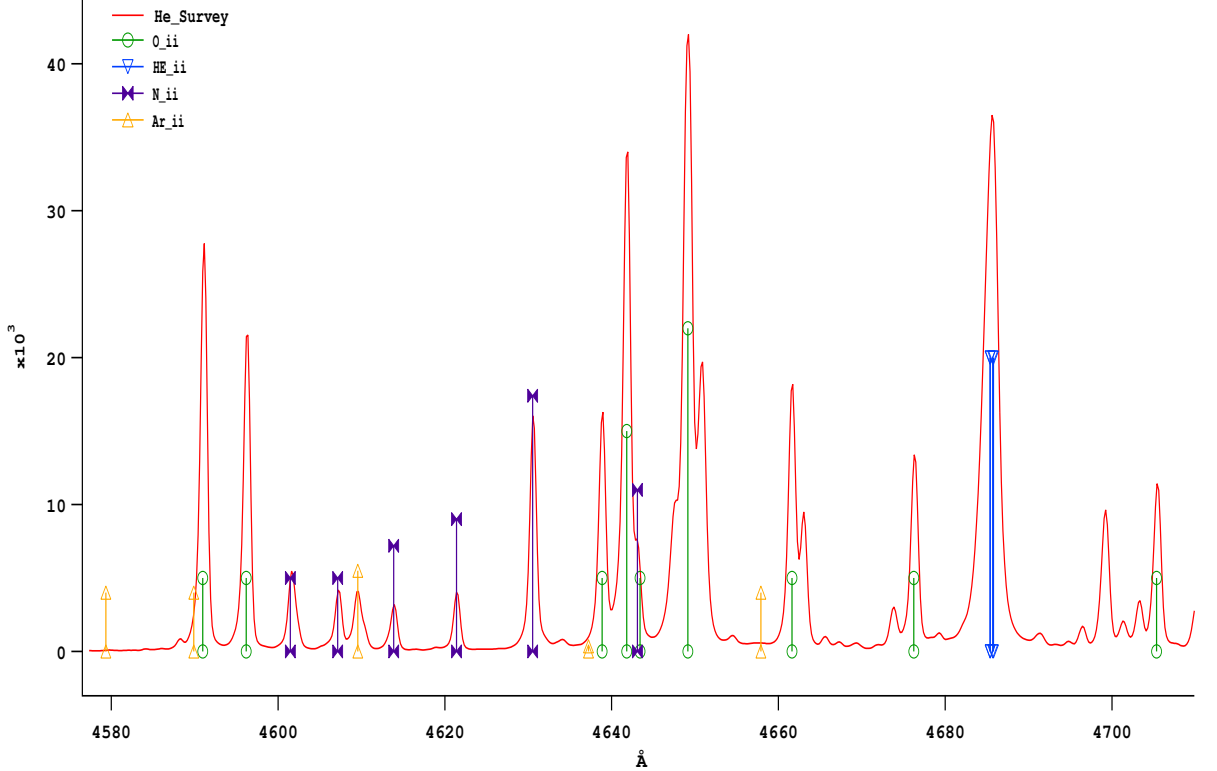


Figure 6.1: Survey spectrum of Helium plasma near He II line

We measured Doppler shifts of this line using an axial line of sight, where the plasma is rapidly moving toward the point of observation. We compared this to spectra that were taken along three different transverse chords that are orthogonal to the direction of plasma motion and so experience no Doppler shift. The spectra along all four of these lines of sight were taken using a time gating method that mapped out the time evolution of the spectral lines and their Doppler shifts in 1 microsecond increments from the moment of plasma breakdown until 30 microseconds after breakdown. During this period the acceleration of the CTIX plasma from 0 to 200 km/s occurs.

The resulting time evolution of Doppler measured plasma velocity was a bit of a surprise at first. Using time gating of the CCD we are able to watch the evolution of ion velocity using the measured Doppler shift at each time step. He II ion velocity peaks very early at 1.5 ms, with a

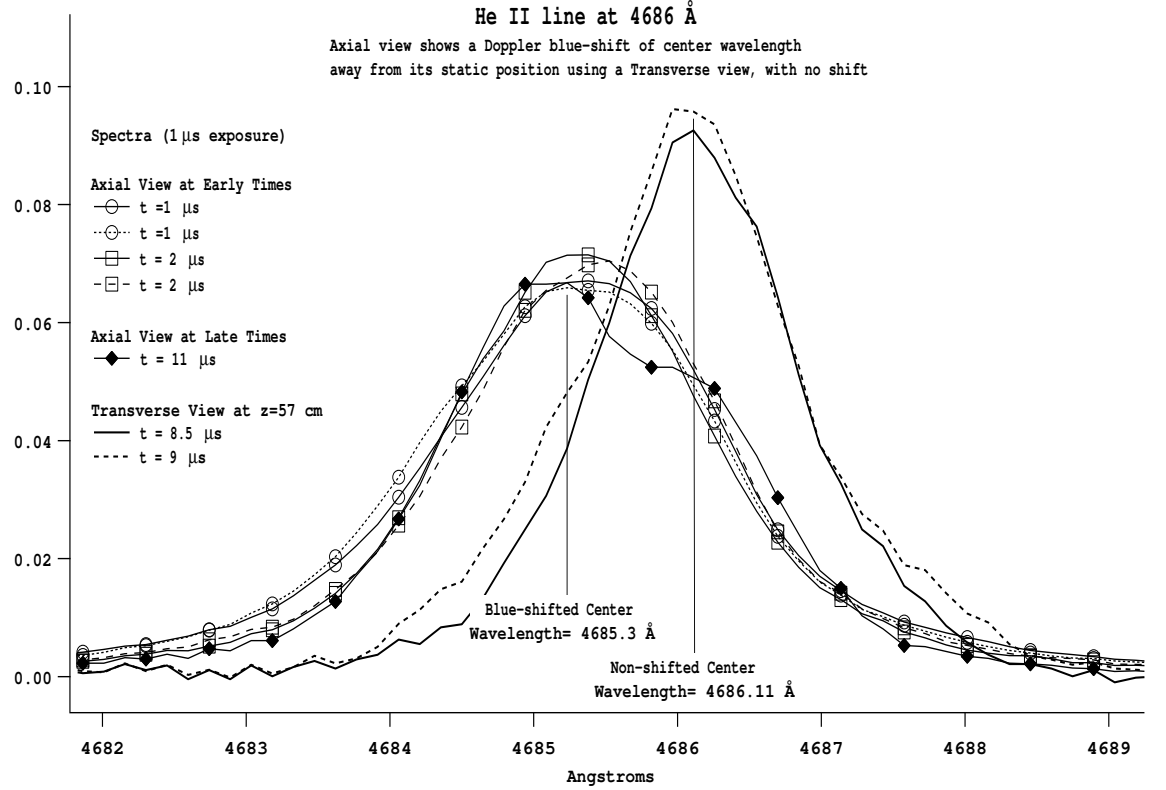


Figure 6.2: Survey spectrum of Helium plasma near He II line

maximum of ~ 50 km/s and then dwindle to only 10 km/s during most of the acceleration of the compact toroid. A second peak of ~ 72 km/s occurs at 14 ms, which is coincident with the moment when the CT leave the end of the accelerator, at this time a re-strike occurs at $z = (0$ to 20 cm) due to the ringing of the railgun circuit.

We never saw the plasma reach anything close to the peak velocity of 200 km/s as measured by the time of flight between magnetic probes. And the velocity as a function of time with its double hump shape seemed peculiar.

Why?

6.1 Doppler measurements of plasma velocity

General scope of work. A self-confined, magnetized plasma ring called a Compact Toroid (CT) is accelerated up to speeds of 200 km/s by the CTIX accelerator. Experimental work has been done on CTIX using a high-resolution transmission grating spectrometer, on loan from the EBIT group.

Bound state line spectra of the plasma have been measured that allow identification of plasma impurities and determination of ion velocity during the acceleration process. Doppler shifts of Helium, Argon, Nitrogen, and Oxygen have been measured.

Here we focus on the Helium data. One key practical result is that the fast rate of ionization imposes a limitation to the size of the region where Doppler measurements can be made. The helium data we have gathered shows a dramatic variation of ion density as a function of position and time, which can be accurately modeled within a simple framework.

Survey of visible emission (3650 Å to 6750 Å) Detected Oxygen, Nitrogen, Argon and Carbon, occurring in $Z = 0, 1, 2$ charge states. We ran with Helium as the primary gas in order to measure large Doppler shifts

6.2 Measurement of Average Doppler Velocity

We are looking at a comparison between the transverse spectra and the axial spectra of the line emission of He II ($Z=1$) at $\lambda = 4686 \text{ Å}$.

The transverse spectra have no shift, while the axial spectra show a Doppler blue-shift because the plasma is moving rapidly toward the input fiber. The apparent wavelength of the blue-shifted light is:

$$\lambda = \lambda_0(1 - v/c)$$

where v/c is the ratio of the ion velocity to the speed of light, which is always less than 10^{-4} for the CTIX plasma. Experimentally however, we can not measure the Doppler shift of individual ions. In

our setup, the light from nearly all the ions in the entire volume of plasma is collected by the axial line-of-sight fiber optic. The measured shift in center wavelength is actually a weighted average of the Doppler shift throughout the vessel. And so we can only infer an average fluid velocity based on this average Doppler shifted wavelength.

$$v_{ave}(t) = c \left(1 - \frac{\lambda_{ave}(t)}{\lambda_0} \right) \quad (6.1)$$

where $\lambda_{ave}(t)$ is the experimental average of Doppler shifted center wavelength as measured by the axial line of sight and λ_0 is the unshifted center wavelength of the line emission as determined by the transverse measurements. $\lambda_{ave}(t)$ is found by taking the first moment of the measured line profile.

$$\lambda_{ave}(t) = \frac{1}{N_I(t)} \int_{\lambda_0-\Delta}^{\lambda_0+\Delta} \lambda I(\lambda, t) d\lambda$$

where the normalization of single line of the spectrum at each instant in time is given by

$$N_I(t) = \int_{\lambda_0-\Delta}^{\lambda_0+\Delta} I(\lambda, t) d\lambda$$

Here, $I(\lambda, t)$ is the output signal of the spectrometer when viewing the axial line of sight, calibrated for wavelength but with intensity in arbitrary units. If we assume a Gaussian line shape for emission from an infinitesimal fluid element we can approximate the spectrum as the integral over the axial coordinate z over the length of the accelerator L

$$I(\lambda, t) = \frac{1}{\sigma \sqrt{\pi}} \int_0^L I(z, t) e^{-(\lambda - \lambda_0(1 - v(z, t)/c))^2 / \sigma^2} dz \quad (6.2)$$

where $I(z, t)$ is the intensity of emission at the center wavelength from the fluid element at position z and time t , and σ is the line width. Here $v(z, t)$ denotes the actual fluid velocity of the plasma, which varies in time and position throughout the accelerator. The velocity function of the plasma is not known for all (z, t) but it is strongly constrained by measurements of the average

velocity determined by the time of flight between signals of magnetic probes at three axial positions along the acceleration section.

Also, the results of 2-D MHD simulation of the accelerator dynamics of CTIX provide accurate approximations to $v(z, t)$. However, one of the goals of this spectroscopic work is to find an independent measure of $v(z, t)$ that can be compared to other results as a check of accuracy. Using the above expression for $I(\lambda, t)$ we can evaluate $v_{ave}(t)$. After some simplification we find

$$v_{ave}(t) = \frac{1}{N_I(t)} \int_0^L I(z, t)v(z, t)dz \quad (6.3)$$

The emission intensity $I(z, t)$ is of key importance. We have endeavored to measure it as directly as possible with the use of narrow bandpass filtered photomultiplier tube measurements made simultaneously at several positions along the length of the accelerator. These measurements can be analyzed using the Lagrangian interpolation technique, in synthesis with the magnetic field data. Additionally, our understanding of the basic ionization and excitation mechanisms can be used to make a simple predictive model of the accelerated helium ions in our system. Ultimately we would like to compare the average velocity evolution measured via Doppler spectroscopy to the results from the two other independent methods, the PMT-Magnetic composite of $I(z, t)$ the yields $v_{ave}(t)$, and a purely theoretic approach.

In the light of this possible cross-comparison of methods, the geometric complication of the axial integrated data is ultimately a good thing since it means that the Doppler measurements provide some constraints on a model of $n_i(z, t)$, which up to this point had been uncharted on the CTIX device.

Ion Velocity Evolution

Using time gating of the CCD we are able to watch the evolution of the average ion velocity using the measured Dopplershift at each time step. Talk about specifics of time gating This analysis

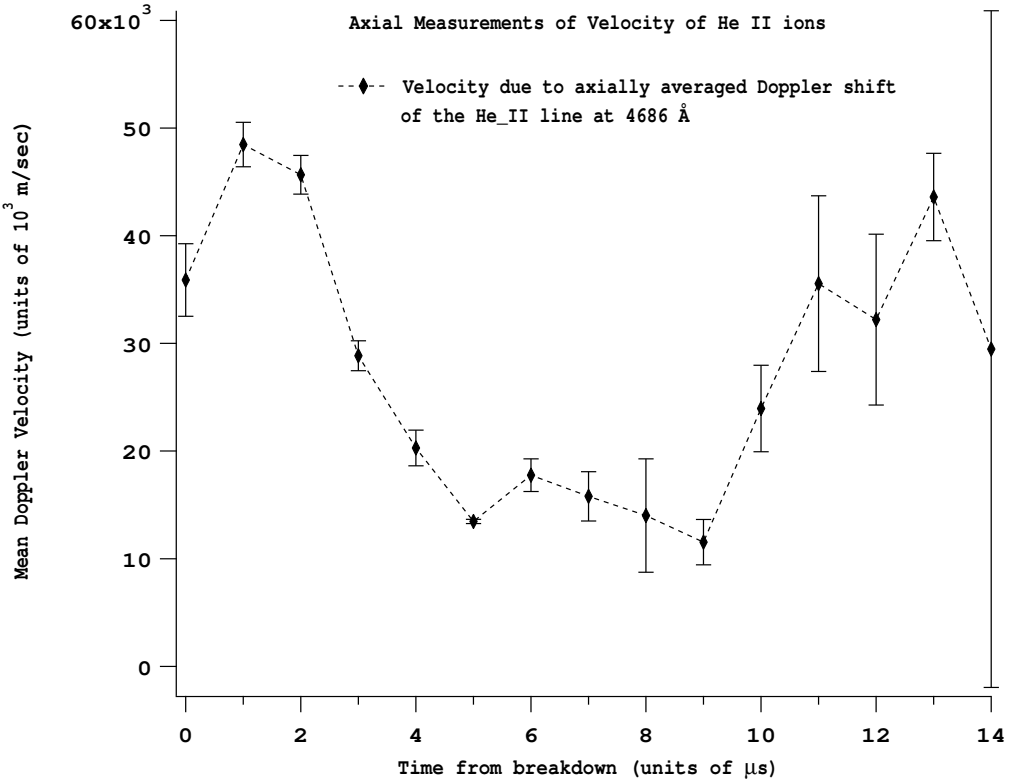


Figure 6.3: Average Doppler velocity as a function of time

shows that He II ion velocity peaks very early at $1.5 \mu\text{s}$, with a maximum of $\sim 50 \text{ km/s}$ and then dwindles to only 10 km/s during most of the acceleration of the compact toroid. This unusual result requires some further explanation. Careful examination of the transverse data show that the He II state becomes extinct as it propagates down the accelerator. Very little is observed at the $z = 91 \text{ cm}$, and absolutely none at all is seen at $z = 142 \text{ cm}$. A second peak of $\sim 72 \text{ km/s}$ occurs at $14 \mu\text{s}$, which is coincident with the moment that the CT becomes fully detached from the end of the accelerator, at this time a re-strike occurs in the formation section ($0 < z < 20 \text{ cm}$) due to the ringing of the rail-gun circuit. It is clear that the maximum velocity measured by the Doppler spectrometer is much less than the CT velocity of 200 km/s as measured by the magnetic probes. The reason for this discrepancy is all in equation 6.8. We have come to understand that because the electron

temperature is sufficiently hot, the population of He II does not last more than a few microseconds during the discharge before it becomes fully ionized. Also He II is also limited in space to the region close to the formation section, because by the time a He II ion gets to the end of the accelerator it has had enough time to turn into an α particle. And so the Doppler spectrometer using the axial line of sight to view the plasma will never see He II ions moving at the maximum plasma velocity. It can only observe them early on in the acceleration process, when velocities are small. The helium ions do in fact get up to the high speeds of 200 km/s or higher, we just can't see them once they lose their last electron. This is a very reasonable interpretation of the data, however it is important to carefully compare the timescales involved in the ionization and acceleration processes and make sure the numbers work out. In the next section we investigate several models and compare them to experimental results.

6.3 Photomultiplier tube measurements

When a charge state is being depleted during the acceleration process, there will be some diminishment of its light emission with increasing axial position. Fast photodiodes with low-noise RF amplifiers were used to measure visible light emissions from the CTIX plasma. The light output of the three accelerator ports, as well as the axial line of sight were monitored in this way.

Optical band-pass filters were used to isolate the light from distinct impurity species and find its evolution as a function of axial position and time. The most general observation we can take away from the photodiode measurements is that across the spectrum, all visible emission was decreasing exponential with increasing axial position. We believe this is primarily due to thermal electron impact ionization.

I was involved in the task of using the results from the high resolution survey spectrum to select a set of optical bandpass filters that allowed light from a limited region (10 nm wide) of the plasma spectrum to be measured by amplified silicon photodiodes. A summer student, Michael

??? from the National Undergraduate Fellowship for Plasma Research constructed three amplified photodiode assemblies with moderate width (10 nm) optical bandpass filters and measured the time evolution of light at the three diagnostic windows along the accelerator section. The visible emission was measured at wavelengths of 465 nm (includes He II, OII, NII), 435 nm (includes OII) and 655nm (includes H α line). For comparison, the total visible light emission was measured without the use of filters.

These measurements gave some circumstantial evidence that the ionization model I proposed was correct. However, they had the problem that the filters took in light from a variety of different line transitions, and so it was not possible to isolate exactly what the He II line at 468.6 nm was doing.

Three quantities were examined in the analysis of this data. First, the time of arrival of the peak signal was used to compare the kinematics of the compact toroid magnetic field and the region of visible light emission. Second, the time difference between the arrival of the peak signal of the filtered light and other signals. Used to look for any separation of ion species in the tail, as the various masses of each might lead to slightly differing acceleration. This was primarily done to test a hypothesized effect of different mass ions becoming separated by the acceleration, similar to a centrifuge. Lastly, the ratio of signal from the filtered photodiode to the unfiltered photodiode, over the duration of each shot. This was used to track the time evolution of atomic processes such as ionization and scrape-off.

Once I began working with the narrow filters, I ran into a number of technical complications that we had not encountered with the wide filters. Initially I had simply plugged the narrow filters into the original photodiode housing, but that suffered from the serious problem that light plasma could enter the filter at all angles from 0 degrees to as large as 30 degrees off of normal incidence.

The critical effect is that the center wavelength of the transmission curve becomes shifted with increasing angle. So non-helium light from neighboring spectral lines could still get through

the filter if they enter at some significant angle. To solve this, I first quantified this effect and found that there is a shift of the center wavelength by approximately 0.1 nm per degree away from normal.

Based on the survey spectra there were neighboring oxygen lines about 0.5 nm on either side of the He II line so we would need to limit the angular acceptance to well below 5 degrees. This has been accomplished with the construction of 9 cm diameter collimator tubes that have a pair of adjustable apertures separated by 55 cm, and internal baffles that block internal reflections.

The narrow bandpass filters are mounted in micrometer adjustable universal joint swivel mounts that allow precise alignment of the plane of the filter to be exactly perpendicular to the axis of the aperture pair. The apertures can be varied in size to optimize the trade-off between angular acceptance and light signal level.

Under typical plasma conditions the angular acceptance can be limited to less than half a degree, while still allowing good light signal. However, many orders of magnitude of the plasma light are thrown away when using the combination of the collimator and the narrow bandpass filter. The resulting light signal was far too dim to be detected by the original silicon photodiode and amplifier circuit. A much more appropriate choice of detector is a photomultiplier tube (PMT). They have nanosecond response times and can be sensitive enough to count single photons. We happened to have an old RCA model 8852 PMT and I was able to borrow two more of the same model from the SSPX group.

[figures showing PD signals as a function of z (logplot)]

As the CT moves down the accelerator it emits less and less light. Fast Photodiode measurements show an exponential decrease of: Total visible light Emission near 465 nm (includes He II, OII, NII) Emission near 435 nm (includes Oxygen II) Emission near 655nm (includes H a line)

6.4 Ionization model

Closed Constant Temperature Ionization Model At the instant of plasma formation there is already a large cloud of moderately high density neutral helium filling the formation section and diffusing lightly out into the accelerator section. Once a small population of energetic electrons becomes liberated within the static electric field, ionization of the neutral proceeds rapidly and the electron and ion densities rise primarily through the process of single electron impact ionization. Figure 2 diagrams the excitation and ionization process that occurs in the CTIX helium plasma. Because the excitation and ionization energies are comparable, if the plasma electron population is hot enough to cause visible line emission from a species, then it also has enough energy to ionize that species into the next higher charge state. It happens that the $\lambda = 4686$ line of He II is one of the brighter lines in the plasma. Its brightness is good for visible spectroscopy because it allows short integration times, however the high magnitude of brightness also means that He II very rapidly becomes fully ionized long before the experiment is over, making it impossible to observe the maximum velocity of the CT via Doppler shifted line emission.[figure 2 = diagram of excitation and ionization process]Electron Temperature Probe measurements show an Electron temperature of $T_e = 54$ eV Electron temperature of $T_e = 54$ eV is high enough to rapidly burn through neutrals and singly charged ions leaving only an α particle plasma that does not emit in the visible.

[figure of electron energy distribution function] comparison of cross sections Recombination rates are small ($a \sim 10^{-14} cm^3 s^{-1}$) Ions will not recombine before the experiment is over ($25\mu s$) because the lifetime of ions (before they recombine) is $1/(a n_e) \sim 1$ second. therefore..

Ionization fraction of the plasma is a monotonically increasing function of time.

The rate of double ionization due to electron impact is more than an order of magnitude smaller than for single ionization, and does not have a significant effect on the lifetime of the He II in the CTIX plasma. First, He II can only loose one more electron before it is fully ionized, so double ionization does not affect He II at all once it has formed. Second, the small effect that

does exist acts primarily to slightly reduce the maximum value of He II density that is obtained during the evolution by allowing a small fraction of the Helium neutrals to bypass the He II state and go straight to the fully ionized state. This does not significantly affect the lifetime of the He II population, and so double electron impact ionization will be ignored. Photo ionization rate?

Formation Region Model In the formation region, where the neutral density is high, the evolution of $n_0(t)$ and $n_i(t)$ are coupled through two first order nonlinear ODE's and an algebraic equation for $n_e(t)$. The density functions can be formulated in terms of the constant $N = n_0(-\infty)$ which is the number density of neutrals before any ionization takes place.

At time $t = 0$ the initial conditions are $n_0(0) = N(1 - \epsilon)$, $n_i(0) = n_e(0) = N\epsilon$ where ϵ is a number much less than one. This model is closed in that no particles enter or leave the volume. However, if we assume that the ionization rates S_0 and S_i (for neutrals and singly charged ions respectively) to be constant in time then some large amount of energy must enter the system to keep the electron temperature constant.

If it is desired, the doubly charged ion density (α -particle density) can be easily accounted for using conservation of nucleons once $n_0(t)$ and $n_i(t)$ are found. The evolution equations are:

$$\frac{dn_0}{dt} = -S_0 n_e n_0 \quad \frac{dn_i}{dt} = -S_i n_e n_i + S_0 n_e n_0 \quad n_e(t) = 2N - 2n_0(t) - n_i(t)$$

We can rephrase this system in terms of dimensionless variables

$$\tau = tS_0N = t/t_0 \quad K = S_i/S_0 \quad \alpha(\tau) = n_0(t)/N \quad \beta(\tau) = n_i(t)/N \quad \gamma(\tau) = n_e(t)/N$$

The evolution equations for α, β, γ are

$$\frac{d\alpha}{d\tau} = -\alpha\gamma \quad \frac{d\beta}{d\tau} = -K\beta\gamma + \alpha\gamma \quad \gamma = 2 - 2\alpha - \beta$$

These have initial conditions $\alpha(0) = 1 - \epsilon$, $\beta(0) = \gamma(0) = \epsilon \ll 1$

If you solve for γ and then combine the two ODE's you can find the path in (α, β) phase space by solving

$$\frac{d\beta}{d\alpha} = (K \frac{\beta}{\alpha} - 1)$$

Provided that $K \neq 1$ then the curve $\beta(\alpha)$ is given by

$$\beta = \frac{1}{1-K}(\alpha^K - \alpha)$$

The evolution of the system can then be fully described in terms of a single variable $\psi = \alpha^{-1}$

$$\frac{d\psi}{d\tau} = -\frac{1}{\alpha^2} \frac{d\alpha}{d\tau} = \frac{\gamma}{\alpha}$$

$$\frac{d\psi}{d\tau} = 2\psi - \frac{1}{1-K}\psi^{1-K} - (2 - \frac{1}{1-K}) \quad (6.4)$$

We do not know if a general closed form solution exists for this equation, and so we have mainly worked with numerical solutions instead. However there is a special case, when $K = 1/2$, in which equation 6.4 can be transformed into a linear equation and solved exactly.

$$\text{For } K = 1/2, \quad \psi(\tau) = (Ae^\tau + 1)^2 \text{ where } A = \sqrt{\frac{1}{1-\epsilon}} - 1$$

This corresponds to a density evolution of

$$n_0(t) = N(Ae^{S_0 N t} + 1)^{-2} \quad (6.5)$$

$$n_i(t) = 2NAe^{S_0 N t}(Ae^{S_0 N t} + 1)^{-2} \quad (6.6)$$

This happens to be a reasonable approximation to the evolution of the helium plasma created in CTIX with its value of $K = 0.57$ based on the calculated cross sections. [figure showing evolution curve in (n_0, n_i) phase space] [figure showing n_0, n_i, n_{ii}, n_e as function of time for typical CTIX plasma parameters]

Accelerator Region Model Because the neutrals are not effected by the electromagnetic fields that accelerate the ions, the slow moving neutrals don't have enough time to make it into the accelerator section during the acceleration of the CT plasma. The absence of neutral helium simplifies the evolution equation for the singly charged ions while they are being accelerated.

We will now consider the evolution of the ion density with respect to a new time variable $t' = t - t_a$ where t_a is the time the fluid element has just entered the acceleration section. The initial condition is $n_i(t' = 0) = N_i$ which is the final ion density $n_i(t_a)$ using the formation region ionization model.

Because some doubly charged ions were created in the formation region, the accelerator initial condition for electron density is $n_e(t' = 0) = N_e = N_i + 2N_{ii}$, again using the formation model to find the doubly charged ion density at the time of entering the accelerator $N_{ii} = n_{ii}(t_a)$. The system evolves according to:

$$\frac{dn_i}{dt'} = -S_i n_e n_i \quad n_e(t') = N_e + N_i - n_i(t')$$

which can be stated more compactly as

$$\frac{dn_i}{dt'} = -S_i n_i (2(N_i + N_{ii}) - n_i(t'))$$

Restated in terms of a few dimensionless variables,

$$\tau' = t' S_i N_i \quad R = N_{ii}/N_i \quad \beta(\tau') = n_i(t')/N_i$$

The evolution equation becomes a logistic equation:

$$\frac{d\beta}{d\tau'} = \beta^2 - 2(1+R)\beta \quad \beta(0) = 1$$

This can be solved to give an exact solution of the ion density evolution in the accelerator region:

$$n_i(t') = 2N_i(1 + R)[(2R + 1)e^{2S_i(N_i + N_{ii})t'} + 1]^{-1}$$

6.5 Conclusions

As diagnostic, a Doppler spectrometer has some unique advantages, and certain limitations that are worthwhile to take into account when planning an experiment in this field.

Unfortunately this effect also puts some constraints on the usefulness of higher Z impurities for visible spectroscopy with our plasma. For a plasma with a moderate electron temperature, there will be a highest charge state that can be obtained from electron impact ionization. For example, consider Ar V ($Z=4$) which is the most strongly charged argon ion that can be created in a $T_e = 100$ eV plasma. If recombination is negligible, then the Ar V will persist until the plasma discharge is complete. This terminal state has bound electrons, unlike fully ionized helium, and so can be made to emit visible light.

The difficulty is that because the excitation and ionization energies are comparable, Ar V only emits very dimly in the visible. If there is not enough energy to ionize, then there is not enough energy to excite. Attempts were made to measure visible line emission of argon ions on the CTIX plasma with no real success so far. The best results were with helium, and in spite of its limitations, the data was very revealing about the basic plasma physics.

6.6 Future work

Plans are underway to improve these Doppler measurements with a new spectrometer, and allowing better optical access using perisopic mirrors placed within the ports on the accelerator

section. The goal is to observe the red shifted light from only the plasma that has passed the port and is accelerating away from it.

Solved for ion velocity this is

$$v = c(1 - \lambda/\lambda_0)$$

$$I(\lambda, t) = \frac{1}{\sigma\sqrt{\pi}} \int_0^L I(z, t) e^{-(\lambda - \lambda_C(z, t))^2 / \sigma^2} dz \quad (6.7)$$

The Doppler shifted center wavelength of line emission from the fluid element at (z, t) is

$$\lambda_C(z, t) = \lambda_0(1 - \frac{v(z, t)}{c})$$

During this process visible light is also emitted when electrons collide with neutrals or ions and exchange an insufficient amount of energy to ionize them. For example, the line emission of neutral helium at $\lambda = 5876$ Angstroms requires a bound electron to be excited from the impact of a plasma electron to an energy of 23.073 eV above the ground state before it can fall down to a lower energy level and emit the photon that we measure. However a bound electron in the ground state of He I can be ionized if it receives an energy of 24.48 eV or more from a collision with a plasma electron. Then the resulting singly charged He II ion has a similar set of possibilities. Its one remaining bound electron can be excited to 51.01 eV above the ground state, and then emit a photon at $\lambda = 4686$ Angstroms, which we then measure with our Doppler spectrometer. Or, that last electron can be liberated from the atom with just 54.403 eV of incident energy, leaving a fully ionized helium nucleus. This helium nucleus, or α particle, has no electrons in a bound state and so it does not emit any line radiation. Because the excitation and ionization energies for most atoms are quite comparable, if a plasma has an electron population that is hot enough to cause visible line emission from a species, then in general, it will also have enough energy to ionize that species into the next higher charge state. This very simple model gives an indication of how quickly the Helium

II state will become extinct under reasonable conditions, and can thereby tell us how long of a time we can expect to observe light emission from the singly charged ions. Once there are no more He II ions left in the system, there will be no more light from the $\lambda = 4686$ spectral line with which to make Doppler measurements. However, there is reason to consider a more accurate ionization model where n_i depends on axial position and time, and take into account what we know about the plasma velocity in order to make a comparison of the experimental Doppler measurement of average velocity and an independent evaluation of the same quantity using the right hand side of equ. 4 and our current understanding of the dynamics of CTIX. So the next task is to consider the effect of ion acceleration relative to a nearly stationary cloud of neutrals, while ionization is occurring.

Constant Temperature Model with Particle Motion In order to account for the ...

Adiabatic Expansion Model Now consider ... If the intensity of light emission due to the specified line transition is proportional to the ion density $I(z, t) \propto n_i(z, t)$ then this reduces to

$$v_{ave}(t) = \frac{1}{N(t)} \int_0^L n_i(z, t) v(z, t) dz \quad N(t) = \int_0^L n_i(z, t) dz \quad (6.8)$$

The weighting function is the normalized density of the ion species we are interested in observing (He II), as a function of axial position and time. Justification of simple proportionality between local number density of charge state and brightness of line emission can be made by looking at the ratio of excitation to ionization cross sections and will be discussed in the following section.

$$\beta = \frac{1}{1 - K} (\alpha^K - \alpha)$$

$$\frac{d\psi}{d\tau} = 2\psi - \frac{1}{1 - K} \psi^{1-K} - \left(2 - \frac{1}{1 - K}\right) \quad (6.9)$$

Chapter 7

Determination of plasma Reynolds number, hydrodynamic and magnetic

7.1 Definitions

Hydrodynamic Reynolds's number

$$Re = LV/\nu$$

= Inertial force/Viscous force

Where ν = fluid viscosity

Magnetic Reynolds's number

$$R_m = \mu_0 LV/\eta$$

$$= \sigma LV$$

= Flow velocity/magnetic diffusion velocity

where η = resistivity, (σ = conductivity), L = length scale of system, V = flow velocity of fluid (plasma in our case).

R_m is a dimensionless parameter that determines the degree to which the magnetic field is effectively frozen-into the fluid.

Different MHD systems with the same R_m will have geometrically similar flow behavior that can be scaled to match each other under a suitable transformation of length and time units.

7.2 Range of accessible values

Chapter 8

Gas puff imaging technique

The CT plasma is composed of fully ionized hydrogen and emits visible light only by exciting bound state impurities. Here we have enhanced light emission by puffing a cloud of neutral helium into the transverse viewing chamber at the end of CTIX.

The neutral gas is injected about a millisecond before the formation of the hydrogen CT plasma. The helium is then excited via electron impact, and emits visible light as the CT plasma washes through the gas puff.

Density fluctuations in the plasma have been detected using fast cameras in addition to plasma density probes and magnetic field probes. Gas puff imaging with high speed cameras are beginning to provide new insight into the plasma physics at work on the CTIX accelerator. In combination with existing diagnostics, wave phenomena and turbulent flow states are being observed. Analysis of this new data is underway, with the hope of understanding the nonlinear physics at work in the CTIX plasma.

Late puffing causes helium to be localized near outlet. A target chamber with large windows (0.5 m by 0.2 m) that allow transverse imaging of a large volume of plasma with fast digital cameras at sub-microsecond exposures. Neutral gas puffing in the target region greatly enhances plasma brightness, and spatial variation of image brightness can be used to infer the spatial fluctuations of

the plasma electron flux density. These fluctuations have been observed with fast intensified and non-intensified cameras, with and without the use of narrow bandpass optical filters.

Some coherent density waves have been measured, and we are working to resolve the structure of shocks and turbulence that are expected to occur in the interaction region. By varying the CT injection velocity, the magnetic Reynolds number of the plasma flow can be controlled, and a large dynamical operating space can be explored. Accelerator gas puffing, timing sequence, valve and pulser design, valve output vs applied voltage.

8.1 Excitation dynamics

We see that light emission as a function of time correlates well with electron density as measured with Langmuir probes (LMP) at floating potential, drawing electron current. The top graph shows the light emission measured along two different chords in the transverse viewing chamber. Photomultiplier tubes (PMT's) were used with a pair of adjustable apertures in order to limit the input light to a narrow chord. The first large peak in both graphs corresponds to the passage of the CT plasma through the drift section, while the second broader peak is the trailing plasma. [ref]

8.2 Implementations on CTIX drift section

8.3 Cameras

8.4 Spectral measurements

8.5 quad PMT and LMP measurements

Chapter 9

Kink dynamics of central column

9.1 GPI results

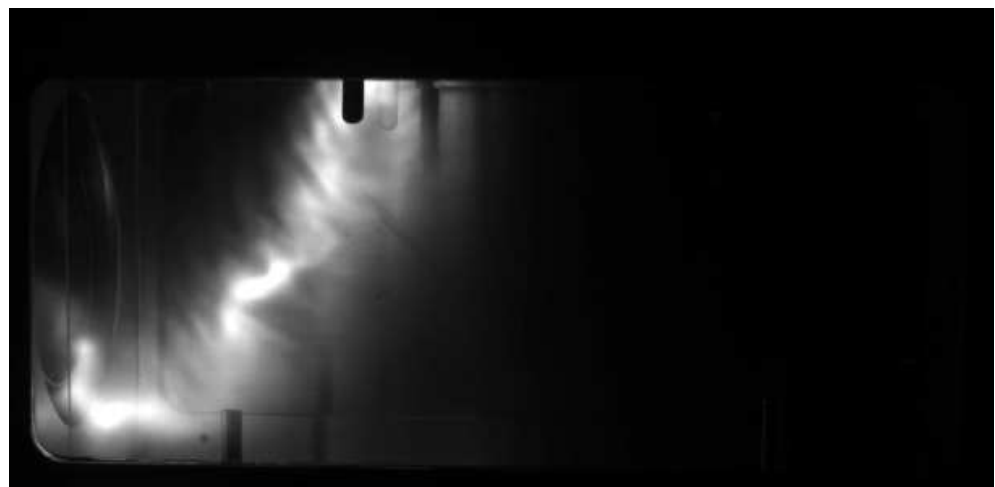


Figure 9.1: Gas puff kink instability caused by accelerator current



Figure 9.2: Gas puff kink instability caused by accelerator current

9.2 Magnetic field results

9.3 Comparison to theory of kink instability

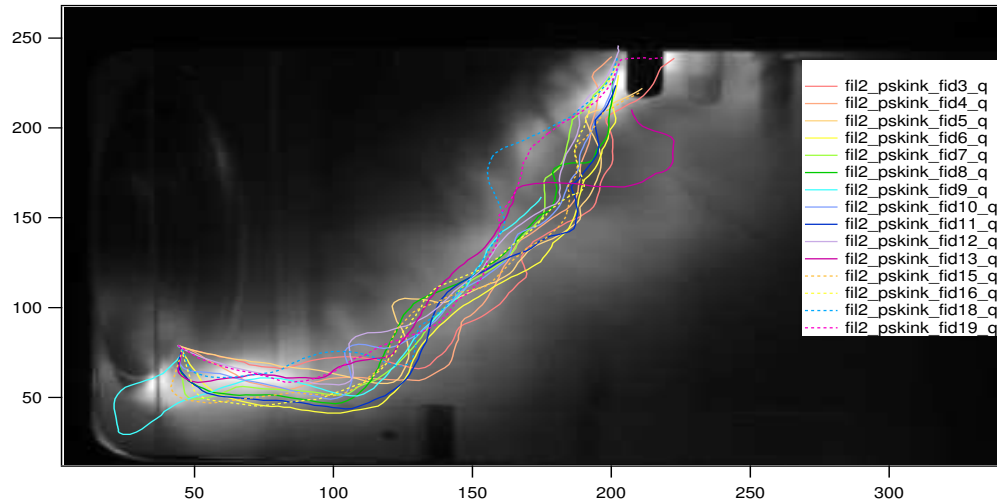


Figure 9.3: Dataset of Kink-effect shots showing the overlay of free-form filament curves for comparison.

Chapter 10

Wire target perturbations

10.1 Target design

mechanical schematic of target, room light image of target description of effect of wire array include image with wire shadows description of effect of glass support tubes, explain implantation of hydrogen, spectroscopic confirmation of light source include images of before and after really bright flare up, and graphs of corresponding spectra rotatablity magnetic probe access pros and cons of design

10.2 Observation of coherent density waves

This graph shows the location of observed plane waves and their approximate wavelength λ and direction. For some shots distinct waves were observed in multiple locations and so are listed separately. There was a noticeable amount of reproducibility of waves occurring in the same location, implying that the waves do not form at random, but instead are caused by some identifiable

mechanism.

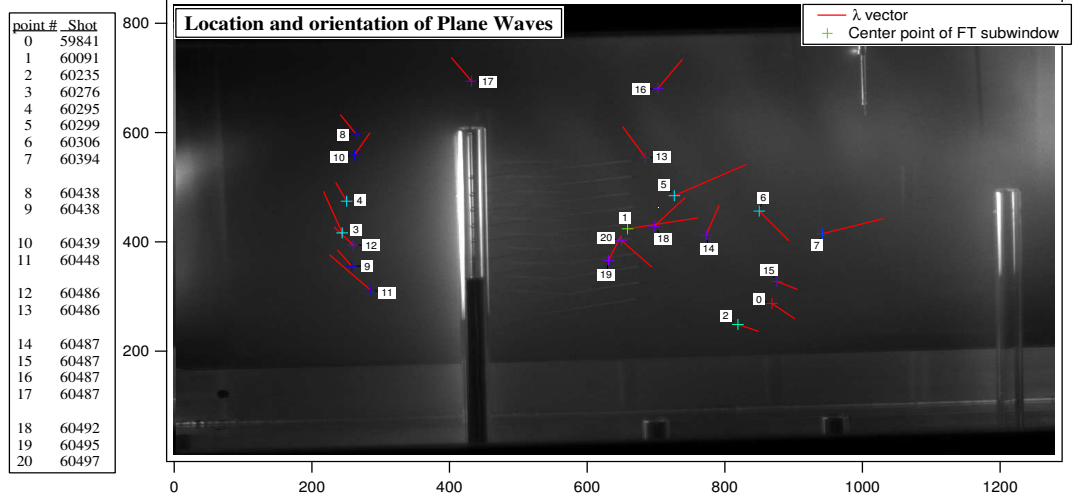


Figure 10.1: Plane wave locations with labels according to shot number.

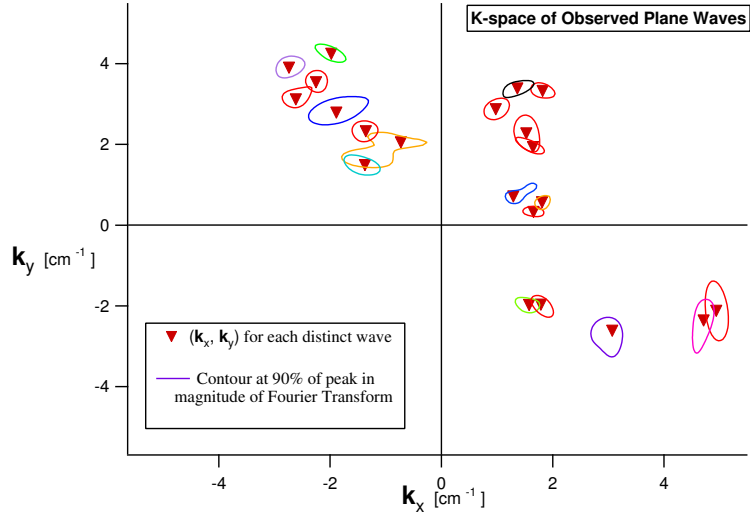


Figure 10.2: K-space distribution of Plane waves

Here are some examples of very localized Fourier modes, which we visually identify as plane waves. Shot 60438 Shot 60295 Shot 59841 Shot 60235

Exposure smear length is the distance the plasma should move during the camera exposure time (of $1 \mu s$), based on time of flight measurements of plasma velocity. Here we compare this length to the wavelength of the plane waves.

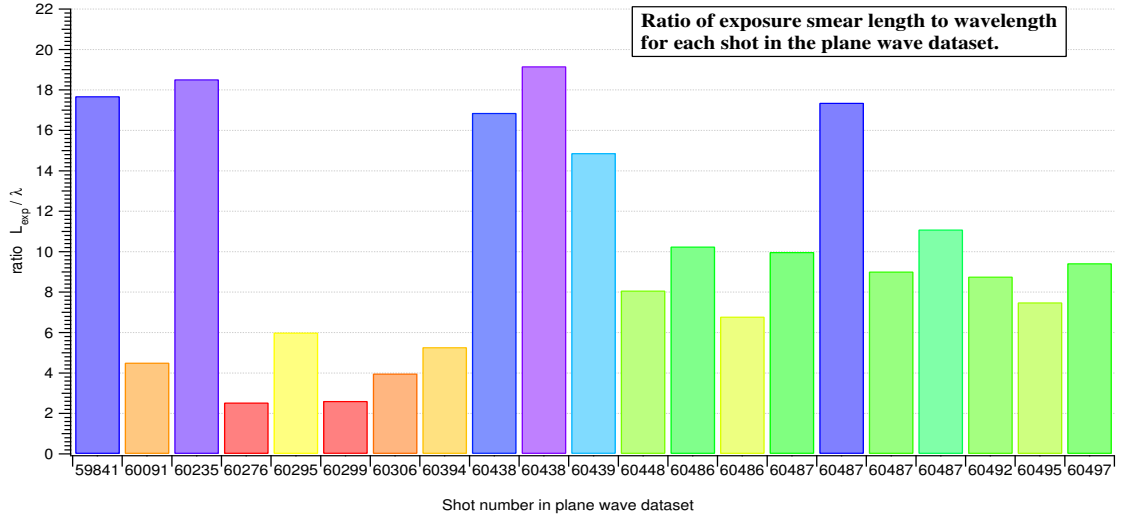


Figure 10.3: Ratio of expected exposure smear length to wavelength is displayed here vs shotnumber of data set.

The curious fact is that if these were plane waves that were co-moving with the plasma at a velocity between 3 to $15 \text{ cm}/\mu\text{s}$, then for an exposure of 1 full μs , we would not be able to resolve the clear wave structures on the order of 1 cm that we do see. If these were co-moving plane waves, the images would be mostly a blur due to the relatively long exposure time, and the fast motion of the plasma. We also see that there is no apparent trend that relates wavelength and plasma flow velocity, such as might be expected from a simple traveling wave with $\lambda f = v_\phi$. This again implies that the wave speed is not the same as the plasma flow speed.

The only viable conclusion is that these waves are essentially standing waves in the laboratory frame of reference, with wave velocities of no more than $1 \text{ cm}/\mu\text{s}$. The mechanism that is responsible for generating these density waves is not fully understood, however we have good reason to expect that the wire targets that were put in place with intention of causing measurable perturbations to the plasma did just that, and the result is that coherent, single-mode density waves

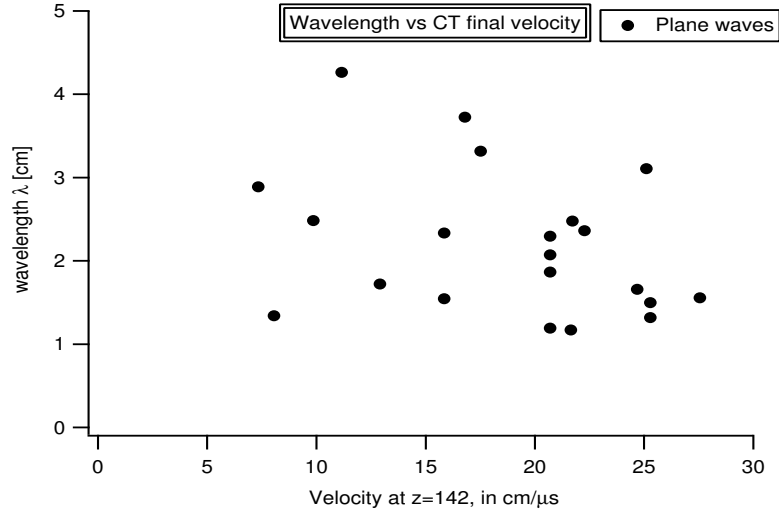


Figure 10.4: Wavelength vs plasma flow speed

are created if the plasma conditions are right. Further analysis on the existing data is required to develop a better model of what causes these, and other wave phenomena in the CTIX plasma. One reasonable model is that the electron density variation is due to the magnetic islands that form as the plasma passes through the wire array. Other possible mechanisms include, shock wave driven ion acoustic modes, or some sort of two stream instability between the moving CT plasma and a stationary singly ionized helium plasma. It is also worth noting that more plane waves of the type discussed above were observed almost exclusively during target region gas puffing. In these shots the CT plasma collided with a stationary neutral population and the result was the appearance of coherent spatial variations in the total plasma luminosity. On the other hand, during shots with accelerator gas puffing, the neutrals had time to become ionized and accelerated by the fields by the time luminous regions of plasma crossed through the transverse viewing chamber. Images of the plasma during these shots had a fundamentally different character than those with the target region gas puffing.



Figure 10.5: Coherent waves in plasma, USE BETTER EXAMPLES

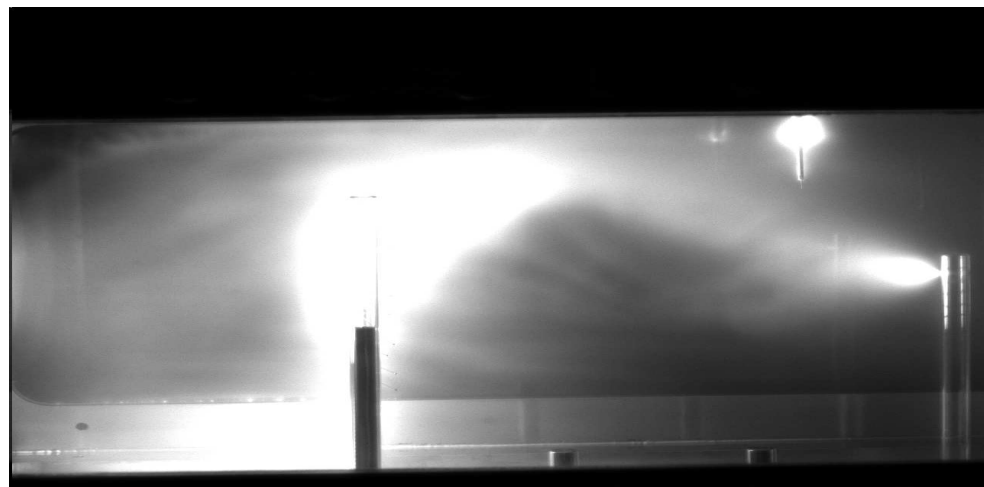


Figure 10.6: Coherent waves in plasma, USE BETTER EXAMPLES

10.3 Observation of turbulent waves

Observation of turbulence during accelerator region gas puff experiments One mode of operation was found to be especially useful for visualizing turbulent flow in the plasma. For example,

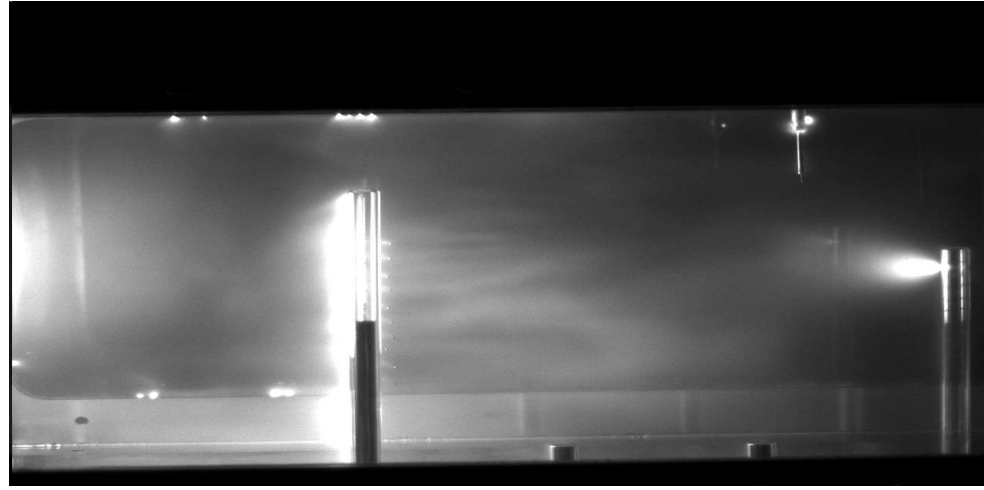


Figure 10.7: Coherent waves in plasma, USE BETTER EXAMPLES

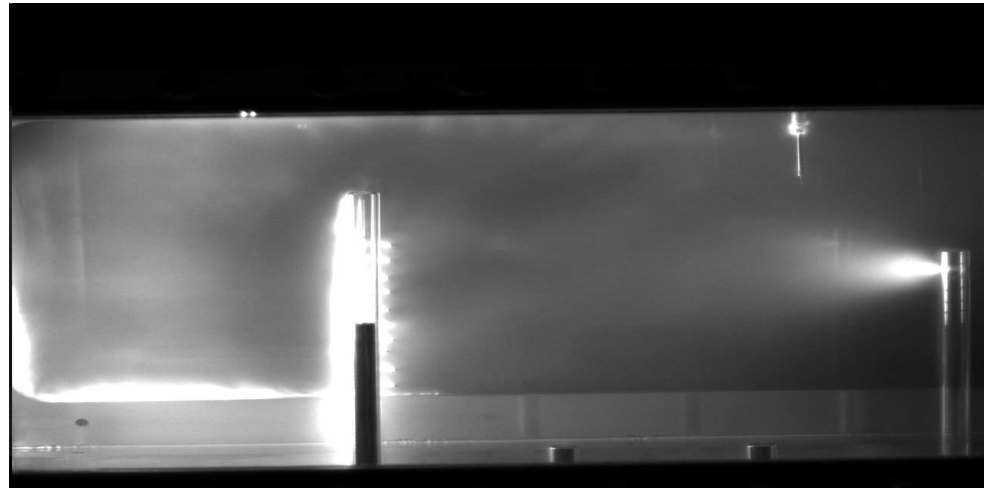


Figure 10.8: Coherent waves in plasma, USE BETTER EXAMPLES

the image taken on CTIX Shot 60062 (Fig 10.10) displays an apparent transition from laminar to turbulent flow as plasma passes wire target and support tubes, traveling from left to right.

The camera exposure for this shot was $1 \mu s$, with a delay of $30 \mu s$ from the formation of the CT plasma. This image is of the relatively uniform B_θ pushing field plasma behind the CT, after the

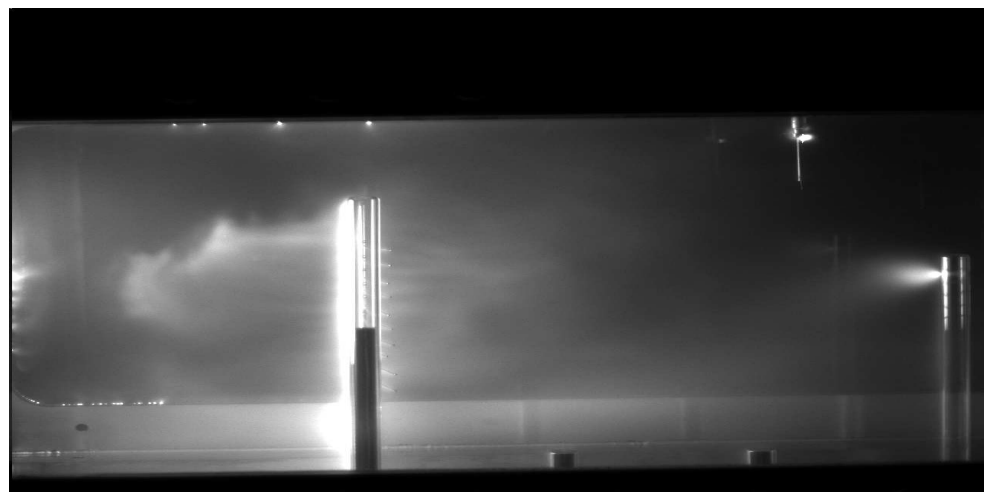


Figure 10.9: Coherent waves in plasma, USE BETTER EXAMPLES

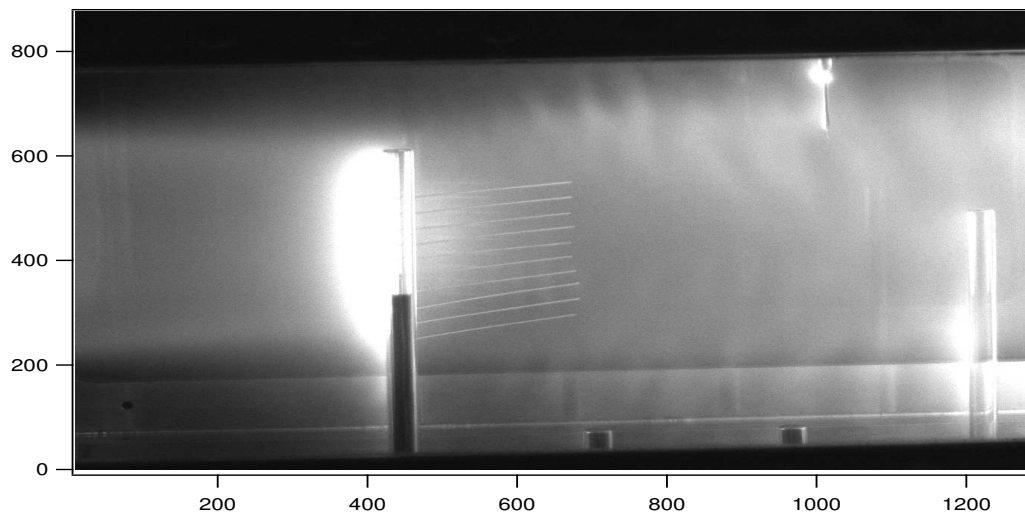


Figure 10.10: Transition to turbulent flow

CT has already moved through the viewing chamber. The helium gas puff was injected into the $z = 91$ cm accelerator port at approximately 14 milliseconds before the shot, which primarily served to increase the plasma electron density by about a factor of 3 for this shot. The secondary effect of the gas puffing is that helium ions (which serve as the dominant source of light for fast imaging) have

a chance to be captured and accelerated by the magnetic fields. By the time they enter the drift section they are co-moving with the plasma and therefore the light emission from these captured ions is indicative of the structure of the flow, and evidence of density fluctuations. When gas puff conditions are just right, this mode of operation is ideal for flow visualization, roughly analogous to using smoke to trace streamlines in wind-tunnel experiments. Injection velocity of SCT for this shot was $3.35 \text{ cm}/\mu\text{s}$. Dominant wavelength of post-target fluctuations for this shot was 2.5 cm.

Top graph in Figure 10.3 is the FT of the plasma flow in the region before it has interacted with the target. Bottom graph is the FT of the plasma after it has interacted with the target. The color scale represents the magnitude of the FT for any given wavevector (k_x, k_y), and the units are arbitrary, but the same for both top and bottom graphs. A significant increase in fluctuation amplitude is observed, as well as wider distribution of waves in the k_y direction. Also the k -spectrum is noticeably more choppy and irregular for the turbulent flow than for the incoming laminar flow. The dominant wave modes in the turbulent spectrum are localized near $k = (2.5, 0)$ [1/cm], where $k = 2\pi/\lambda$. A custom-made discrete Fourier transform algorithm was used instead of a prepackaged FFT algorithm in order to provide more precise control of the resulting resolution in k space. Here are a few other nice examples of apparent laminar-turbulent transition. The time at which the images were taken are listed in parentheses. Shot 60053 (26 μs) Shot 60061 (27 μs) Shot 60055 (30 μs) Shot 60091 (27 μs)

10.4 Comparison of experimental results with plasma turbulence theory

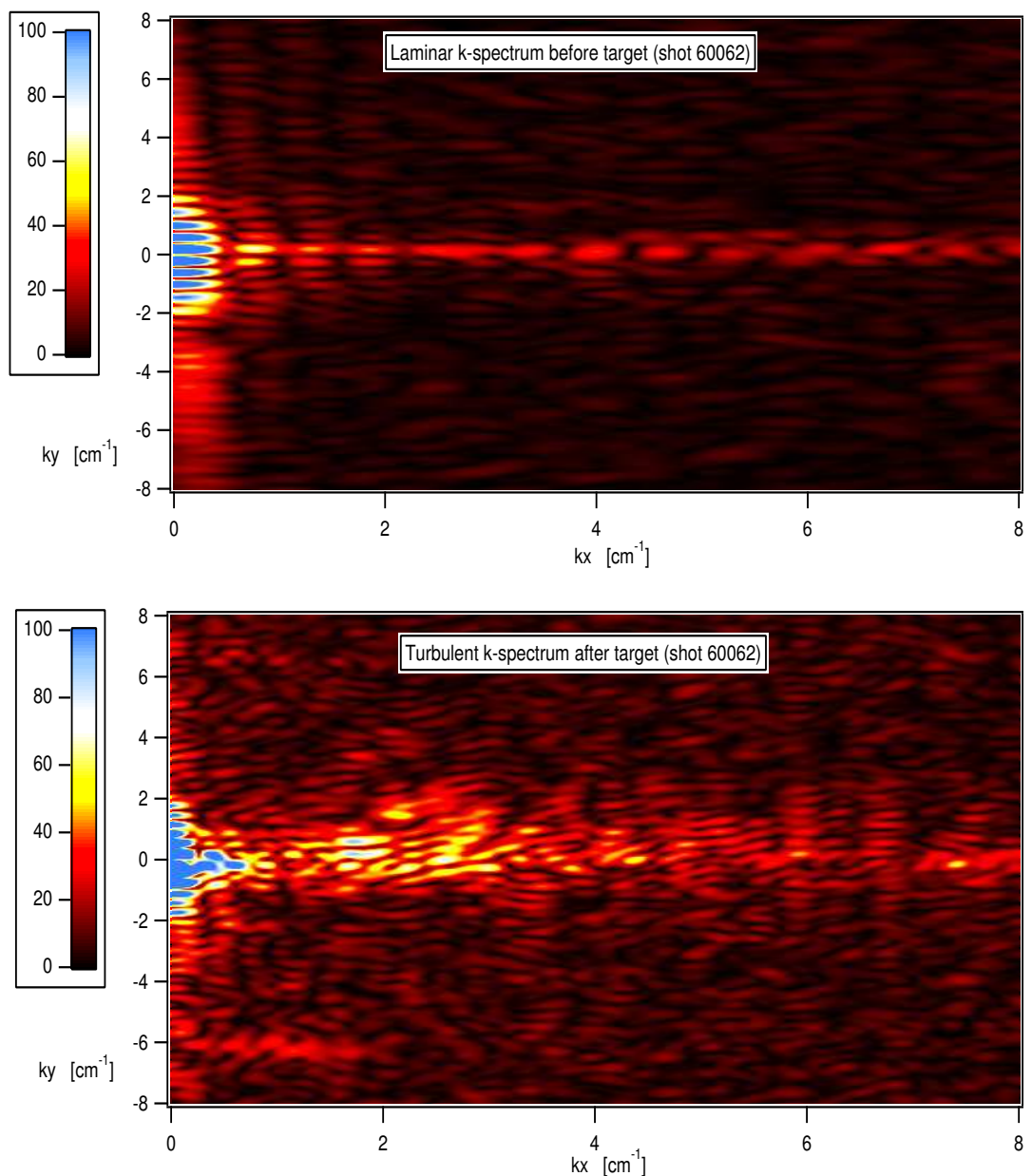


Figure 10.11: Fourier transforms of the image taken for shot 60062,(top) in laminar region before plasma has interacted with target, (bottom) turbulence after interaction.

Appendix A

Magnetic helicity of a CT

The key idea in magnetic relaxation is that short timescale effects such as microturbulence and reconnection cause the magnetic fields to decay and become reconfigured in space in such a way as to find a state of minimum total energy. This minimum is non-zero because the total magnetic helicity of the plasma is a conserved quantity on the MHD timescales, and this provides a constraint on the system. The magnetic field can only become reconfigured in ways that preserve the value of the magnetic helicity $\mathbf{A} \cdot \mathbf{B}$ integrated over the volume of the plasma. In order to measure this constant

$$H = \int_V \mathbf{A} \cdot \mathbf{B} \, dV \quad (\text{A.1})$$

we need to determine the vector potential \mathbf{A} . The magnetic field is curl of the vector potential, and so \mathbf{A} is determined only up to the gradient of a scalar function.

For the case of a force-free field it is sufficiently general to formulate \mathbf{A} in terms of the magnetic field and two scalar functions $\gamma = \gamma(\mathbf{x})$ and $\psi = \psi(\mathbf{x})$ according to

$$\mathbf{A} = \gamma \mathbf{B} + \nabla \psi \quad (\text{A.2})$$

The helicity is gauge invariant for a bounded plasma in a conducting vessel, and the helicity integral

simplifies to

$$\int_V \mathbf{A} \cdot \mathbf{B} \, d\mathbf{V} = \int_V \gamma B^2 \, dV$$

The $\nabla \psi$ term was dealt with by applying a vector identity in combination with $\nabla \cdot \mathbf{B} = 0$, followed by the use of the divergence theorem and the fact that $\mathbf{B} \cdot \mathbf{n} = \mathbf{0}$ at the walls of the conducting vessel. We see that the grad ψ term vanishes.

$$\int_V \nabla \psi \cdot \mathbf{B} \, d\mathbf{V} = \int_V \nabla \cdot (\psi \mathbf{B}) \, d\mathbf{V} = \int_{\partial V} \psi \mathbf{B} \cdot \mathbf{dA} = 0$$

For a force free magnetic field configuration satisfying $\nabla \times \mathbf{B} = \lambda \mathbf{B}$ the multiplicative factor $\gamma(\mathbf{x})$ that determines \mathbf{A} can be found by taking the curl of \mathbf{A}

$$\mathbf{B} = \nabla \times \mathbf{A} = \gamma \nabla \times \mathbf{B} + (\nabla \gamma) \times \mathbf{B}$$

so

$$\lambda \mathbf{B} = \frac{1}{\gamma} \mathbf{B} - \frac{\nabla \gamma}{\gamma} \times \mathbf{B}$$

Then taking the dot product with \mathbf{B} eliminates the cross product term and we see that

$$\lambda B^2 = \frac{1}{\gamma(\mathbf{x})} B^2$$

so $\gamma(\mathbf{x}) = 1/\lambda$ which is a constant. So the vector potential is uniquely determined (up to a scalar gauge) by the magnetic field and the force free eigenvalue λ . The vector potential for a force free magnetic field is simply

$$\mathbf{A} = \frac{1}{\lambda} \mathbf{B} \tag{A.3}$$

The magnetic helicity is then directly proportional the total magnetic energy

$$H = \frac{1}{\lambda} \int_V B^2 \, dV \tag{A.4}$$

This result implies that once a plasma has reached a force-free state, the total magnetic energy can not be reduced any further because it is constrained by the conservation of H . From then on, the magnetic field and the helicity can decay only at a much slower rate due to the bulk resistivity of the plasma. [ref A.M. Dixon Astron. Astrophys. 225, 156-166 (1989)]

Appendix B

Magnetic computations for probe calibration

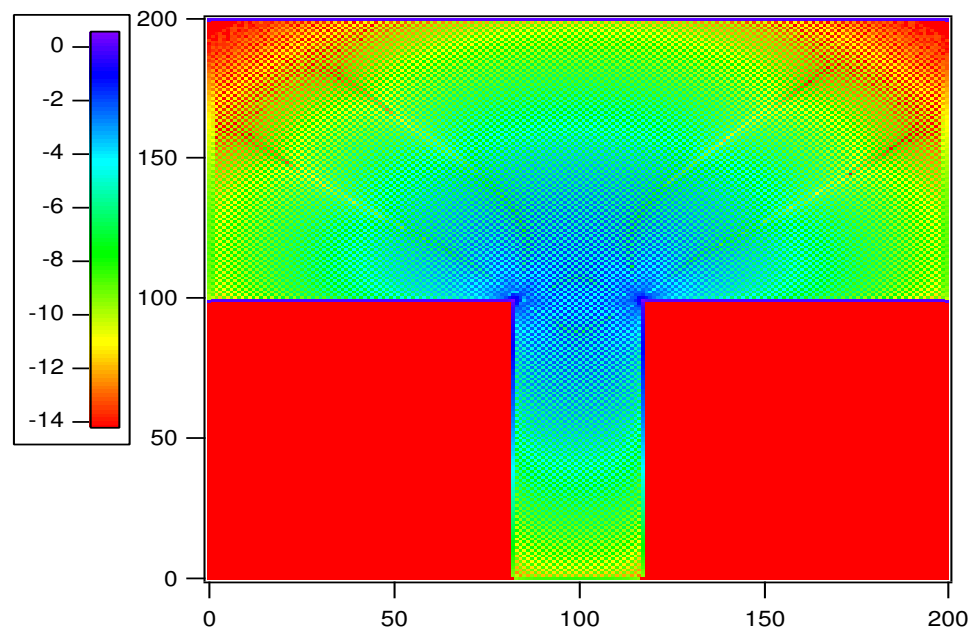


Figure B.1: The log (base 10) of the value of the Laplacian of the magnetostatic potential near a conducting port well. Since the goal is $\nabla^2 \phi = 0$, this graph indicates the order of magnitude of the error in the calculation.

Appendix C

Method of approximate reconstruction of temporal and spatial dependence of a pulse moving past a finite sequence of probes

In the following discussion we present a general purpose method of analyzing a finite sequence of time signals $F_i(t)$ that consist of local measurements of real valued observables taken at the diagnostic ports of a linear accelerator device, with i being the port index. We describe an algorithm that can reconstruct an accurate approximation of the true space and time dependence of the given observable $F(z, t)$ in the regions between the points of measurement where diagnostic access is possible. We also present the conditions needed for this approximation to hold, and we

test the algorithm by directly comparing an analytically defined wave pulse to the reconstruction of the spatial discretization of the original known pulse. We find that for many realistic physical systems as few as three probe signals provide a good reconstruction of the true spatial distribution of the known wave pulse.

C.1 Sequential measurements of a moving pulse

The motivation for developing this type of interpolation originates with daily task of trying to comprehend and interpret each sequence of time signals in real time as the data comes in. After some experience with the raw signals, a sort of mental-interchange of space and time coordinates is possible to visualize; resulting in an intuitive appreciation of the accelerator dynamics and an approximate understanding of how a given observable varies in space. Of course, it is often difficult to fully communicate this understanding to others who are less familiar with the nuances of the particular system under consideration. In this paper we present an algorithm that produces a quantitative result that makes the accelerator dynamics easy to interpret. Below in fig. 1 is presented some sample data from the Compact Toroid Injector eXperiment (CTIX), where magnetized hydrogen plasma is accelerated past a sequence of three magnetic field probes. One problem that has been central to motivating this work has been the question of what is the exact magnetic geometry of the compact toroid plasma. Essentially, we would like to know what is the function $B(z, t)$ that describes the magnetic field as a function of axial position and time. A variety of other experimental observables are also measured at sequential positions and can benefit from this interpolation analysis. The details of the CTIX facility are explained in [ref,ref,ref] [fig 1 Bz signals at 57, 91, 142] A similar problem arises in video decompression schemes when trying to interpolate in time between actual frames of a video image, in order to reconstruct a better video at a higher frame rate.[ref,ref] The motion of distinct features within an image can be taken into account to predict where each feature will be at any intermediate time t , according to a quadratic model of its trajectory. In

this problem the observables are vectors, and the details of any practical solution ultimately rely some advanced image analysis. While the problem of one dimensional flow considered in this paper is in some sense a lower-dimensional special case of the motion-compensated interpolation used in video analysis, in which the space and time coordinates have been interchanged, it is worth formulating this application in a coherent and directly useable way. The algorithm we have developed can be broken down into two distinct sub-processes. The first process uses correlation functions of adjacent probe signals to calculate a set of time-of-flight correspondence maps that approximately track individual fluid elements as they pass by the probe positions. The second process takes this set of correspondence maps and uses it to create fluid element trajectories, and finally computes a unitary superposition of the adjacent real data to determine the interpolated value of the observable at intermediate positions along each trajectory. For example, these signals could be measuring a given component of the magnetic field at several axial positions as a function of time, or the average particle density, or light emission.

C.2 Lagrangian Interpolation Algorithm

This method can be simply described by the following general formula for the interpolated value of the observable $f(z, t)$ at position z between the i th and $(i+1)$ th real probes, which involves a unitary superposition of neighboring probe signals, evaluated at retarded and advanced times:

$$f(z, t) = w_i(z, t)F_i(t + \Delta t_i(z, t)) + (1 - w_i(z, t))F_{(i+1)}(t + \Delta t_{i+1}(z, t)) \quad (\text{C.1})$$

where w_i is a weighting factor (≤ 1) dependent on the fractional distance between the position z of and the positions of the real probes. Although w_i can in general depend on z and t , the simplest good implementation is actually independent of time, $w_i(z) = (z - Z_i)/(Z_{i+1} - Z_i)$ where Z_i is the position of the i th real probe, $i \in \{1, 2, \dots, (n-1)\}$. The function $F_i(t)$ is the timesignal of the i th real probe, and $\Delta t_i(z, t), \Delta t_{i+1}(z, t)$ are some delay functions that will need to be optimized

for best agreement with the approximately measured flow dynamics inferred from the time of flight between sequential probes. For fluid that is moving in the positive z direction, a given fluid element first passes by the lower probe at Z_i , then it passes through the value of z under consideration for interpolation, and lastly it passes the upper probe at Z_{i+1} . And so with the sign convention used in (C.1) we see that $\Delta t_i(z, t)$ will have negative values, while $\Delta t_{i+1}(z, t)$ will have positive values.

C.3 Estimation of Flow Field

Ideally we need to find the time-of-flight of each distinct fluid element as it travels between adjacent probes. To define distinct fluid elements we need to work with the group velocity of the wave pulse, and the most robust approach is to calculate the correlation function between adjacent probe signals

$$C_i(\Delta t) = \int F_i(t)F_{(i+1)}(t + \Delta t)dt$$

The peak of $C_i(\Delta t)$ occurs when Δt is equal to the time of flight of the pulse between the probes. This is a much better method than simply comparing the time of peak probe signals, which can produce erroneous results that are a combination of the group velocity and the phase velocity of any higher frequency modes within the pulse. The result of this step is a vector of time shifts Δt_i such that $C_i(\Delta t_i) = \max C_i(\Delta t)$, $i \in \{1, 2, \dots, (n - 1)\}$.

Implementation The only challenge is establishing a good model of the fluid velocity $v(z_n)$ at each virtual probe position as a function of timeFinally, once $f(z, t)$ has been found it is then possible to resample the combined set of probe signals, real and virtual, to get F as a function of z , for each timeslice. This process of interpolation generates the function $F(z_n, t)$ from the measurements $F_1(t), F_2(t), \dots, F_n(t)$. It is standard to formulate this type of problem in terms of a flow function

$$\eta(\hat{x}, t)$$

C.4 Validity of Approximation

Test the algorithm by directly comparing an analytically defined wave pulse to the reconstruction of the spatial discretization of the original known pulse. Accurate for longest wavelength modes. Timescale of interpolation is much smaller than Resistive Diffusion timescale. Numeric simulation test shows what the fastest measurable mode is ... numerical reconstruction of an analytical test function

C.4.1 First order velocity error

We need to find the error in the velocity curve of the CT-pushing field interface (CT back edge), since this will have an effect on the entire reconstruction. The key idea is that will be some time error Δt in the measurement of the time that the CT back passes each probe position, and this error is dependent on the random fluctuation of the signal level, and inversely proportional to the slope of the signal at the crossing time. $\Delta t = \frac{1}{m} \Delta B_z$. First we need to estimate the signal fluctuation level. Here we will investigate the high frequency noise in the B_z signal as being the source of any errors in computing the velocity of the CT as a function of time. We will define the signal fluctuation to be the maximum absolute value of the residual of the B_z signal after subtracting off a smoothed version of the original signal.

$$\Delta B_z = \max |B_z(t) - \text{smoothed}(B_z(t))|$$

However, the result of this is dependent on exactly how much smoothing is done. To provide an objective criterion for sufficient smoothing, and thereby yield uniform results in this analysis, we will adopt the following procedure to implement the smoothing. The primary concern with this procedure is that it smoothes enough, but not too much. The fluctuations that we identify as noise in our B_z signals typically exhibit a rapid change from positive to negative slope over a short interval of time. And so the “true” signals (as we conceptualize them) that lie underneath the noise will not have this “jumpy” character to them. As a reasonable measure of this “jumpyness” factor we

can consider the first time derivative of the partially smoothed signal S_i , and then multiply it by a weighting factor determined by the duration that the signal is near that value of time-slope. The result is a function of time

$$jump(t) = \frac{1}{Duration(slope)} \cdot \frac{dS_i(t)}{dt}$$

Here, the term $Duration(slope)$ is simply the time between zero crossings of the time derivative, and it measures (in a piecewise fashion) the duration that the signal has either positive or negative slope. The reason for dividing by the duration of same-sign slope is that the physically real signal may have large slopes, but it will typically maintain this slope for some extended period of time; whereas noise will change the sign of its slope every few digitization steps. As the original signal is iteratively smoothed, the noise will be removed, and the maximum absolute value of $jump(t)$ of the i th partially smoothed signal S_i , will fall monotonically. Let us call this jumpiness parameter $\xi = \max |jump(t)|$. The smoothing process should stop when ξ falls below some small predetermined value ξ_{stop} , which should be in agreement with estimates of the signal to noise ratio for the probe signals. Approximately, $(1 - \xi_{stop}) \sim (signal/noise)$. For example, here is the Bz 57, 91, and 142 signals for shot ?. With a value for the smoothing limit of $\xi_{stop} = 0.01$ we will tabulate the estimated signal error ΔB_z , and a corresponding arrival-time error $\pm \Delta t$ for each probe. Lastly we list the relative error of the final velocity of the CT, derived from the maximum possible error considering all possible sign combinations for each of the arrival time errors. Note that if you had a set of three new arrival times that were all shifted in the same direction (either + or -) by the same amount Δt , then the calculated final velocity with these "errors" would be exactly the same as the true final velocity. Only if there is some asymmetric distribution of positive or negative errors, will the resulting error of the final velocity reach its maximum value. Here we list this worst case velocity error as an upper bound.

C.4.2 Constraints on the amplitude of undetectable transient pulses

In order to estimate the reliability of this reconstruction method we need to carefully consider the worst possible errors that could in the space between consecutive probes. We will consider errors that are as large as the mathematics of the algorithm allow, with no concern initially for the physical limitations on such errors. The end result of this analysis is a constraint in the form of an uncertainty relation between the duration and spatial extent of any undetected transient pulse-like modulations of the field occurring in the unmeasured region between the probes. This will provide a solid upper limit to the total error of the reconstruction. Since the probes themselves yield extremely accurate and reproducible measurements of the field quantities in the immediate vicinity of the probe locations, there is very little error due to global fluctuations, since these would be detected simultaneously by multiple probes. Instead, the real cause for concern are *transient fluctuations*, that cause error because they are short enough in duration and spatial extent, and happen to occur deep enough into the empty space between probes so that they go undetected, and consequently the algorithm has no ability to include their existence in the reconstructed waveform.

It is tractable and informative to consider transient pulses that have a Gaussian form in space and time (z, t) such as

$$\mathcal{F}(z, t) = A e^{-\left(\frac{t - t_p}{\tau}\right)^2} e^{-\left(\frac{z - vt}{L}\right)^2}, \quad (\text{C.2})$$

here, A is the amplitude of the pulse, τ is the characteristic rise/decay time of the pulse, ie its duration, L is the characteristic spatial extent, t_p is the time at which the pulse reaches its peak value, and v is the pulse group velocity, which we will assume is approximately the average fluid velocity. To measure the damage this pulse could do to our reconstruction, we need the envelope of the pulse as a function of position z , which is the maximum value of the pulse at a fixed z , over all values of time.

First we find, for each z , the value of t maximizes $\mathcal{F}(z, t)$. For positive-valued Gaussians like we are considering, there is a finite maximum value but no minimum value for finite (z, t) . The maximum occurs when $\partial\mathcal{F}/\partial t = 0$,

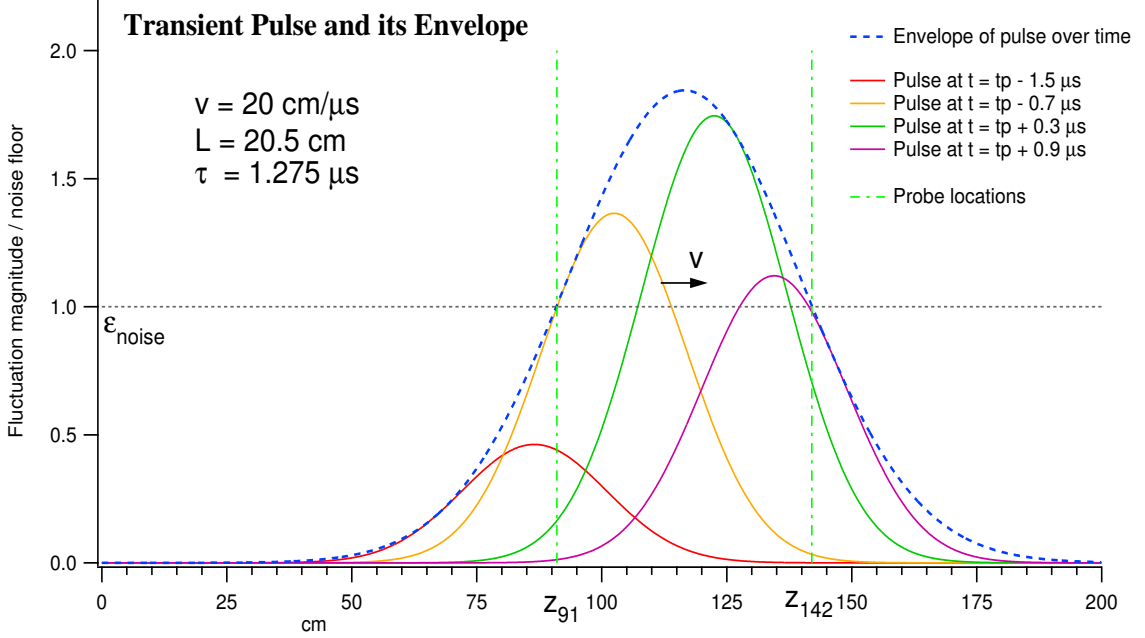


Figure C.1: Transient pulse at various times and its time-envelope as a function of axial position.

$$\frac{\partial \mathcal{F}}{\partial t} = -\mathcal{F}(z, t) \left(\frac{2}{\tau} \left(\frac{t - t_p}{\tau} \right) - \frac{2v}{L} \left(\frac{z - vt}{L} \right) \right)$$

And so the maximum occurs when

$$\frac{t - t_p}{\tau^2} - \frac{v(z - vt)}{L^2} = 0$$

$$\text{or } t \left(1 + \frac{v^2 \tau^2}{L^2} \right) = t_p + \frac{v^2 \tau^2 z}{L^2}$$

Now, to clarify the algebra, let us define a dimensionless parameter $\kappa = v\tau/L$, and we see that for a fixed z the pulse reaches a maximum value at time

$$t = t_{max}(z) = \frac{t_p + \frac{\kappa^2 z}{v}}{(1 + \kappa^2)}$$

The envelope is given by $\mathcal{F}_{env}(z) = \mathcal{F}(z, t_{max}(z))$, which simplifies to

$$\mathcal{F}_{env}(z) = A e^{-\left(\frac{z - vt_p}{L\sqrt{1+\kappa^2}}\right)^2}.$$

Restated in terms of τ , (using $L\sqrt{1+\kappa^2} = \sqrt{L^2+v^2\tau^2}$), this is

$$\mathcal{F}_{env}(z) = A e^{-\left(\frac{z-vt_p}{\sqrt{L^2+v^2\tau^2}}\right)^2}. \quad (\text{C.3})$$

In order for this pulse to be undetected by neighboring probes located at z_A and z_B we would need the pulse envelope to be less than some noise floor ϵ_{noise}

$$\mathcal{F}_{env}(z_A) < \epsilon_{noise} \quad \text{and} \quad \mathcal{F}_{env}(z_B) < \epsilon_{noise} \quad (\text{C.4})$$

where ϵ_{noise} is the determined by statistical fluctuations that are present in an ensemble of measured signals under equivalent experimental circumstances. It does not have to be restricted to just the electrical noise present in the probe diagnostics, but could include actual MHD modes in the plasma that constitute random deviations away from the average waveform of the probe signals. It is at least conceptually possible that occasionally these real fluctuations would occur at a larger than normal amplitude and in a transient fashion between the probes, and thus go undetected. In the worst case scenario the peak of the transient pulse would occur at exactly the half-way point between consecutive probes, thereby allowing the largest possible amplitude allowable by (C.4). From this (unlikely) situation, we could make the most conservative estimate for the accuracy of this reconstruction method. The true accuracy should only be better than what we find here. The worst case is when $vt_p = z_{mid} = \frac{1}{2}(z_A + z_B)$, and so let $\Delta L_{probe} = 2(z_B - z_{mid})$. Then condition for nondetection is

$$A e^{-\left(\frac{\Delta L_{probe}}{2\sqrt{L^2+v^2\tau^2}}\right)^2} < \epsilon_{noise} \quad (\text{C.5})$$

And the maximum possible undetectable amplitude is constrained by

$$A < \epsilon_{noise} e^{\frac{\Delta L_{probe}^2}{4(L^2+v^2\tau^2)}} \quad (\text{C.6})$$

This maximum possible amplitude is plotted in fig (C.4.2) as a function of fluctuation duration and spatial extent (τ, L) using parameters typical for the CTIX experiment. Using this result we can make statements regarding an upper bound of the error of the reconstruction method, such as:

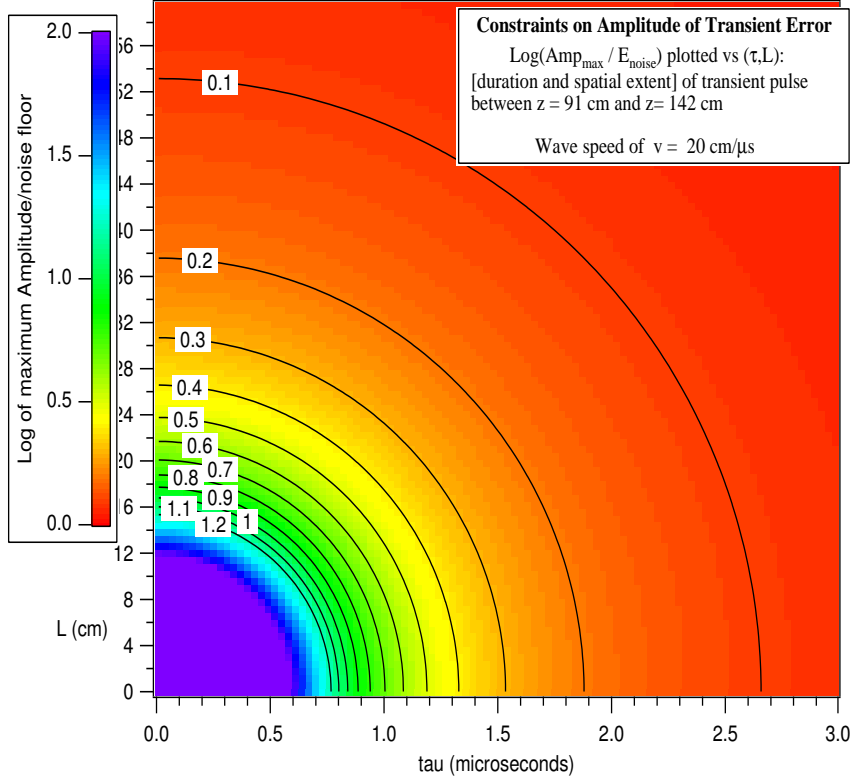


Figure C.2: Log (base 10) of the maximum possible amplitude of undetected transient pulses, plotted as a function of pulse duration and spatial extent.

For an average fluid velocity of $v = 20 \text{ cm}/\mu\text{s}$ in the region between $z_A = 91 \text{ cm}$ and $z_B = 142 \text{ cm}$, if there exists an undetected transient pulse that spans the space between the probes, and exists for at least the transit time between probes [$2L = 51 \text{ cm} \Rightarrow L = 20.5 \text{ cm}$ and $2\tau = (51/20)\mu\text{s} \Rightarrow \tau = 1.275\mu\text{s}$], (see fig C.4.2) then the amplitude of the pulse can be no larger than

$$A_{max} = 1.84493 \cdot \epsilon_{noise}$$

For pulses that are significantly shorter in duration and extent, the upper limit on amplitude becomes much larger than this example. In fact, formula (C.6) goes to ∞ in the limit of zero pulse length and duration. Ultimately however, this does not cause any serious problems if our goal is to reconstruct the average waveform of the field moving past a set of probes, where we care about a spatial resolution of several cm, and temporal resolution of a few μs . Also, there is a mitigating factor involving the probability of these hypothetical high-amplitude events. If we take the noise floor to be the expectation value of the natural fluctuations \mathcal{F} that occur with the plasma, $\epsilon_{noise} = \langle \mathcal{F} \rangle$,

then we can use Markov's inequality [ref] to bound the probability that a high-amplitude event will occur during any given shot. Let \mathcal{F} be a nonnegative random variable; then for any amplitude of fluctuation $A > 0$, the probability that \mathcal{F} will exceed A is bounded according to

$$P(\mathcal{F} > A) \leq \frac{\langle \mathcal{F} \rangle}{A}$$

For example, the probability that a fluctuation will exceed 100 times ϵ_{noise} , is at the very most 1/100. And so, although high amplitude errors are possible, they are constrained by basic probability laws to be correspondingly rare occurrences. Alternatively, if there is some physical reason for some finite upper bound on A , such as conservation of energy perhaps, then we can restate equation (C.6) in the form of an uncertainty relation

$$L^2 + v^2\tau^2 < \frac{\Delta L_{probe}^2}{4 \ln\left(\frac{A}{\epsilon_{noise}}\right)} \quad (\text{C.7})$$

We see that if $A < \epsilon_{noise}$ then L and τ are unconstrained, which agrees with the fact that small amplitude fluctuations have already been included in our definition of ϵ_{noise} . But as A becomes larger, the region of spacetime with a significant reconstruction error must become smaller and smaller, and its occurrence becomes increasingly improbable. Lastly, for some fixed $A > \epsilon_{noise}$, we see that there is a trade-off between the spatial extent and the duration of undetectable pulses, and that this relationship depends on the fluid velocity and the distance between consecutive probes. The best reconstruction occurs when consecutive probes are closely spaced, and there is a high flow velocity.

Appendix D

Equations of incompressible resistive MHD

Both \mathbf{v} and \mathbf{B} are solenoidal

$$\nabla \cdot \mathbf{v} = \nabla \cdot \mathbf{B} = 0 \quad (\text{D.1})$$

The definition of fluid vorticity closely parallels that of current density via Ampere's Law

$$\boldsymbol{\omega} = \nabla \times \mathbf{v}, \quad \mathbf{j} = \nabla \times \mathbf{B} \quad (\text{D.2})$$

The vorticity evolves in time according to a generalized Navier-Stokes equation that includes the effect of the Lorentz force term ($\mathbf{j} \times \mathbf{B}$)

$$\partial_t \boldsymbol{\omega} - \nabla \times (\mathbf{v} \times \boldsymbol{\omega} + \mathbf{j} \times \mathbf{B}) = \mu_\nu (-1)^{\nu-1} \Delta^\nu \boldsymbol{\omega} \quad (\text{D.3})$$

Where μ_ν is the fluid viscosity and the exponent ν determines the type of diffusion operator that is used. $\nu = 1$ gives usual Navier-Stokes diffusion. $\nu = 2$ gives "hyperdiffusion"

The magnetic field also evolves in time according to a convection-diffusion equation:

$$\partial_t \mathbf{B} - \nabla \times (\mathbf{v} \times \mathbf{B}) = \eta_\nu (-1)^{\nu-1} \Delta^\nu \mathbf{B} \quad (\text{D.4})$$

Where η_ν is the electrical resistivity of the fluid. Be aware that equations D.3 and D.4 are nonlinearly coupled through the convection terms.

Appendix E

Vector field visualization using a complex color code

Appendix F

Direction of future research